Laser-induced heat and momentum transfer in nanostructure processing

Matthew J. Crane

A dissertation
submitted in partial fulfillment of the
requirements for the degree of

Doctor of Philosophy

University of Washington

2017

Reading Committee:

Peter J. Pauzauskie, Chair

Vincent C. Holmberg

E. James Davis

Scott T. Dunham

Program Authorized to Offer Degree:
Chemical Engineering

University of Washington

Abstract

Laser-induced heat and momentum transfer in nanostructure processing

Matthew J. Crane

Chair of the Supervisory Committee:
Assistant Professor Peter J. Pauzauskie
Materials Science & Engineering

The ability to engineer materials with precise atomic structure represents one of the major challenges in chemistry and materials science. Steps toward this goal have led to applications in medicine, chemistry, physics, and engineering. Among the many possible synthetic parameters, light with wavelengths close to nanomaterial's size plays an increasingly important role due to its ability to resonantly target nanomaterials and to create highly non-equilibrium environments to explore new chemistry. Here, we leveraged Mie theory, chemistry, and photothermal effects to drive phase transformations in carbon and to assemble nanomaterial heterostructures.

In the first part of this work, we developed a bottom-up method to synthesize doped nanodiamond with defects defined by small molecules. To demonstrate this process, we synthesized carbon aerogels doped with small molecules and drove a phase transformation at high pressures with photothermal heating. Photoluminescence revealed that the small molecules doped into the carbon aerogel persisted as active color centers in the nanodiamond product. These results open the door for designer defects that are precisely controlled by the stereochemistry of the molecular dopant, rather than thermodynamics. In addition, microscopy studies of the doped nanodiamond also revealed the incorporation of noble gas pressure media, which were previously thought to act only as spectators, challenging the existing view of the high pressure community.

By leveraging the rapid timescale of photothermal heating, we also synthesized a new form of carbon with a rhombohedral unit cell, belonging to the Pban space group. We have tentatively named the phase Pban-carbon.

In the second part of this work, we used light in the form of an optical trap, to manipulate, align, and assemble nanomaterial building blocks into complex heterostructures. To expand the range of accessible nanomaterials, we conducted these experiments in organic solvents for the first time. The fivefold decrease in thermal conductivity in organic solvents compared to water led to a nonlinear increase in temperature. We measured these temperatures optically with ratiometric quantum dots and used them to solder germanium nanorods together with bismuth nanocrystals.

TABLE OF CONTENTS

LIST OF FIGURES

LIST OF TABLES

ACRONYMS

BET: Brunauer–Emmett–Teller

BF: bright-field

CVD: chemical vapor deposition

DAC: diamond anvil cell

DDA: discrete dipole approximation

DDSCAT: discrete dipole approximation code

DFT: density functional theory

EEL: electron energy loss

EDS: energy dispersive X-ray spectroscopy

ESA: excited state absorption

FTIR: Fourier transform infrared transmission spectroscopy

HAADF: high-angle annular dark field

HPHT: high-pressure, high-temperature

HR: high resolution

MAADF: middle-angle annular dark field

NA: numerical aperture

NIR: near-infrared

NV$^-$: negatively-charged nitrogen vacancy

NWS: nanowires

PL: photoluminescence

PTFE: polytetrafluoroethylene tape

QD: quantum dot

RFA: resorcinol–formaldehyde aerogel

SAED: select area electron diffraction

SEM: scanning electron microscopy

SIV$^-$: negatively-charged silicon divacancy

SRIM: stopping and range of ions in matter

STEM: scanning transmission electron microscopy

TPA: two-photon absorption

TEM: transmission electron microscope

TEOS: tetraethyl orthosilicate

TCSPC: time-correlated single photon counting

TMD: transition metal dichalcogenide

XRD: x-ray diffraction

ZPL: zero phonon line

ACKNOWLEDGMENTS

I can't image where I would be without my thoughtful, inspiring, and wise mentors, many of whom were much younger or much older than me.

First, I want to thank and acknowledge my adviser, Peter. The most successful research projects grow from the kernel of a compelling and open-ended idea, and Peter gave me many, many kernels. In addition, Peter pushed me to always dig deeper into data, even when I thought that I had already squeezed out the last drop of results. These suggestions led to some of the most exciting results of my PhD and have given me the belief that there is almost certainly a major finding in every experiment, if you look close enough.

Second, I want to thank my committee members, Vincent and Jim. Among my many academic mentors, Jim was perhaps the most constant throughout my graduate career. Jim guided me through graduate heat transport, changing advisers, and research to give me a wonderful, quantitative foundation that will last throughout my career. Jim's stories and insights were the stuff of legends in office hours and will remain an important and guiding part of my life. Vincent was a mentor and, I daresay, friend who constantly encouraged me with his excitement and let me pepper him with questions. Walking into Vince's office, I was often full of confusion and questions; walking out of Vince's office, I was confident and full of direction.

I hope to emulate and to achieve at least fraction of what these mentors have accomplished.

Finally, I want to thank my family and friends for their constant support. It

is an understatement to say that I have constantly been inspired by their opinions, character, and love. But all I have is words, so they will have to do. To the coffee crew, you argued with me when I was an idiot and kept me sane. To Elena, you made me compassionate, kind, a better person, and a better puppy. You're so funny. To my aunts and uncles, you engaged me endlessly and kept me curious. To grandma and grandpa kitty, you taught me what it means to be content, made me a mean card player, and sang with me. To grandma and grandpa neck, you laid the world at my feet and let me find my way through it. You taught me to ask questions, embrace creativity, and constantly inspired me with your lives. To my Mom, Dad, and sister, I don't know how you managed to put up with me, make me laugh, and allowed me to keep asking why, even after I found out what was smaller than a molecule. Someday you'll have to tell me how you did it. You taught me to get a ladle, and, when I couldn't find it, you were there for me. Thank you.

I love you all.

DEDICATION

The highest I've ever stood is on the shoulders of my family.

For my Mom, Dad, and Sister.

Chapter 1
INTRODUCTION

The control over a solution or material's temperature remains one of the most useful handles to understand and to manipulate matter: the temperature of a reaction dictates the extent of a reaction through thermodynamics, the rate at which it progresses via kinetics, and the diffusion of reactants or products as they arrive or leave. An understanding of these complex phenomena through Fourier's Law and Fick's Law has enabled the synthesis of compelling new materials and chemicals and the creation of new technologies [1]. In addition, it has facilitated the growth of materials with structures smaller than their mean scattering phonon length or their Bohr-exciton radius. The confinement of materials to dimensions below their mean scattering phonon length or their Bohr-exciton radius has produced interesting phenomena that have become the topic of extensive research across a range of fields [2, 3]. However, it is challenging to manipulate and to grow structures at the nanoscale, where strong forces dominate. For instance, how does one assemble and attach nanomaterials together, observe reactions at a single site, or place dopants in structures with atomic precision? Fortunately, we have developed new technologies to process and to analyze at smaller and smaller scales. Light-based techniques have become one of the premier methods for the large scale manufacture, study, and manipulation of nanostructures. Because the area of manipulation depends only on the light wavelength, single-mode lasers are used extensively in VLSI semiconductor processing, diagnostics and therapeutics, biological labeling, super resolution techniques, and laser refrigeration to name a few examples [3–6]. If the process is intensity- or temperature-dependent, we can surpass the diffraction-limit by leveraging light-matter interactions and analytical heat transport such that reactions occur only at the center of focused beam [7]. Despite these advances, we still struggle to accomplish

seemingly-easy "bulk" processing tasks.

In part, this is due to the challenge of understanding how heat and mass diffusion occur at the nanoscale when phonons are confined and electrostatic and curvature effects dominate. For example, phonon scattering at interfaces of materials can lead to a Kapitza resistance; curvature-dependent thermodynamics causes Ostwald ripening of nanoparticles and diameter-dependent melting temperatures; and, light-matter interactions change the rate of radiative heat loss in nanostructured materials [8–10]. How heat flows in nanoscale structures strongly impacts both existing processes such as semiconductor manufacturing and integrated circuit operation as well as emergent technologies such as forming dopants in diamond and studying kinetics of chemistries like supercritical-fluid-liquid solid (SFLS) nanowire growth [11].

1.1 Dissertation overview

My PhD research uses light-matter interactions to lay the foundation for exploring these processes and leverages the results to engineer new complex materials. In particular, my PhD work investigates laser-induced excitation, heating, and scattering in nanomaterials to drive phase transformation, to modify the kinetics of chemical processes, and to assemble nanoparticles. Broadly, radiation-based heating excels in these endeavors because it provides a contact-free method to heat samples below the diffraction limit while avoiding substrate effects. Additionally, generating heat in low conductivity environments can produce high temperatures without high temperature equipment, an advantage that was recently used to fully reduce graphene oxide to graphene and to synthesize highly monodisperse gold nanorods [12, 13]. In this report, my research on these topics is separated into two distinct sections: high pressure, high temperature (HPHT) diamond anvil cell research and optical trapping.

The breadth of my PhD work focused on developing a bottom-up method for synthesizing doped nanodiamond. Chapter 2 introduces the motivation for these experiments and places Chapters 3 to 5 in context. Briefly and in collaboration with many excellent scientists, I employed a doped carbon aerogel, a microporous amorphous carbon gel, as a precursor for

nanodiamond formation at HPHT conditions in a laser-heated diamond anvil cell (DAC). I demonstrated that dopants added into the carbon aerogel precursor persisted as active color centers in the recovered nanodiamond by targeting SiV^- and argon-based defects. This portion of my thesis concludes with the observation of a new phase of carbon, which we tentatively name Pban-carbon, formed by modifying the kinetic pathway to diamond with rapid laser heating. Diffraction measurements imply that Pban-carbon is a rhombohedral phase of carbon with a predominantly sp^3 structure. Initial theoretical studies suggest that I-carbon is a semimetal.

Next, Chapter 6 outlines experiments conducted with an optical trap, which is a high irradiance, laser-based technique that allows for simultaneous manipulation of a nanometer or micrometer scale particle in three dimensions. The optical trap is an excellent tool to interrogate and to assemble single nanomaterials into complex devices. I expanded the optical trap to non-aqueous solvents and measured the temperature of optically-trapped silicon and germanium nanowires for the first time. I used the results of this experiment to assemble bismuth nanocrystal-germanium nanowire heterostructures freely in solution.

My thesis concludes with a side project, where I leveraged the high surface area and electrical conducitivity of pyrolyzed carbon aerogel and the high capacitance of transitional metal dichalcogenides to produce a supercapacitor. Chapter 7 details the rapid synthesis and evaluation of carbon aerogel-TMD composites for supercapacitor applications.

Chapter 2
DIAMOND ANVIL CELL

The ability to access high pressure environments has provided a glimpse into new phases of materials with exotic properties, including phases of silicon with direct band gaps [14], materials with core electron bonding [15], topological insulators [16], and high-temperature superconductivity [17]. Examining these unexpected behaviors enables the rational prediction and design of new materials. In general, varying the pressure modifies the Gibb's free energy through the pV term,

$$G(p,T) = U(p,T) + pV - TS(p,T) \tag{2.1}$$

which can often approach or exceed the bond energy. Non-intuitively, this does not always yield the closest packed structure.

One particularly interesting goal of high pressure research that well-illustrates the evolution of the field is the search for a metastable superconducting hydrogen phase with a T_c around room temperature [18]. In pursuit of superconducting hydrogen, scientists have resorted to extreme means to exert high pressures, including the use of a light-gas gun to launch a projectile at a chamber of liquid H_2, measuring the solution conductivity before its destruction [19], and pulsing a sample with Sandia Lab's Z-machine, which is capable of generating large pulsed currents (20 MA) and magnetic field densities (10 MG) [20]. In comparison, the diamond anvil cell (DAC) is a much more convenient tool, which consists of two counterposed diamond anvils, aligned planar to each other, which act as the ceiling and floor of the final chamber (Fig. 2.1). Driving the anvils together generates pressure. The relative ease of generating pressure has made the DAC the tool of choice in the search for

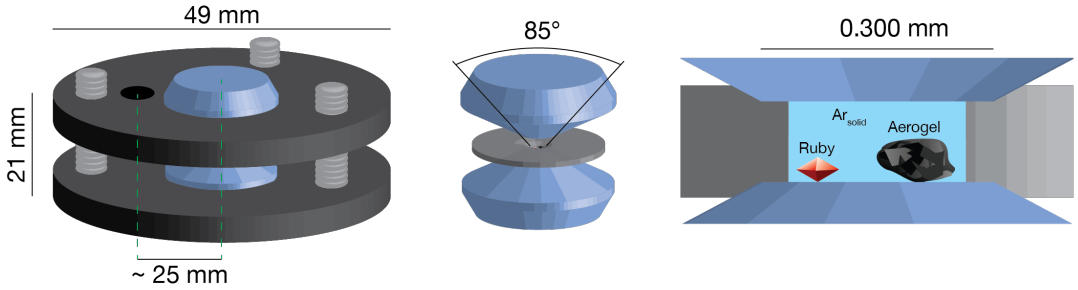

Figure 2.1: Schematic of the Boehler-Almax DAC used in our lab and these experiments.

superconducting H_2 [21] and other high pressure experiments, including ours.

In a typical DAC experiment, we dimple a metal gasket, typically rhenium, to a thickness of 30-40 μm with the anvils and drill a 80-100 μm hole in the center of the dimple with an electronic discharge machine. This hole becomes the walls of the pressure chamber. We then align the drilled gasket onto one of the anvils and load individual samples into the vessel. Finally, we add a pressure medium around the sample and drive the anvils together, until they press against the gasket to seal both the pressure media and the samples inside the cell. Because they rely on static, rather than dynamic forces to generate force, DAC's are highly portable and samples can be characterized with a range of techniques, including PL, Raman, absorption, and XRD at high or low temperatures. By patterning electrodes onto the anvils before sealing the chamber, a full range of galvanostatic measurements are accessible. Unlike other techniques, the pressure vector can be modified by using different pressure media: employing non-hydrostatic pressure medium produces a pressure field normal to the anvils, while employing a hydrostatic pressure medium produces a uniform pressure field normal to the sample's surfaces. In these experiments, we use argon, which acts as a near-hydrostatic pressure medium up to approximately 18 GPa. DAC experiments commonly use laser-heating to produce the high temperatures necessary to drive phase transitions because of the ease of optical access and the challenges of resistive heating within the confined space.

2.1 Diamond properties and applications

When considering HPHT conditions, diamond often comes to mind for good reason. By all metrics, diamond is an extraordinary material: mechanically, diamond is the hardest material and has an extremely high thermal conductivity; chemically, diamond is inert in a range of cell lines and its surface can be modified via simply wet-chemistry techniques; aesthetically, diamond shines the brightest at a jewelry shop [22–24]. These superlatives have accelerated research in diamond synthesis, among the most popular of which are CVD, plasma, and HPTP based approaches. We are specifically interested in diamond as an electronic material and as a host for unique color centers.

2.1.1 Diamond as an electronic material

Diamond exhibits a wide bandgap of 5.5 eV, high electron and hole mobilities (>3500 $cm^2V^{-1}s^{-1}$) and impressive saturation velocities (>0.8 $10^7 cms^{-1}$) at room temperature, and a predicted breakdown field strength above 10 $MVcm^{-1}$ [25] (Fig. 2.2a). These combined properties make diamond the premier material for high frequency field effect transistors, high power switches, Schottky diodes, and devices that are beyond the scope of current operating conditions due to dielectric breakdown. However, we have been unable to identify a stable n-type defect for diamond or engineer a process to create theoretically-proposed defects [27]. This is largely due to unexpected relaxation effects, which push the donor levels deep into the band gap (Fig. 2.2b) and the dense carbon lattice (3.5 gcm^{-3}), which prevents the diffusion of atoms with a molecular weight greater than carbon [28]. In particular, these limitations make it impossible to produce high-energy heteroatomic defects such as the LiN_4 and NSi_4 [29, 30] with current technologies.

2.1.2 Diamond as a host for color centers

Despite these challenges, more than 100 different color centers have been identified in diamond, spanning the periodic table from hydrogen to rare earth elements, including noble

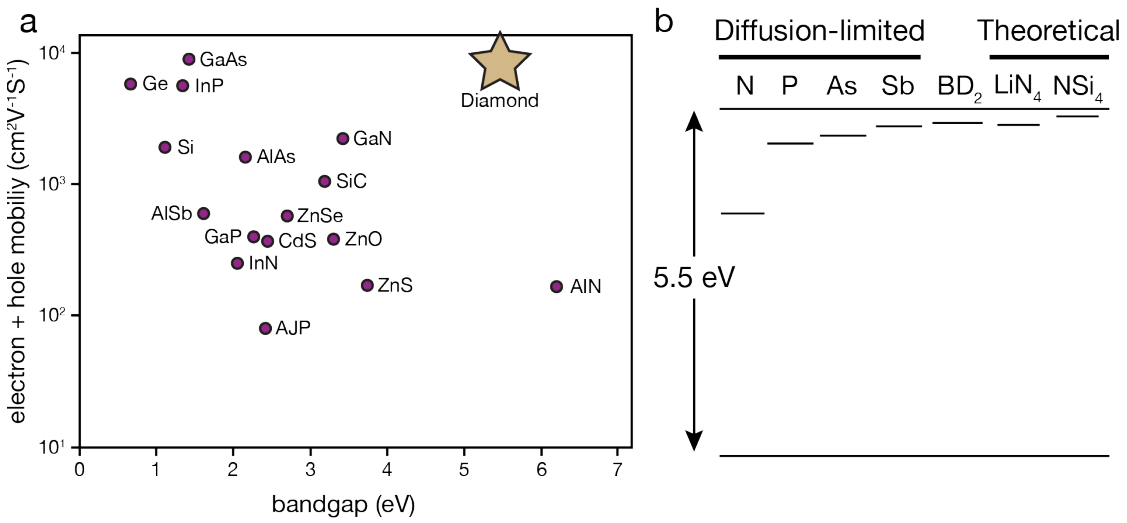

Figure 2.2: Log-log plot of combined electron and hole mobility of a range of semiconductors verses their bandgaps to illustrate breakdown voltage. Reproduced from data in [26].

gases [31]. The characterization and manipulation of these dopants in diamond has generated a wide range of applications spanning quantum computing, sensing, and cryptography [32, 33], the determination meteoritic samples'interstellar origins [34–36], and biolabeling [23]. Many properties of the diamond lattice enable these applications.

The dense diamond lattice exhibits a wide band gap, small spin-orbit coupling, and restricts heteroatom defect diffusion at temperatures far above the diamond-graphite phase line at atmospheric pressure. For example, a common defect in diamond, substitutional nitrogen, does not diffuse at temperatures below 2000 °C [28]. In quantum sensing applications, this low diffusion coefficient enables the reliable use single-defects like the nitrogen vacancy center (NV^-) to optically measure local spatiotemporal variations, which modify the defect's spin precession rate, without fear of color center migration over long time scales [32]. The NV^- center, in particular, has emerged as a promising qubit because of its long T2* lifetime at room temperature, its ability to be optically initialized, manipulated, and read out, and its lack of photobleaching [24]. Similar applications in quantum cryptography have been proposed for the negatively-charged, silicon-divacancy (SiV^-) center due to its

narrow zero phonon line (ZPL), which emits greater than 90% of its photons, compared to 5% in NV^- at room temperature.

In astronomy and geological studies, the low diffusion coefficient and extreme synthesis conditions enable nanodiamonds (Cδ), the most abundant presolar material currently identified, and bulk diamonds to act as highly stable time capsules [35, 36]. The dopants trapped in the lattice of these crystals can be studied to fingerprint the diamond's formation environment and history. For example, dopants in diamond have identified the redox state of the earth's crust and mantle [14, 37], enabled thermobarometery of diamond crystallization [38], revealed thermal and chemical properties of the forming solar systems accretion disk [36, 39].

Beyond quantum, astrophysical, and geological applications, nanodiamonds have quickly become popular in a range of applications, again, largely due to their ease of synthesis and surface functionalization and biocompatibility [23]. For example, nanodiamonds have been used in composites for their mechanical properties [40], as drug-delivery vessels for cancer therapies [41], as tissue scaffolds and surgical implants for their ability to promote bone growth [42], and have been proposed as protein mimics to make artificial nucleosomes [43]. Here, the low diamond diffusion coefficient enables nanodiamond to act as highly stable luminescent centers without photobleaching.

2.2 Diamond synthesis and doping

2.2.1 Current methods

While the dense, stable diamond lattice is ideal for applications, the high temperatures and long time scales necessary for diffusion make diffusion doping impractical at ambient condition: temperatures of 2000 °C exceed kinetic barrier of metastable diamond, which rapidly graphitizes above 800 °C.

The most common synthetic strategy to produce nanodiamonds employs dynamic (< 10 ns) high-pressure, high-temperature (HPHT) conditions to nucleate nanodiamond grains.

For example, detonation nanodiamonds form within a shockwave produced by the confined detonation of a high explosive [23]. As the shockwave propagates, the supersaturated carbon vapor rapidly condenses into nanoscale liquid droplets that homogeneously nucleate nanocrystalline diamonds. Ultrasound cavitation, laser ablation, and shock waves all generate similar conditions and lead to nanodiamond formation [44–46]. The doping of nanodiamonds synthesized with these dynamic processes occurs by varying the chemical composition and bonding of the carbon precursor, which provides a potential route to influence the formation of optically-active, heteroatomic point-defects [47, 48]. However, the brief duration of the HPHT conditions generated in these methods produce a wide range of lattice defects and result in the unintentional incorporation of heteroatoms from the synthesis chamber. This lack of synthetic control ultimately limits the optoelectronic application of detonation nanodiamond materials [49].

Bulk diamond films grown via chemical vapor deposition (CVD) exhibit significantly greater chemical purity and electronic quality in comparison with detonation nanodiamond. In this process, a high energy plasma breaks down a mixture of carbon and hydrogen molecules into individual, gaseous sp^3 carbon atoms. The selective addition of sp^3-bonded carbon atoms onto a substrate seeded with diamond with concomitant etching of graphite by hydrogen yields diamond growth driven by kinetics at low pressures. Directly adding dopants to the precursor feed deleteriously influences the kinetics to modify the growth direction and or the product. More significantly, the plasma completely dissociates species in the precursor feed causing dopants to incorporate non-deterministically at random locations and without their initial stereochemistry, limiting the ability of this approach to produce heteroatomic defects.

Because modifying the growth feedstock curtails diamond synthesis and lacks control of heteroatomic defect formation, post-growth ion implantation of CVD diamond films is often used to add heteroatomic dopants. Ion sources can achieve a high degree of spatial dopant control through the use of masks and stopping and range of ions in matter (SRIM) calculations [50]. This process relies on Poisson statistics, SRIM calculations, and masking

techniques to control color center generation [33]. Subsequent thermal annealing and acid-washing can mitigate lattice damage, remove sp^2 carbon, and drive carbon-vacancy (V_c) diffusion to generate optically-active defects [50, 51]. In addition, recent advances with pulsed lasers have enabled a high precision of V_c incorporation to potentially replace this annealing step [52]. Subsequent ball milling or etching of CVD-synthesized diamond films can produce nanodiamonds via a top-down approach with similarly high quality as the original films, as evidenced by the long T2* lifetimes in the resulting nanodiamonds [53]. However, it has remained a challenge to use CVD methods to create complex, polyatomic defect centers in diamond, due to the decomposition of ion sources as they penetrate the diamond lattice.

The static, HPHT synthesis of diamond also can yield bulk crystals with electronic properties similar to ion-implanted CVD diamond. In fact, during the first attempts at industrial-scale bulk, HPHT diamond synthesis, nanodiamonds were an unexpected byproduct. The direct HPHT synthesis of nanodiamonds was not pursued again until recently [54–58]. Research on bulk HPHT diamond during this 50-year hiatus realized a range of important discoveries including the use of catalysts to decrease the pressures and temperatures required for diamond production, the observation that different carbon precursors can form diamond at less extreme conditions, and the ability to incorporate dopants into diamond by simply mixing them into the carbon precursor [56, 58–62].

Recently, nanodiamonds were synthesized at HPHT in a laser-heated diamond anvil cell from a carbon aerogel precursor, a nanostructured sol-gel of amorphous carbon aerogel that is produced with solution-phase chemistry [56]. In this approach, the absorption of a near-infrared laser increased the temperature of the amorphous carbon aerogel precursor at elevated pressures to drive a phase transition from amorphous carbon to diamond nanocrystals. The authors hypothesized that the use of a carbon aerogel precursor confined diamond nucleation and growth to yield a nanocrystalline product. In addition, the nanodiamond product contained optically-active NV^- and SiV^- defects, which were thought to stem from atmospheric and glassware impurities. Intriguingly, this observation suggests that sol-gel chemistry can be used to control dopants in diamond. Sol-gel chemistry provides many de-

grees of freedom for precise heteroatomic doping beyond what is possible in ion implantation of CVD diamond. However, a number of challenges remain in understanding the laser-driven HPHT formation of diamond including the kinetics of photothermal heating, the interplay between temperature and atomic diffusion during growth, the potential for Ostwald ripening during extreme photothermal heating, and the concentration of lattice defects [55, 59, 63].

2.2.2 High pressure, high temperature nanodiamond doping

In my PhD work, I sought to develop a bottom-up technique to synthesize doped nanodiamond without ion implantation. In this process, we proposed to overcome diamond's low diffusion coefficient by first synthesizing a doped amorphous carbon precursor and then converting it to diamond at HPHT conditions. This would allow us to deterministically integrate the desired dopant into carbon while it is thermodynamically stable with traditional synthetic techniques, rather than rely on ion implantation into a metastable substrate. If diamond grows without significant dopant diffusion in the precursor, this bottom-up approach could enable the formation of designer defects with structure dictated by the stereochemistry of the small molecule dopant, rather than relying on ion implantation and Poisson statistics. Similarly, if diamond grows without significant Ostwald ripening, bottom-up doping would enable the control of defect location both within the nanodiamond grain and relative to other dopants.

To develop this bottom-up nanodiamond doping approach, we sought to understand the origin of silicon defects from previous HPHT experiments on carbon aerogel precursors and the photothermal effects associated with diamond growth in an HPHT environment. These experiments are the topic of Chapter 3. We leveraged the results of these experiments to demonstrate deterministic silicon doping by controllably incorporating silicon-containing small molecules into carbon aerogel precursors. To demonstrate the efficacy of bottom-up dopants, we demonstrated optical pressure metrology with the silicon color centers. In addition, we investigated the role of the traditionally-inactive noble gas pressure medium on doped nanodiamond formation to illustrate that the pressure medium itself can form

defects within the diamond lattice. This represented the first time that noble gas pressure media have been recovered at ambient conditions and questions the widely-held assumption of pressure media inactivity. These experiments are the topic of Chapter 4. Finally, we show that rapid, stepped heating of the carbon aerogel opens alternate kinetic pathways. Using spherical aberration corrected electron microscopy, we identify a new phase of carbon. These results are the topic of Chapter 5.

Chapter 3

PHOTOTHERMAL EFFECTS DURING HPHT NANODIAMOND SYNTHESIS

3.1 Introduction to HPHT diamond formation

As outlined in Chapter 2, the two primary mechanisms of diamond formation involve either thermodynamic nanoscale effects or highly non-equilibrium processing, both of which inhibit polyatomic dopant incorporation and patterning[1]. In this first class of synthesis, detonation, laser ablation, or ultrasound cavitation, among others, generate high local temperatures and pressures to produce nanodiamonds, driven by the thermodynamic stability of diamond over graphite at high curvatures [23]. In the second class of synthesis, plasma-enhanced chemical vapor deposition (PECVD) dissociates a carbon and hydrogen precursor mix, creating a range of hydrocarbon species. Selective deposition of sp^3 carbon species and hydrogen termination results in diamond growth driven by kinetics [64]. For both cases, defects incorporate randomly, generating an uncontrolled range of dopants [33]. In addition, unintentional doping from reactants or reaction vessels is common. For instance, substitutional nitrogen (N_s), negatively-charged nitrogen vacancy (NV^-) and silicon divacancy (SiV^-) defects can form in PECVD, detonation, and HPHT diamonds from atmospheric N_2, reactants, and silicon reaction vessels [65, 66]. Inductively-coupled plasma analysis has identified the presence of more than 27 different elements at up to 1000 ppm average concentration in detonation nanodiamond [49].

The synthesis of nanodiamond from a carbon aerogel precursor at HPHT conditions offers an alternate method to produce doped diamond. However, nanodiamond synthesized

[1]This chapter is currently under review with the title, ". It is comprised of work from Matthew J. Crane, Bennett E. Smith, Peter B. Meisenheimer, Xuezhe Zhou, Rhonda M. Stroud, E. James Davis, and Peter J. Pauzauskie.

via this method contained both NV^- and SiV^- defects, and the source of both impurities was unknown [56]. In addition, the influence of the photothermal heating effects on the nanodiamond product, including phase conversion conditions and the temperature-dependence of color center formation, were not reported.

In this chapter, we present a predictive photothermal model of HPHT nanodiamond synthesis from an amorphous carbon aerogel precursor in a laser-heated DAC. Using Mie theory, we develop an analytical model of heat transport to quantify the maximum temperatures during nanodiamond formation. By correlating temperatures during phase conversion with Raman and photoluminescence, we identified that the nanodiamond-carbon aerogel phase boundary sits between 12 and 16 GPa and 1600 to 1800 K. This is significantly below the uncatalyzed graphite-diamond phase boundary [67]. Analytical modeling and irradiance-dependent blackbody (Planck) emission showed that the solid argon pressure medium melts to form a thermally-insulating, supercritical fluid during the synthesis. In addition, the photoluminescence of nanodiamond synthesized at the lowest laser irradiance did not exhibit NV^- centers, while PL at the highest temperatures contains NV^- defects. A temperature- and pressure-dependent CVΩ model for vacancy diffusion suggests that NV formation depends on V_c diffusion to substitutional nitrogen atoms, which is modified at HPHT conditions.

3.2 HPHT nanodiamond formation

3.2.1 Aerogel synthesis, doping, and characterization

We synthesized the carbon aerogel by dissolving resorcinol (Sigma-Aldrich) in acetonitrile (EDM Millipore) and adding formaldehyde (37 wt. % in H2O with methanol stabilizer, Sigma-Aldrich), followed immediately by hydrochloric acid catalyst (37 wt. % Macron Fine Chemicals) to avoid basic conditions that can etch SiO_2 glassware [68]. The final molar ratios of acetonitrile, formaldehyde, and HCl relative to resorcinol were 100:1, 2:1, and 1:10, respectively [69, 70]. This solution was quickly placed into a Branson 1510R-DTH ultrasonic

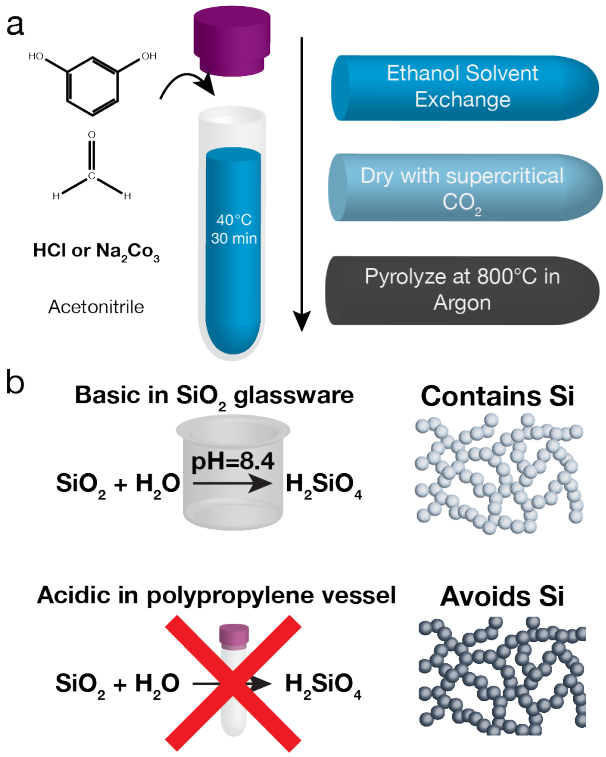

Figure 3.1: A schematic of the aerogel synthesis with either basic or acidic catalysts (a) and a visual abstract of the silicon doping hypothesis (b).

cleaner for 30 minutes, and then removed and allowed to gel for about 24 hours, during which the gel turned light pink. The acetonitrile solvent was exchanged by washing with ethanol 4 times over 5 days. To make the Erbium-doped aerogel, an aerogel sample was submerged in 0.1M $ErCl_3$ in ethanol and placed in a freezer for 28 days to allow for diffusion of $ErCl_3$ into the pores after solvent exchange. Aerogels were then dried in an autoclave filled (E3100, Quorum Technologies) with supercritical CO_2 to prevent collapse of the pore structure (Figure 3.1a). Finally, the gels were pyrolyzed under N2 at 900 °C for 4 hours to remove oxygen species. The gel surface area was measured with a NOVA 2200e.

3.2.2 Diamond anvil cell loading, heating, and spectroscopy

A Bohler-Almax plate DAC with 0.300 mm diameter culets was prepared by dimpling and drilling a rhenium gasket to a hole diameter of 120 μm. The gasket, which acts as the walls of the pressure chamber, was then carefully aligned into the DAC, which acts as the roof and floor of the pressure chamber. Gels were lightly ground in aluminum foil and transferred into the gasket with a Marzhauser Wetzlar nanomanipulator. Finely ground rubies were also added to measure pressure through optical emission of the Cr^{3+} crystal field levels. Gaseous argon was condensed with liquid N_2 and added to the DAC as a near-hydrostatic pressure medium. The liquid argon infiltrates the aerogel's pores during this process, allowing the gel to maintain its morphology throughout the phase transformation to diamond [56]. DAC pressure was incrementally increased to a final pressure of 16.3 GPa as shown in S5. We detected pressure in situ by exciting a ruby crystal placed in the cell and measuring the $^2T_1$ to $^4A_2$ Cr^{3+} emission, which has a well-documented pressure dependence. During compression to 16.3 GPa [71], the argon pressure medium undergoes a phase transition to solid, face-centered cubic argon [72].

Laser heating in the DAC was accomplished with a solid-state Nd:YAG (BL-106C, Spectra Physics) focused via a Mitutoyo 50x objective (0.55 NA) using a polarized beam splitter cube. Raman and PL were collected with a home-built setup comprised of a Coherent compass 532 nm laser, the aforementioned Mitutoyo objective, and focused onto an Acton SpectraPro 500i spectrometer with a Princeton Instruments liquid N_2-cooled CCD detector. Planck emission was collected with an Ocean Optics USB2000 spectrometer. These spectra were fit to Wien's approximation, and the result of this linear fit was used as the starting parameter for a nonlinear fit to Planck's law. All spectra were collected and intensity-corrected with an Ocean Optics HL-2000 intensity calibration lamp and wavelength-corrected with an argon lamp.

3.3 Laser-directed spatial control of HPHT nanocrystalline diamond formation

To dope diamond, we synthesized an amorphous carbon aerogel [73] precursor with a controlled molecular composition, which we subsequently pressurized and laser-heated in a DAC. The carbon aerogel used here exhibits an interconnected, three-dimensional network of amorphous carbon spheres (12.9 ± 3.4 nm diameter, Figure 3.5a) with a high surface area (311.6 m^2g^{-1}), low thermal conductivity, and broadband spectral absorption [74, 75]. Previously reported HPHT diamond aerogels contained both NV^- and SiV^- defects [56]. It has been suggested that NV^- and SiV^- defects were incorporated from adsorbed atmospheric N_2 and silicon atoms etched from glassware during the aqueous, base-catalyzed (pH=8.4) cross-linking process. Here, we used an acid-catalyzed sol-gel cross-linking reaction [69, 70] within a polypropylene vessel to investigate the origin of silicon doping. To further study the role of diffusion in doping, we deposited erbium onto the surface of the carbon sols via $ErCl_3$ in acetonitrile. We then loaded the aerogel into the DAC using argon as a near-hydrostatic pressure medium. Because it infiltrates the gel's pores before further compression to solid argon, argon allows the nanostructured carbon to maintain its morphology during phase conversion [76]. With this methodology we can directly probe dopant incorporation without relying on dynamic or non-equilibrium processing typically involved in nanodiamond synthesis. During heating, the aerogel's temperature rose with increasing laser irradiance until it reached the melting point of argon, 1383 K at 16.3 GPa [72]. After argon melted, the temperature quickly spiked to a maximum (1-2 s peak duration), due to the decrease in supercritical argon's thermal conductivity (Figure 3.3). The diamond phase conversion temperature is constant at a range of irradiances due to self-limiting absorption of amorphous carbon following the formation of nanodiamond.

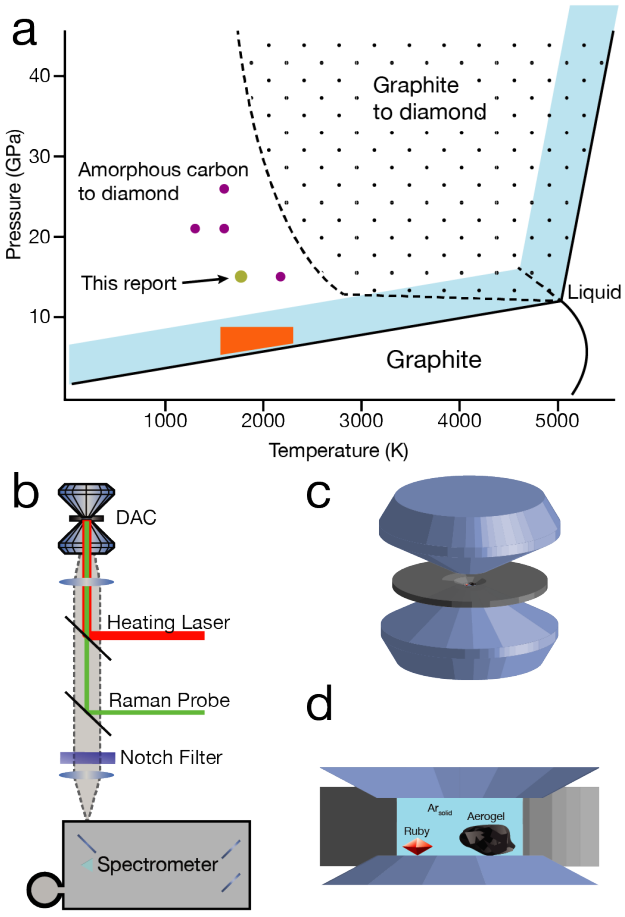

Figure 3.2: Diamond-graphite phase diagram with kinetically-accessible regions (a). The dotted region labeled shows the direct graphite-to-diamond phase transition. The light cyan region represents the phase diagram for a 1.2 nm diameter diamond nanocrystal, and the orange area represents the experimental region for catalyzed graphite-to-diamond phase conversion. The dark purple dots represent the successful synthesis of diamond from amorphous, non-graphite carbon starting materials. A schematic of spectroscopy system for laser-heating and Raman experiments (b) and the laser-heated DAC (c), with an expanded view of ruby and aerogel under hydrostatic compression by solid argon (d).

3.4 Photothermal nanodiamond formation

Upon heating above 1800 K, transparent regions appeared in the carbon aerogel with new Raman scattering modes—480, 1130, 1370, 1410 and 1550 cm^{-1}—corresponding to the formation of diamond coated with amorphous surface material, graphite, and transpolyacetylene, which are common in HPHT diamond synthesis (Figure 3.4) [56, 58, 59, 77, 78]. We distinguished potential PL from Raman scattering by observing peak shifts for Raman modes with varying excitation laser wavelength. SAED, TEM images, and EELS spectra of the carbon aerogel after HPHT processing showed crystalline structures composed of sp^3 carbon with a small amount of sp^2 carbon and a 2.06 Ålattice spacing, corresponding to nanodiamond with sp^2 surface reconstruction (Figure reffig:CAPT4). The EELS spectra also contain a dip at 302.5 eV, characteristic of cubic diamond's second gap. The minimum conditions (16.3 GPa and ~1800 K) to drive the phase change of carbon aerogel to nanodiamond are among the lowest reported, as illustrated in Figure 3.2 [58, 59, 61, 79]. In a separate experiment at 12.0 GPa and identical irradiances, there was no evidence of phase conversion, suggesting that the carbon aerogel–nanodiamond phase line sits between 12.0 and 16.3 GPa and 1340 and 1800 K. These relatively mild conditions are likely due to the amorphous carbon starting material and the rapid heating conditions. Amorphous carbon lacks long-range crystalline structure, which lowers the kinetic barrier present between other carbon allotropes like graphite (~0.4 eV) and diamond, even at high pressure [80, 81]. The rapid heating of the carbon aerogel upon melting of the argon pressure medium may prevent graphitization that occurs in resistively-heated HPHT experiments prior to the formation of cubic diamond, thereby lowering the pressures and temperatures required for phase conversion [59, 79].

This rapid heating may also enable the observation of new allotropes of carbon and will be the focus of future studies. However, this also suggests that the thermal gradients during photothermal heating due to the variation of the irradiance within the Gaussian laser (or the diffusion of heat away from the beam spot) may influence phase conversion to diamond. Indeed, while most recovered material predominantly contained nanodiamond, some

grains exhibited greater concentrations of graphite accompanied by a small amount of carbon onions. Carbon onions were not observed in recovered material with large concentrations of nanodiamond (Figure 3.5b). These data suggest that thermal gradients exist during the synthesis and that sp^2 domains likely form in lower temperature regions. Because the synthesis conditions are insufficient to drive phase conversion from graphite to nanodiamond, graphite represents a kinetic dead end and cannot produce diamond during subsequent direct photothermal heating.

Interestingly, the large thermal gradients due to the high thermal conductivity of solid argon and low thermal conductivity of carbon aerogel resulted in localized heating that limited phase conversion to a small area (Figure 3.4). By varying the irradiance, the carbon-aerogel could be heated to a temperature greater than 1800 K. Heating at 47 $MWcm^2$ and rastering over the aerogel produced a diamond line-width of 8.5 $\pm$ 0.3 μm. Heating and rastering at 22 $MWcm^2$ produced a diamond line width of 4.0 $\pm$ 0.6 μm. To the best of the author's knowledge, this is the highest resolution of diamond film patterning to date [82].

3.5 Modeling pressure-dependent defect formation

The PL spectra of nanodiamonds synthesized at average temperatures above 1480 K showed a ZPL at 610, phonon sidebands centered at 650 nm, and a lifetime of 8.2 ns, characteristic of an NV^- center under hydrostatic pressure at 16.3 GPa (Figure 3.4). This is consistent with prior reports at pressure [83, 84]. Surprisingly, NV^- production was not observed in nanodiamond formed with an average temperature up to 1340 K. Because the diamond formation temperatures are self-limiting and constant (1950 K average) irrespective of irradiance, the temperature-dependence of NV^- formation is likely not due to size or surface effects. Electron paramagnetic resonance, optical absorption, and PL spectroscopy studies have shown that nitrogen initially incorporates in diamond as a substitutional (N_s) defect, which is immobile at pressures above 6 GPa for temperatures ¡2000 K [28]. Comparably, neutral carbon vacancy defects in diamond are highly mobile, and they diffuse upon annealing until they meet N_s, where they ultimately form low-energy NV^- defects. Annealing-induced vacancy-

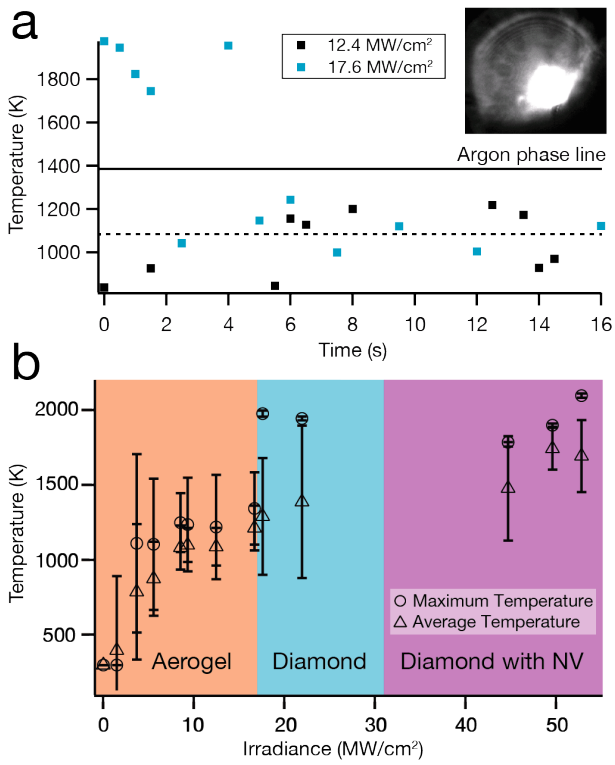

Figure 3.3: Time-dependent, Planck-fit temperatures during laser irradiation of carbon aerogel at a pressure of 16.3 GPa at 17.6 MWcm^{-2}, which melts argon, and 12.4 MWcm^{-2}, which does not melt argon (a). The dotted line represents the average temperature at 12.4 MWcm^{-2} and the solid line represents the argon solid-liquid phase line. The inset shows an image captured during laser heating. The time-averaged and maximum temperatures measured during the laser heating of carbon aerogel inside the DAC at different irradiances (b). The orange, blue, and purple panels represent the phase space where the aerogel did not undergo a phase change, where cubic diamond formed without NV, and where cubic diamond formed with NV defects, respectively. The average temperature error bars represent the standard deviation from at least 60 spectra collected over a 30 s period; the maximum temperature error bars represent 95% confidence interval fits to Planck's Law.

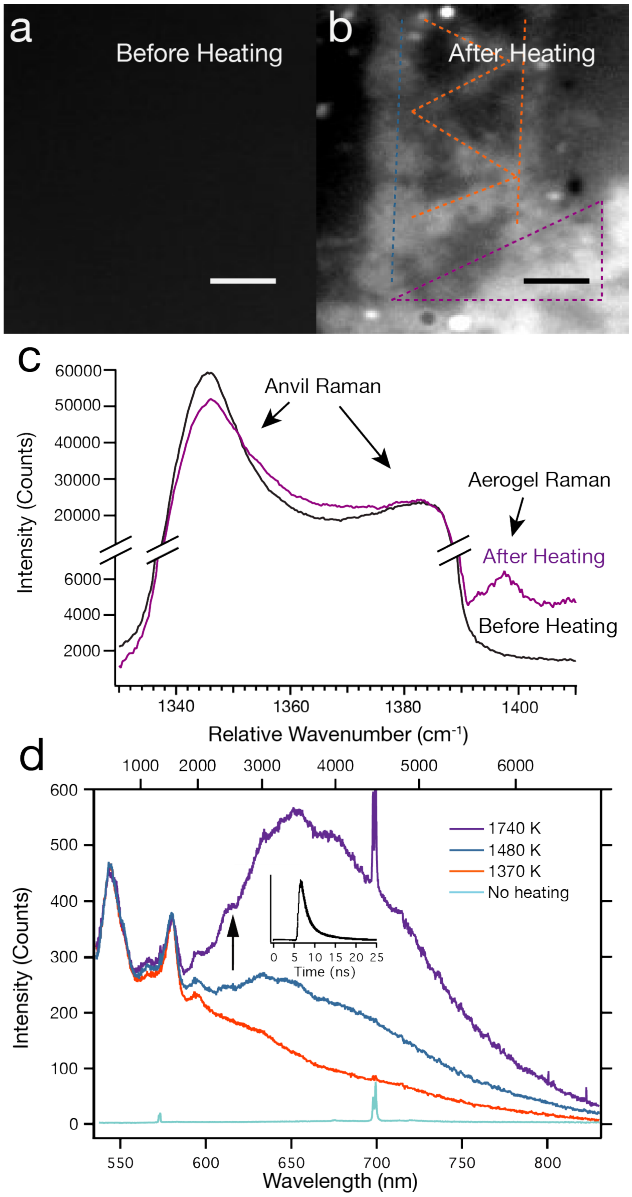

Figure 3.4: Dark field images before (a) and after (b) aerogel heating in the DAC at 16.3 GPa, respectively. Heating on the left side of (b) at 47 MWcm^{-2} yields a diamond line-width of 8.5 $\pm$ 0.3 μ m (orange dotted line); heating on the right side of (b) at 22 MWcm^2 (blue dotted line). The bottom right corner shows a large area of heating at 53 MWcm^2 (purple dotted line). Scale bars in both images are 10 μ m. Raman from the heated areas (c) and characteristic emission (d) from diamond after subsequent heating and excitation at 1 mW and 532 nm normalized to the graphite g-band. The black arrow shows the NV$^-$ ZPL at 16.3 GPa and the decay inset shows time-correlated single photon counting at this wavelength. These data are fit with two time constants at 1.2 and 7.0 ns. The sharp peaks centered at 700 nm is due to the ^{2}T$_1$to^{4}A$_2$ crystal-field transition of Cr^{3+} in the ruby pressure sensors.

diffusion is commonly used to generate NV^- defects, and the temperature dependence of this process at atmospheric pressure is well documented [33, 85]. However, the neutral vacancy diffusion coefficient decreases significantly with increasing pressure due to compression of the diamond lattice. In addition, while the carbon aerogel in this work was laser-heated in 30 second intervals, diamond films are typically annealed for ~2 hours to produce NV^- centers. Using theory to model vacancy diffusion at 16.3 GPa and a probability distribution function solution for 3D diffusion, we estimate that vacancies will consistently activate NV^- defects at ~1350 K (Table 3.1) [28, 86, 87]. Details of this calculation are shown in Appendix A. This boundary is consistent with the observed temperature range for NV^- formation, considering potential variations in N_s concentration. These observations suggest that the formation of NV^- centers in laser heated diamond occurs via the diffusion of carbon vacancies to nitrogen, which is initially incorporated as N_s below 1 wt-%, and that we can accurately predict these conditions [88, 89]. Interestingly, this also implies that varying the pressure could provide the ability to control defect formation. Finally, while there have been recent reports on strain-alignment of defects, we do not anticipate any preferential alignment due to the near-hydrostatic nature of the argon pressure medium [90].

Table 3.1: Obseved and calculated regions of NV formation from cBΩ theory

	At 1 atm $(K)^2$	Observed (K)	At 16.3 GPa (K)
Vacancies become mobile	870	-	1070
NV centers begin to form	1070	1480	1350
High quality NV centers form	1470	1700	1950

In all previous HPHT diamond aerogel syntheses, SiV^- defects with a ZPL at 738 nm consistently formed; however, in these experiments, we did not observe any SiV^- emission at any conditions. These previous HPHT diamond aerogel reports used a carbon aerogel

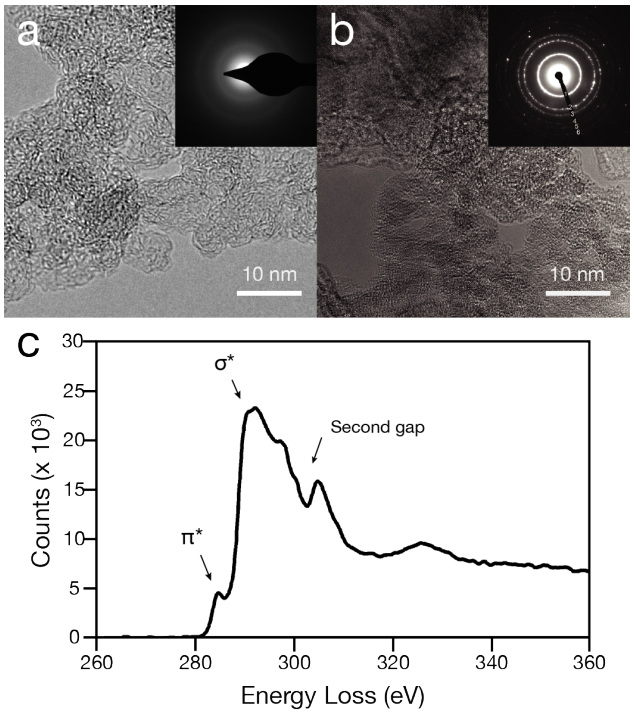

Figure 3.5: Bright field TEM images of carbon aerogel before (a) and after (b) HPHT treatment and the electron energy loss spectrum (c) of the HPHT treated carbon aerogel. The selected area electron diffraction (inset) before HPHT treatment shows amorphous material, while the pattern after HPHT treatment indexes to cubic diamond. The labels 1-6 correspond to the measured values and (hkl) indices of (1) 2.06 Å(111); (2) 1.29 Å(220); (3) 1.09 Å(311); (4) 0.92 Å; (5) 0.83 Å(331); and (6) 0.75 Å(422).

precursor that was synthesized under *mild basic conditions* using silica glassware; whereas, in the experiments reported here, we carefully avoided silica glassware and employed an alternative acidic catalyst. These observations suggest that silicon incorporates into the carbon grains as silicic acid during polymerization by basic etching of the silica glassware [68],

$$\mathrm{SiO_2(s) + H_2O\,(l)} \xrightarrow{\mathrm{pH=8.4,40\,^{\circ}C}} \mathrm{H_2SO_4(aq)} \tag{3.1}$$

which yields SiV^- centers upon conversion to diamond. To further investigate if diffusion-doping of nanocrystals is possible at HPHT, we deposited $ErCl_3$ on the precursor carbon aerogel surface. Erbium forms a bright, high quantum efficiency dopant in a range of materials [6, 91]. However, erbium emission was not observed in the nanodiamond product, despite excitation and attempted-observation with ultraviolet, visible, and near-infrared spectroscopy. These observations demonstrate that it is possible to eliminate SiV^- formation by avoiding silica-based reaction vessels and suggest that diffusion limits incorporation of large atomic radii dopants, even for nanoscale carbon.

3.6 Nanodiamond growth model

To understand the nanodiamond formation mechanism and quantify the resolution of defect control, we developed an analytical solution for the temperature within a carbon sphere upon irradiation. It is important to note that the resolution of the phase transformation depends not on the spot size of the laser [7], but rather on the ability of the carbon precursor to support large internal temperature gradients. Thus, the temperature distribution, which is a function of the pressure medium, carbon precursor, and heating laser dictate the ultimate resolution of diamond synthesis and dopant formation. To solve for the temperature distribution, we apply Mie theory to obtain the internal electric field [92] and use this solution as the source term in the energy balance, given by

$$\rho C_p \frac{dT}{dt} = \frac{1}{r^2}\left(kr^2\frac{dT}{dr}\right) + \frac{1}{r^2\sin\theta}\frac{d}{d\theta}\left(k\sin\theta\frac{dT}{d\theta}\right) + \frac{1}{r^2\sin^2\theta}\frac{d}{d\phi}\left(k\frac{dT}{d\phi}\right) + S\left(r,\theta,\phi\right), \tag{3.2}$$

where T is the temperature, r, θ, and ϕ are the radial coordinate, polar angle, and azimuthal angle defined in Figure 3.6, and k, ρ, and C_p are the thermal conductivity, density, and heat capacity of the carbon sphere. For highly absorbing spheres in the Rayleigh limit [92], the source function, S, is only a function of r. Consequently, at steady state the internal temperature is only a function of r, and the one-dimensional energy equation becomes (for constant thermal conductivity evaluated at the mean temperature of the sample)

$$\frac{d}{dr}\left(r^2\frac{dT}{dr}\right) = -\frac{S}{k}r^2 \tag{3.3}$$

The temperature is bounded at $r = 0$, and the boundary condition at the surface is a combination of conductive and radiative heat losses given by

$$-k\frac{dT}{dr}\Big|_r = R = \frac{k_{Ar}}{R}\left(T_R - T_\infty\right) + \sigma\left(T_R^4 - T_\infty^4\right), \tag{3.4}$$

where T_∞ is the bulk mean temperature of the surroundings, σ is the Stefan-Boltzmann constant, and k_{Ar} is the argon thermal conductivity evaluated at the surface temperature, T_r. The radiation may be modified by writing

$$T_R^4 - T_\infty^4 = \left(T_R + T_\infty\right)\left(T_R^2 + T_\infty^2\right)\left(T_R - T_\infty\right). \tag{3.5}$$

The solution of the energy equation becomes

$$T = T_\infty + \frac{SR^2}{3k}\left(\frac{1}{Bi} + \frac{1}{2}\left(1 - \left(\frac{r}{R}\right)^2\right)\right), \tag{3.6}$$

where the Biot number is defined by

$$Bi = \frac{k_{Ar}}{k} + \frac{\sigma R}{k}\left(T_R + T_\infty\right)\left(T_R^2 + T_\infty^2\right). \tag{3.7}$$

The surface temperature is then given by

$$T_R = T_\infty + \frac{SR^2}{3kBi}, \tag{3.8}$$

which is determined by solving equations 3.7 and 3.8 simultaneously. Based on the analysis of TEM images (Figure 3.5a), we modeled the carbon aerogel as spheres with 12.9 nm diameters. The results of this model provide several important insights. First, the temperatures achieved within carbon grains depend strongly on the thermal conductivity of the argon pressure medium, which melts to form supercritical argon during photothermal heating. The thermal conductivity of supercritical argon at these conditions is challenging to predict. We bound the temperatures by using extrapolated, temperature-dependent gaseous (1 atm) and solid (16.3 GPa) thermal conductivities to calculate maximum and minimum temperatures, respectively. This analysis suggests the maximum internal temperature to be between 1750 and 2200 K during photothermal heating at 18 MWcm^{-2} (Figure 3.6). However, based on the experimental conditions, we expect the supercritical argon to exhibit gaseous characteristics [93, 94] and anticipate that temperatures will be closer to 2200 K, which is consistent with observed temperatures. Using this assumption, the photothermal heating of isolated carbon spheres with diameters above 10 nm can drive a phase transition to diamond in supercritical argon. Below 10 nm, both collective absorption and lateral heat insulation are required to produce diamond. Synthetic control over the monodispersity of carbon spheres above 10 nm would enable the most precise resolution of nanodiamond formation by selectively converting material at the center of the focused, laser beam [7]. However, leveraging pressure and the pressure medium to adjust thermal conductivity will tune this size range.

Second, there exists a large temperature gradient throughout the individual carbon grains during photothermal heating, and the maximum occurs in the center of the carbon spheres (Figure 3.6). At this pressure, diamond nucleates and grows [80], rather than forming via a diffusionless mechanism. We predict that diamond nucleates at the sphere's center and growth continues outward, until the decrease in absorption due to phase conversion of amor-

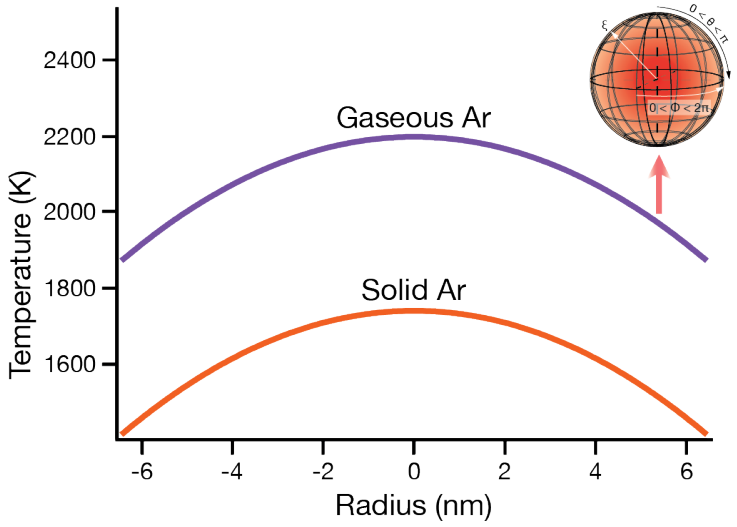

Figure 3.6: Temperatures calculated within a single amorphous carbon sphere with a refractive index of 1.5 - 1.0i and thermal conductivity of 0.05 $Wm^{-1}K^{-1}$ in supercritical argon (refractive index 1.6) at 18 $MWcm^{-2}$ for solid and gaseous argon (c). To account for sphere-sphere heating, we set to 1380 K, the melting point of argon at 16.3 GPa. Based on analysis of TEM images (Figure 3.5a), we modeled the carbon aerogel as spheres with 12.9 nm diameters. The iterative solutions for gaseous and solid argon yielded thermal conductivities of 0.066 $Wm^{-1}K^{-1}$ and 0.88 $Wm^{-1}K^{-1}$, respectively. The inset shows the coordinate system for temperature calculations within a single amorphous carbon sphere upon irradiation from the bottom of the sphere.

phous carbon (n=1.5-1.0i) to diamond (n=2.4-0.0i) inhibits further conversion. This process traps N_s defects, which can later be converted to NV^-, and coats the surface in the graphitic or amorphous carbon found in Raman scattering and previously observed via x-ray absorption.

3.7 Conclusions

Progress in the development of nanodiamond materials for quantum computing and sensing applications increasingly relies on improving synthetic methods to enable precise control in the formation of point defects in the nanodiamond's crystal lattice. Experimental and theoretical results presented here show that nanodiamond formation from carbon aerogel

can occur at 1800 K and 16.3 GPa. A combination of Mie theory and analytical heat transport predict that nanodiamond synthesis occurs after the argon pressure medium melts to form a supercritical fluid with low thermal conductivity. The thermal insulation from the supercritical argon causes rapid local heating of the carbon aerogel, likely leading to nucleation at the center of amorphous carbon grains, and subsequent radial growth until conversion to diamond limits further heating. Eliminating glassware during sol-gel synthesis suppressed the formation of SiV^- centers, allowing the production of defect free diamond. This sets the stage for the controllable reintroduction of color centers back into diamond. In addition, the temperature-dependent formation of NV^- centers and $CB\Omega$ model suggest that nitrogen initial incorporates substitutionally and subsequent vacancy diffusion drives the formation of NV^-. The low thermal conductivity of carbon aerogel enables the highest reported resolution of phase conversion of amorphous carbon to diamond with a spatial resolution of 4 μm. The methodology presented here opens the door to diamond synthesis below the diffraction limit through high-resolution photothermal phase control [7].

Chapter 4

BOTTOM-UP, MOLECULAR DOPING OF NANODIAMONDS

4.1 Introduction: applications and challenges of dopants in diamond

As discussed in Section 2.2, the characterization and manipulation of dopants in diamond has generated a wide range of applications spanning quantum computing, sensing, and cryptography [32, 33], the determination of interstellar origin in meteoritic samples [34–36], and biolabeling [23], due to the remarkable properties of the diamond host[1]. The dense diamond lattice exhibits a negligible immune response, maintains a wide band gap, and, notably, restricts heteroatom defect diffusion at temperatures far above the diamond-graphite phase line at atmospheric pressure. While the low diffusion coefficient of the diamond lattice represents a challenge for doping diamond, it is a boon for applications, where defect stability enables highly fidelity quantum sensing and the fingerprinting of presolar nanodiamond. For example, the isotopic abundance of noble gasses and nitrogen atoms in nanodiamond has allowed for characterization of supernova and presolar accretion disk formation [35, 36, 95].

Across these applications, ion implantation remains the dominant method to introduce dopants into diamond because it can deterministically generate single heteroatom color centers and overcome the diamond's low diffusion coefficient. In addition, the ion implantation of single heteroatomic dopant species has no atomic restrictions: accelerated noble gasses work just as well as accelerated transition atoms. These are not just academic goals. Defects across the periodic table, including noble gasses for color centers for quantum applications and enable to study of presolar nanodiamonds. We note with great foreshadowing that, despite the critical role of noble gas in nanodiamond, there are no studies regarding the

[1]This chapter is in preparation and will be published. It is comprised of work from Matthew J. Crane, Alessio Petrone, Ryan Beck, Matthew B. Lim, Xuezhe Zhou, Xiaosong Li, Rhonda M. Stroud, and Peter J. Pauzauskie.

conditions that lead to noble gas incorporation within the lattice at HPHT conditions [95, 96].

The results in Chapter 3 demonstrated that removing dopants from carbon aerogel precursors prevented the formation of silicon dopants in nanodiamond produced by HPHT conditions. While intuitive, those experiments were an important proof of concept. In this chapter, we leverage those results to deterministically incorporate silicon atoms into the diamond material as SiV^- centers by introducing a silicon-containing small molecule into the carbon aerogel precursor. We propose a bottom-up methodology to dope diamond by first synthesizing a doped amorphous carbon precursor and then converting it to diamond at HPHT conditions in a noble gas environment. This allows us to integrate the desired dopant into carbon while it is thermodynamically stable with traditional synthetic chemistry techniques, rather than rely on ion implantation into a metastable diamond substrate and investigate noble gas incorporation at HPHT. We find that elements incorporated into a nanostructured carbon precursor remain in the recovered diamond product. In addition, pressure-dependent PL and DFT show that of SiV^- color centers can act as a pressure sensor in a laser-heated diamond anvil cell even after high temperature annealing, which damages traditional pressure sensors [97]. Finally, by employing an argon pressure media and studying the nanocrystals with EELS and EDS, we observe that the traditionally-inactive argon incorporates throughout the throughout the nano and microscale diamond product in all samples. This observation challenges the traditionally-held view that noble gas pressure media remain chemically and physically inactive throughout HPHT experiments, even after recovery at atmospheric conditions. Most importantly, this allows us to tune dopants across the full range of the periodic table without ion implantation for the first time, and, we anticipate, will open the door to a wide range of new designer dopants.

4.2 Materials and methods

4.2.1 Doped carbon aerogel synthesis

We synthesized carbon aerogels by adding resorcinol (Sigma-Aldrich, St. Louis, MO, USA), formaldehyde (37 wt-% methanol-stabilized aqueous solution, Sigma-Aldrich), and hydrochloric acid (37 wt-%, Macron, Center Valley PA, USA) to acetonitrile (EMD Millipore, Billerica MA, USA) to achieve a molar ratio of resorcinol to formaldehyde, hydrochloric acid, and acetonitrile of 1:2, 8.4:1, and 1:76. For silicon-doped carbon aerogel, we added tetraethyl orthosilicate (98 wt-%, Acros Organics) at a final molar ratio of 4.5×10^{-9} M. We transferred the solution to a Branson 1510R-DTH ultrasonic cleaner until the gel turned a light pink and solidified, typically 30 minutes. We then exchanged the acetonitrile solvent with ethanol 4 times over 5 days and dried the gel with supercritical CO_2 in an autoclave (E3100, Quorum Technologies, Laughton, East Sussex, UK) to prevent pore collapse due to capillary pressure. Finally, we pyrolyzed the gels at 1000 °C for 4 hours to remove oxygen moieties from the gel.

4.2.2 High pressure, high temperature synthesis

To achieve HPHT conditions, we employed a laser-heated Boehler-Almax plate DAC with 0.300 mm diameter culets. First, we dimpled a rhenium gasket from 250 μm to 30 μm and drilled an 80 μm hole in the center of the gasket using an electronic discharge machine to form the walls of the high-pressure chamber. We then returned the gasket to the DAC and used a Marzhauser Wetzlar nanomanipulator equipment with a tungsten probe to transfer carbon aerogel and finely-ground ruby crystals into the DAC's cavity. The carbon aerogel and ruby act as a diamond precursor and pressure monitor, respectively. To remove adsorbed species from the aerogel, we placed the DAC into a sealed chamber and flowed argon over it for at least 30 minutes. Afterward, we used liquid nitrogen to condense the flowing argon and subsequently tightened the DAC to trap liquid argon in the DAC's chamber. By condensing liquid argon from an argon environment, we infiltrate the carbon aerogel precursor's pores

with gaseous and then liquid argon to maintain the aerogel pore structure as much as possible.

We laser heated the DAC using a ytterbium-based, 1070 nm IPG photonics YLR laser focused with a NIR-corrected Mitutoyo 50x objective (0.55 NA). The laser rapidly heated the aerogel precursor, and we simultaneously collected Planck emission from 250 to 900 nm with a fiber-coupled Ocean Optics USB2000 spectrometer and 1000 nm dichroic mirror, which was calibrated with an Optics HL-2000. To calculate temperatures, we fit the wavelength- and intensity-corrected spectra with Wien's Law and used this solution as the initial guess for a full nonlinear Planck's solution in Matlab. We collected Raman and PL using a home-built microscope comprised of a Coherent compass 532 nm laser, a Mitutoyo 50x objective (0.55 NA) and an Acton SpectraPro 500i with a Princeton Instruments liquid nitrogen-cooled detector. In addition, we measured some Raman data with a Renishaw inVia system equipped with a Leica DMIRBE inverted microscope and a 785 nm excitation source.

4.2.3 Microscopy methods

Scanning transmission electron microscopy, including high-angle annular dark-field imaging, was performed with a Nion UltraSTEM 200X operated at 60 kV. This instrument is equipped with a Gatan Enfinium ER energy loss spectrometer, and a Bruker XFlash100, 0.7sr energy dispersive X-ray spectrometer. The nominal probe conditions were 50 pA -100 pA with a 0.15 nm probe. For carbon core loss fine structure determination, a dispersion of 0.05 eV/ch was used, which provided an energy resolution of 0.4 eV, as measured by the FWHM of the zero loss peak. Transmission electron microscope bright field images and selected-area electron diffraction were taken on an FEI Tecnai G2 F20 at an accelerating voltage of 200 kV.

4.2.4 Computational methods

Computational studies were performed using the Gaussian electronic structure package [98]. A nearly spherical $C_{119}SiH_{104}$ nanodiamond (~1.2 nm in diameter) was constructed with a bulk fcc lattice parameter of a = 0.357 nm [99] and hydrogen atoms were used to passivate

the surface carbon atoms and to saturate surface dangling bonds, according the procedure presented in the Reference [84].

The SiV center in diamond consists of a silicon atom and a vacancy in a split-vacancy configuration [100, 101]. The SiV center was thus created by removing two carbon atoms near the center of the nanodiamond along the $< 1, 1, 1 >$ axis of the model, and positioning the silicon at the center of the resulting divacancy in a local D3d environment, as observed in previous computational studies [102–104]. In this work, we focus on the reduced SiV^- center, whose ground state has been shown to be a doublet. The ground-state electronic structures were obtained by solving the Kohn-Sham equation using the hybrid Becke, 3-parameter, Lee-Yang-Parr (B3LYP) density functional [105–107] with a 6-31g(d) basis set. This theory level has been previously validated for the description of the electronic structure and optical properties of both pure and nitrogen vacancy doped nanodiamonds of the same dimensions [84]. Several models were prepared to investigate the effect of uniform hydrostatic pressure by shrinking the lattice parameter uniformly using the lattice constants from Reference [108].

4.3 Bottom-up synthesis of silicon and noble gas dopants

To study the incorporation of dopants at HPHT conditions, we synthesized a nanostructured carbon aerogel precursor with a controlled chemical composition, and subjected it to HPHT conditions in a laser-heated DAC with an argon pressure medium, as shown in Figure 4.1 [56, 73]. BF-TEM and SAED in Figure 4.1 demonstrate that the aerogel consists of 6.8 ± 1.9 nm amorphous carbon grains. We tuned the chemical composition of the aerogel grains by adding TEOS molecules directly to the mixture as it gelled (Figure 4.1a). EDS confirmed that silicon dopants were incorporated throughout the carbon precursor material. To synthesize diamond, we placed the doped carbon precursor into a diamond anvil cell and condensed solid argon within the high-pressure chamber to infiltrate the microstructure of the aerogel (Figure 4.1b). We subsequently pressurized the cell above 20 GPa to thermodynamically favor diamond formation and drove grain growth by heating above 2000 K with a near-infrared, continuous laser (Figure 4.1c) [67].

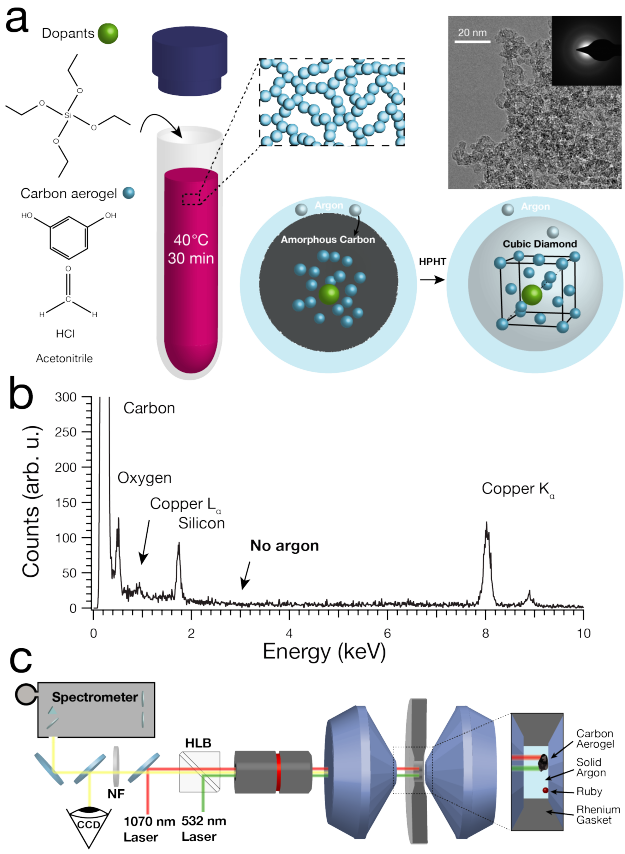

Figure 4.1: Carbon precursor doping mechanism and characterization. (a) Schematic representing the synthesis and doping of carbon aerogels, including BF-TEM image with SAED inset. Dopants are introduced alongside resorcinol and formaldehyde incorporate within the carbon aerogel grains. Upon conversion to diamond at high pressure and high temperature, dopants remain inside the diamond lattice as color centers. (b) EDS spectra of the carbon aerogel as synthesized show only the presence of carbon, silicon, and oxygen. Copper signal comes from the TEM grid. (c) Schematic showing a 1070 nm heating laser or polarized 532 nm Raman and photoluminescence laser focused into the pressurized diamond anvil cell, which is loaded with a carbon aerogel precursor, ruby for pressure measurements, and a solid argon pressure media, contained by a rhenium gasket.

To characterize the recovered material, we examined BF-TEM, SAED, and EELS. We found that the recovered material exhibited nanocrystalline domains with interlayer distances corresponding to cubic diamond (Figure 4.2b). The nanodiamond grain sizes ranged from 1 - 200 nm, indicating that significant carbon diffusion occurs during HPHT synthesis, which was likely enhanced by the high synthesis temperatures that surpass the melting point of argon at 20 GPa (1580 K) [72]. The carbon K-edge EEL spectra of pure diamond has a characteristic near-edge structure with prominent σ^* peak at 290 eV a dip at 302.5 eV [109].

The carbon K-edge spectrum of the recovered material contained both features, further indicating that the HPHT treatment formed cubic diamond, as well as a small pre-edge peak at 285 eV. This pre-edge feature corresponds to a π^* excitation associated with sp^2 carbon [35, 109]. Raman scattering from the recovered material exhibited peaks related to cubic diamond (A_{1g}, 1332 rel cm-1) and sp^2 carbon (E_{2g}, 1600 rel cm-1) [77]. As observed in previous HPHT and CVD experiments, this sp^2 carbon likely stems from nanodiamond surface reconstruction and incomplete sample heating due to the self-limiting absorption of amorphous carbon as it converts to diamond [56].

EDS and EEL spectroscopy allow us to measure the chemical composition of the recovered nanodiamond and confirm the presence of dopants, including nitrogen, silicon, and argon. The Z-contrast of STEM-HAADF images identify individual atoms and clusters (Figure 4.2a). Combined, these data unambiguously demonstrate that silicon dopants added to the carbon aerogel precursor remain in and/or on the nanodiamond product after heating, despite significant grain growth. The presence of argon within the recovered material, despite decompression to atmospheric pressure, transfer to a TEM grid, and analysis at ultrahigh vacuum conditions, demonstrates robust incorporation within the diamond lattice, rather than surface adsorption.

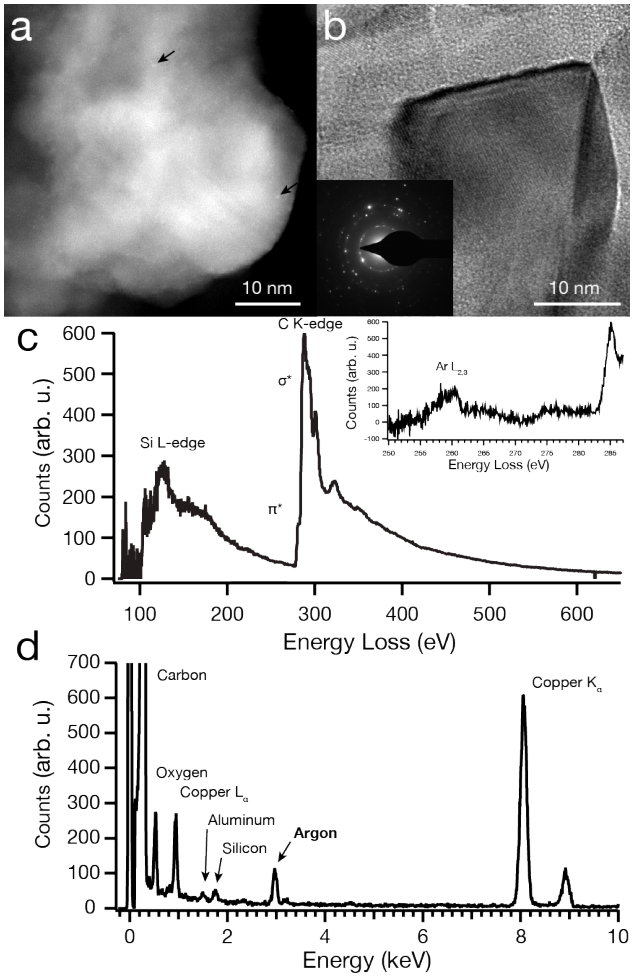

Figure 4.2: Structural and chemical characterization after HPHT synthesis. (a and b) STEM-HAADF and BF-TEM illustrate the microstructure of the recovered diamond material. Arrows in the STEM-HAADF image point out example impurity atoms (mostly argon and silicon), and the inset in panel (b) contains SAED, corresponding to diamond. In addition, (b) exhibits 2.08 Ålattice spacings. Index SAED shows d spacings (miller indices) of 2.08 Å(111), 1.27 Å(220), 1.08 Å(311), 0.89 Å(311), 0.83 Å(311), and 6, 0.74 Å(422). (c and d) STEM-EELS and STEM-EDS of the region displayed in (a) showing the silicon L-edge and carbon K-edge, and elemental composition, respectively. The small concentration of aluminum likely comes from trace amounts of ruby during laser heating. The Cu peak is from the sample grid and STEM pole piece. The inset in panel (c) displays the carbon pre-edge features and the argon $L_{2,3}$ peak.

4.4 Argon dopants and implications for high pressure experiments

We observed argon in all recovered samples synthesized at a range of pressures and temperatures from 20 to 25 GPa and 1800 to 3000 K. While other reports have demonstrated the effect of noble gas pressure media on samples at elevated pressures, such as partitioning of helium in SiO_2 [110], this is the first confirmation of noble gas incorporation and recovery from HPHT [111]. These results suggest that the aerogel structure allows argon to incorporate within its micropores during compression and that grain growth during laser heating traps these atoms within the lattice. For optoelectronic color center applications in diamond, this represents a new methodology for the incorporation of noble gas defects, e.g. xenon, for quantum computing and sensing [112]. In addition, noble gas pressure media are almost exclusively used in HPHT experiments because they remain hydrostatic to high pressures and are chemically and physically inert [113]. The incorporation of noble gas pressure media into materials at HPHT conditions challenges the view of complete inactivity, and could explain hysteresis effects in prior DAC experiments [114]. It could also provide an explanation for how noble gas atoms are incorporated into nanodiamonds in astrophysical environments.

4.5 Silicon-vacancy photoluminescence and applications for optical metrology

The PL spectra of all the recovered material contain optically-active color centers from NV centers (Figure 4.3). The shoulders at 575 and 637 nm and the broad feature centered at 700 nm are uniquely characteristic of NV^0 and NV^- ZPLs and phonon side bands, which have been observed in multiple HPHT reports due to atmospheric N2 incorporation [56, 83]. PL signal from the argon is neither observed nor expected [115]. However, the silicon-doped carbon aerogel contains a peak at 739 nm, corresponding to the SiV^- color center, that is not present in undoped carbon aerogel [116]. These observations confirm that dopants added to the carbon aerogel precursor persist within the nanodiamond lattice and provide a new mechanism for engineering dopants in diamond. Both SiV and NV are lower energy states than their substitutional silicon and nitrogen counterparts due to lattice relaxation,

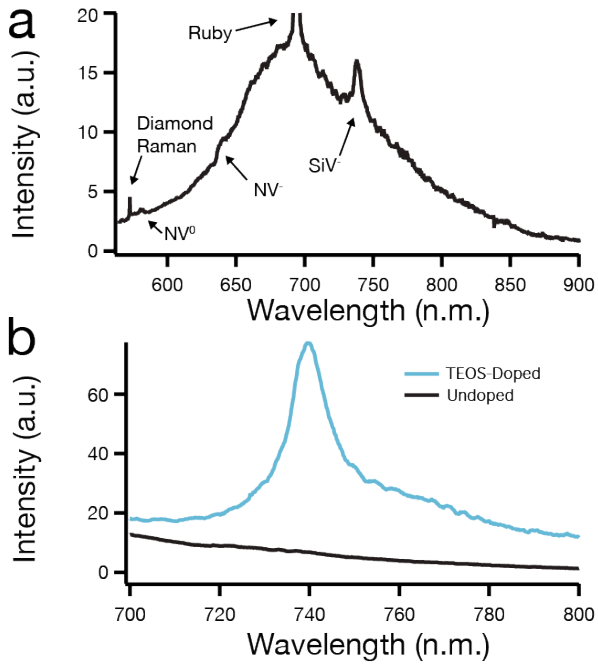

Figure 4.3: Photoluminescence of color center. (a) Photoluminescence and Raman scattering of recovered nanodiamond synthesized from the TEOS-doped carbon aerogel after depressurization and removal from the DAC. Labels denote diamond Raman scattering, and NV^0, NV^-, and SiV^- color center ZPLs. (b) High resolution spectra of the SiV^- region comparing TEOS-doped and undoped carbon aerogels.

as observed in Jahn-Teller distortion of the lattice [103, 117]. Unlike ion implantation, which requires annealing to drive vacancy diffusion to activate incorporated heteroatoms, optically-active color centers form immediately upon HPHT conversion to diamond. This suggests that as the diamond lattice forms around the heteroatomic silicon and nitrogen atoms, the lowest energy structure forms immediately. While silicon atoms have been doped into diamond before, the process involved ion implantation or complete chemical breakdown in a plasma which limited controllable heteroatom defect formation [33]. This bottom-up approach illustrates the possibility of a new doping paradigm for diamond where molecular dopants can be designed with the precise heteroatomic stoichiometry and three-dimensional stereochemistry to create a wide range of multifunctional polyatomic point defects. Future studies will track the ultimate location of atoms from a single small molecule upon conversion to diamond. These investigations will clarify whether dopants remain kinetically trapped in the diamond lattice or diffuse significantly during the phase transformation—that is, whether the final defects reflect the stereochemistry of the small molecule or not.

As discussed above, color centers in diamond are attractive materials for optical sensing applications due to their high stability in the chemically inert diamond lattice [83]. Due to its narrow linewidth, the SiV^- center may act as a high-resolution pressure sensor. To evaluate the defect for optical pressure metrology and illustrate the efficacy of bottom-up doping, we collected pressure-dependent photoluminescence (Figure 4.4a) spectra, which reveals a 0.95 meV/GPa slope from 0 to 25 GPa. We employed ab initio calculations to model the pressure-dependence of the SiV^- by fully simulating a nearly-spherical $C_{119}SiH_{104}$ nanodiamond (1.2 nm in diameter) containing a SiV^- defect under the effect of the uniform hydrostatic pressure with density functional theory using the —Gaussian electronic structure package [98]. These theoretical results predict a 0.8 meV/GPa shift from 0 to 25 GPa, in close agreement with experimental observations. Extending the simulation up to 140 GPa demonstrates the viability of optical pressure metrology with SiV^- to high pressures. To date, the high quantum efficiency, narrow linewidth d–d transitions of Cr^{3+} in alumina (ruby) have made it the nearly-ubiquitous choice to measure pressure at high pressure DAC experiments

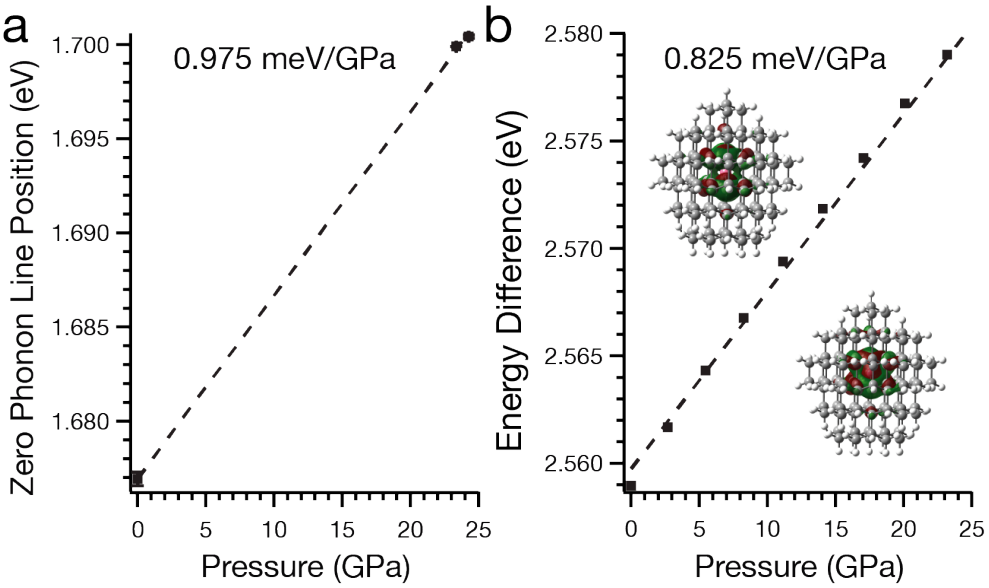

Figure 4.4: Evaluation of SiV^- center for optical pressure manometry. (a) Experimental SiV^- ZPLs and (B) the B3LYP/6-31G(d) average energy differences of the molecular orbitals which exhibit largest contributions to the absorption peak responsible for the ZPL at different pressures. Error bars for both pressure and ZPL energy sit within the circular markers. The insets in (b) illustrate the contour plots (0.025 isodensity) of the LUMO (top) and the HOMO-2 (bottom) molecular orbitals (the largest contribution) of a SiV^- containing nanodiamond ($C_{119}SiH_{104}$), oriented perpendicular to the diamond <1,1,1> axis, as modeled with DFT. White, grey, and pink atoms are hydrogen, carbon, and silicon, respectively.

[118]. However, ruby undergoes a phase transition at 94 GPa at 1300 °C [119], making it unsuitable for the next generation of HPHT experiments, which have recently reached the terapascal range [120]. On the other hand, diamond is the thermodynamically-stable polytype of carbon at all temperatures pressures above 1 GPa until melting [67]. The lack of phase transformation suggests that SiV^--doped nanodiamond may succeed at conditions where ruby fails.

4.6 Conclusions

The rational incorporation of silicon by doping the carbon precursor with TEOS and argon by employing an argon pressure media into nanodiamond illustrate the potential impact

of this doping methodology for doped nanodiamond applications, like pressure metrology, without ion implantation. Rather than synthesizing diamond and subsequently introducing heteroatoms with ion implantation, vacancy center annealing, and confocal searches for color centers, the HPHT conversion of doped carbon can directly form color centers. For single-defect applications, this research opens the door to the incorporation of more complex defects into diamond with structures defined by the chemical dopant added into the carbon precursor. If diamond nucleates prior to dissociation of the dopant, defects could be added with chemical precision limited only by molecular synthesis. For extraterrestrial nanodiamonds, where dopants in diamond are used to fingerprint the presolar and interstellar environment, this demonstration unveils the DAC as a tool to study HPHT doping that could occur in astrophysical environments [35, 36]. Given the prevalence of noble gas pressure media, these results have broad implications for high pressure experiments, where, to date, noble gasses have been considered inert [110, 113].

Chapter 5

SYNTHESIS OF A NOVEL PHASE OF CARBON, PBAN-CARBON

5.1 Introduction to exotic allotropes of carbon

The wide number of bonding configurations (sp, sp^2, and sp^3) and the range of kinetic pathways enable elemental carbon to form many stable allotropes, dictated by the precursor and synthetic conditions[1] [54, 56, 59, 69, 121–127]. For example, while the static compression of sp^2 graphite forms diamond at high temperatures, the static compression of layered sp^2 carbon onions forms nanotwinned diamond [123, 128]. On the other hand, cold compression of graphite produces interlayer bonding to generate monoclinic, M-diamond, and cold compression of sp^2 benzene drives a Stone-Wales reaction that yields nanodiamond threads [54, 124]. For M-diamond, the sluggish kinetics of the phase transitions allowed it to elude final identification for 50 years after it was first reported [127]. Similarly, rapid heating and non-equilibrium conditions can modify phase transformation kinetics to create previously-unidentified carbon phases, such as carbon nanotubes, buckminsterfullerenes, Q-carbon, and BCC carbon [129–131]. While challenging to control, the fruits of this carbon labor have generated widespread interest across fields, including electronic materials[132–134], single photon emitters[51, 69, 135], ceramics, and even astrophysics through the fingerprinting of solar system formation with extraterrestrial diamond [35, 136]. Despite extensive study, the number of theoretically-proposed carbon phases still drastically outnumber the experimentally-observed phases, including theoretical metallic, superdense, and cage-like carbons phases [137–144].

---

[1]This chapter is in preparation and will be published. It is comprised of work from Matthew J. Crane, Rhonda M. Stroud, and Peter J. Pauzauskie.

Here, we present the formation of a new, metastable, nanocrystalline phase of carbon, which we tentatively name Pban-carbon, produced by the rapid heating of amorphous carbon grains under hydrostatic compression by solid argon. To synthesize Pban-carbon, we used carbon aerogel as a precursor material. Carbon aerogel is a nanostructured, low density, and highly absorbing network of amorphous carbon grains [56, 69]. We loaded individual grains of carbon aerogel into a DAC and condensed argon within the gel to act as a hydrostatic pressure medium. HR-TEM images illustrate the aerogel grain size and fractal network, which creates a low thermal conductivity, highly absorbing material [74, 75]. Upon step irradiation with a high power, NIR laser, the compressed carbon rapidly heats to temperatures between 2000 and 3000 K [67]. The high temperature was maintained for 2-30 s.

5.2 Materials and Methods

The carbon aerogel synthesis was identical to the method describe in Sections 3.2 and 4.2 with the exception that no dopants were added to the aerogel. As in the previous methodology, we employed a laser-heated Boehler-Almax plate DAC with 0.300 mm diameter culets. To pressurize the carbon aerogel, we first dimpled a rhenium gasket from 250 μm to 30 μm and drilled an 80 μm hole in the center of the gasket using an electronic discharge machine to form the walls of the high-pressure chamber. We then returned the gasket to the DAC and used a Marzhauser Wetzlar nanomanipulator equipment with a tungsten probe to transfer carbon aerogel and finely-ground ruby crystals into the DAC's cavity. Finally, we condensed argon around the aerogel and sealed the chamber to a pressure of 24 GPa, as measured with the ruby pressure scale [86].

For laser heating, we employed the same ytterbium-based, 1070 nm IPG photonics YLR laser focused with a NIR-corrected Mitutoyo 50x objective (0.55 NA) as described in Section 4.2. However, during heating, we increased the beam power to between 30 and 60 W and directly exposed the beam onto the carbon aerogel to rapidly increase its temperature. We refer to this as “step” heating, rather than ramp heating, where the laser is exposed to the carbon aerogel as the power is increased. This caused the argon to immediately melt,

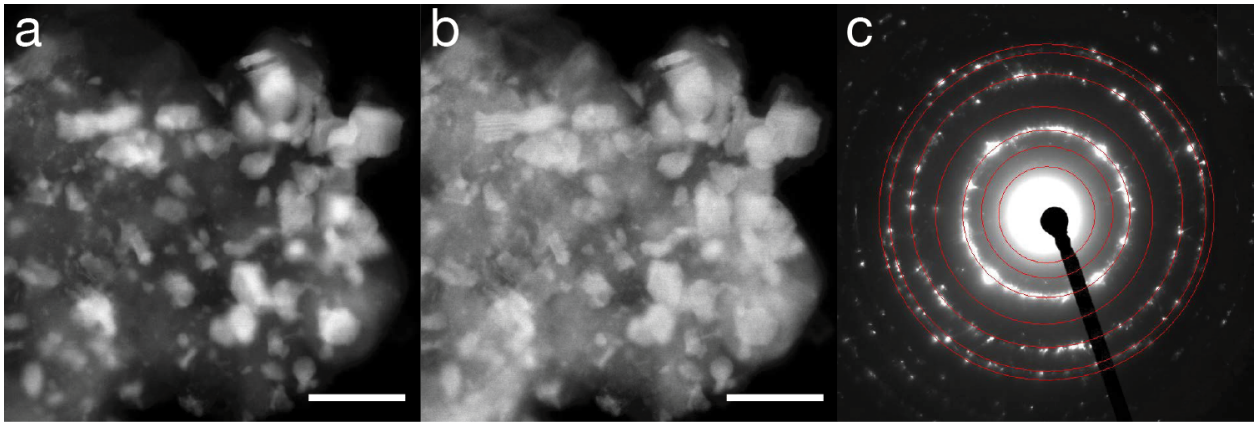

Figure 5.1: STEM-HAADF (a), STEM-MAADF (b), and SAED of the recovered material (c). Diffraction peaks index to Pban-carbon and correspond to d-spacings (miller indices) of 3.12 Å(110), 2.70 Å(111), 2.38 Å(002), 1.93 Å(121), 1.38 Å(113, 310), and 1.19 Å(203, 040).

decreasing its local conductivity, and insulating the carbon aerogel to reach 3000 K quickly. While the initial goal was to limit graphitization of the carbon during the irradiance ramp, this rapid heating appears to have generated both cubic diamond and Pban-carbon, as discussed below.

The microscopy methods, including Raman, photoluminescence, and TEM were identical to those discussed in section 4.2.

5.3 Results and discussion

After step heating of the carbon aerogel with a power of at least 30 W, Raman spectra show the presence of a number of previously-unidentified peaks between 100 and 1100 (Figure 5.2) cm^{-1} [77, 145]. Typical carbon Raman contains features at 1332, 1350, and 1600 cm^{-1}, corresponding to cubic diamond, disordered sp^3, and sp^2 carbon [145].

STEM-EEL spectra of the recovered material demonstrate that the carbon bonding is largely sp^3, indicative of diamond-like material [35, 69, 109]. Indeed, d-spacings and SAED show that much of the amorphous carbon converted to cubic diamond (Figure 5.1). However, despite the uniform, crystalline sp^3 carbon bonding, Z-contrast from STEM-HAADF and

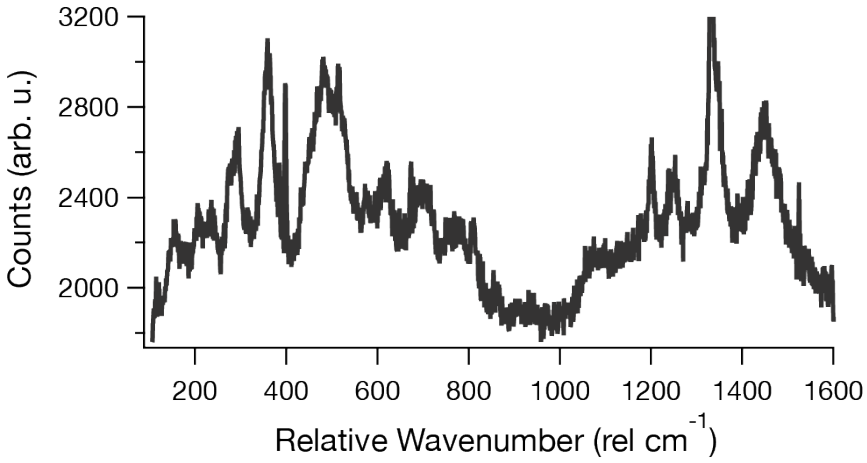

Figure 5.2: Raman scattering collected from the recovered material after rapid "step" heating with a 785 nm excitation source.

MAADF images illustrates significant differences in scattering between grains embedded in the diamond matrix.

The nanoscale changes in Z-contrast suggest the presence of non-cubic diamond phases with different densities. HR-STEM images show that the recovered crystalline material has d-spacings of 2.45, 2.36, and 2.08 Å, larger than the d-spacings of cubic diamond and, to the best of our knowledge, unrelated to other known diamond allotropes (Figure 5.3). Pban-carbon matches these d-spacings. This phase was first identified by Jose Fayos (termed "diamd_cr44_ch") and has since been found in evolutionary molecular modeling searches of carbon [138, 144]. It has a rhombohedral unit cell with lattice constants of 4.13, 4.94, and 4.82Åand Pban space group symmetry [138]. In addition, Pban-carbon has cage-like motifs (Figure 5.4).

To characterize the electronic properties of Pban-carbon, we used DFT implented in Quantum Espresso [146]. After relaxing the structure, the phonon density of states calculations illustrate a range of active Raman modes below 1100 cm^{-1}, matching our observations 5.2. In addition, the band structure and fermi energy calculations suggest that the Pban-carbon phase is semimetallic at room temperature with an indirect band gap (Figure 5.5).

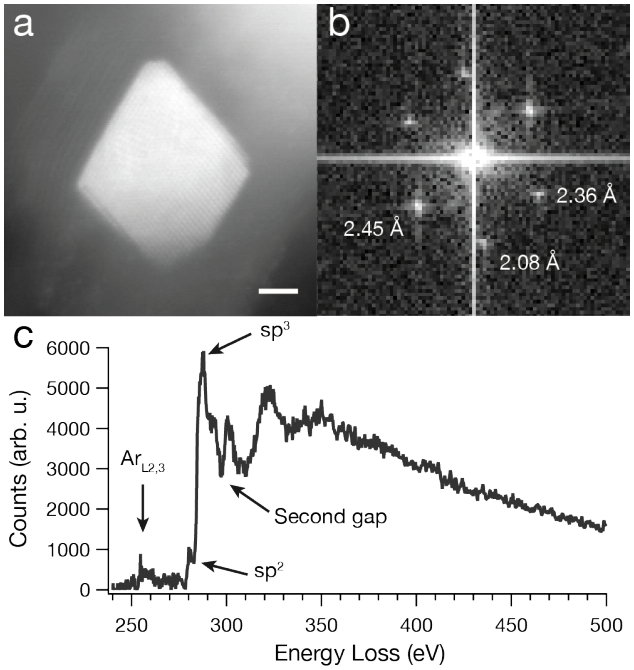

Figure 5.3: High-resolution STEM-HAADF image of Pban-carbon (a) and the corresponding fast Fourier transform (b) and EELS (c) of the dense inner region.

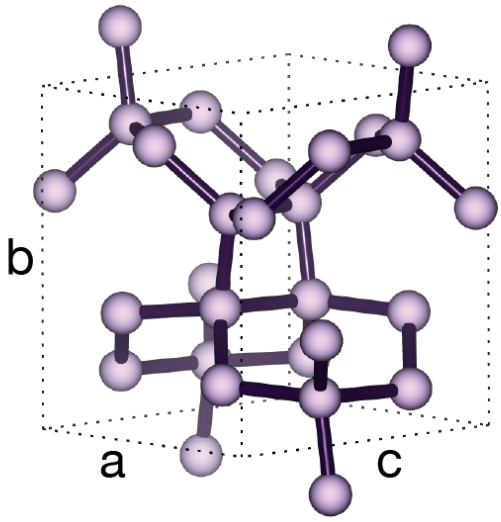

Figure 5.4: High-resolution STEM-HAADF image of Pban-carbon (a) and the corresponding fast Fourier transform (b) and EEL (c) of the dense inner region

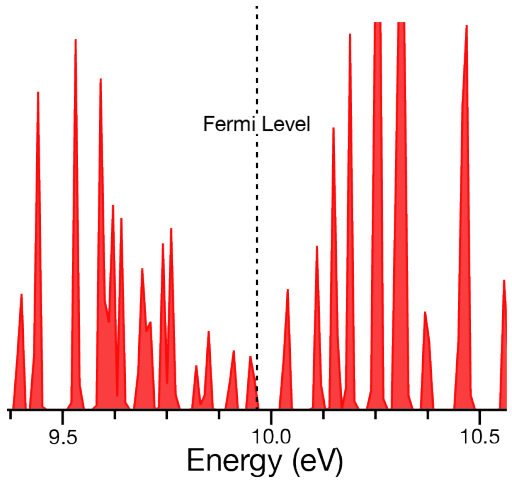

Figure 5.5: Electronic density of states of Pban-carbon calculated with Quantum Espresso.

However, we note that relaxing the lattice structure did modify the atomic location and lattice constants slightly. Thus, the DFT electronic and vibrational predictions should be taken with a grain of salt and warrant further investigation.

Interestingly, STEM-EEL spectra of the recovered material reveal the presence of argon dopants contained with the Pban-carbon phase (Figure 5.3). EEL spectra collected across the entire available range do not show the presence of any atoms other than argon and carbon. The argon, in part, accounts for the increased Z-contrast within the Pban-carbon phase grains. It may also explain the inability of DFT to perfectly reproduce the proposed lattice structure. The cage motifs within proposed Pban-carbon lattice may enclose the argon atoms as interstitial defects. In addition, extensive research on dopants in cubic diamond have found that heteroatomic dopants in the diamond lattice have extremely low diffusion coefficients [28]. This has enabled the fingerprinting of noble gasses in interstellar and pre-solar nanodiamonds as well as highly stable, single photon emission for quantum computing and sensing [34–36, 147]. Thus, argon atoms may also incorporate as substitutional defects in Pban-carbon. If the argon atoms dope interstitially, it is conceivable that they stabilize the Pban-carbon phase. Similar previous syntheses did not observe the Pban-carbon phase

[56]. However, they also did not employ an argon pressure medium and used ramped, rather than stepped, laser heating.

This stepped heating may enable rapid formation of sp^3 carbon from amorphous carbon without producing long-range graphitic grains. As originally predicted, Pban-carbon stems from a kinetic pathway where graphite forms interlayer bods in either a chair or boat configuration. Boat structures traverse a kinetic pathway to diamond; chair structures traverse a kinetic pathway to other proposed phases, including Pban-carbon and hexagonal diamond [80, 138]. Variations of this proposed interlayer bonding mechanism for cubic diamond formation have been observed in a range of theoretical predictions [80, 126]. When amorphous carbon is heated by a ramped NIR laser, graphite is observed far above the Berman-Simon, graphite-diamond coexistence line, and often forms at low temperatures [67, 148]. Thus, heating by ramping the temperature likely produces more, larger graphitic grains that subsequently yield diamond at longer time scales. On the other hand, analytical heat transport suggests that stepped heating allows carbon to reach steady state within ~50 ps, on the time scale of diamond nucleation. We hypothesize that this rapid heating modifies this kinetic pathway to form Pban-carbon.

We also note that the Raman spectra varied significantly across each chunk of the aerogel, which suggests that the high thermal gradients may have produced different phases across each grain of aerogel. As discussed in Section 3.4, the Gaussian heating beam contains a massive variation in intensity across its ~1 μm diameter [7]. This large variation in intensity produces a similarly extreme temperature gradient, which is further amplified by the high thermal conductivity of solid argon and diamond anvils outside of the supercritical argon bubble. During decompression, the samples in the chamber shift significantly. In addition, the temperature-dependence of Planck emission biases fits to the highest temperature. For these reasons, it is challenging to correlate individual heating events with microscopy. However, scanning confocal Raman demonstrates that the strange sub-1100 cm^{-1} peaks occur more frequently at the surface of the carbon aerogel, where thermal gradients are greatest. This further suggests that rapid step heating and high thermal gradients modify the kinetics

of phase transformation to produce Pban-carbon. Because of the nanocrystalline grain size, the energy of the surface states may also heavily impact the phase transformation kinetics, as observed in nanodiamond and quantum dot metastability [149, 150].

5.4 Conclusions

The synthesis and observation of a super-dense, carbon phase with cage-like motifs, validates a wide body of theoretically-proposed carbon phases and opens the door for many potential applications. These include a new host for single-photon emitters, a material for heteroatom storage and migration, such as membranes for chemical separation or electrodes for batteries, and unprecedented, hard ceramics or glasses. In addition, the presence of noble gas atoms within the suggests that the Pban-carbon phase may be present in meteoritic nanodiamond samples, where mesostructured carbons both contain noble gasses and experience HPHT conditions. The observation of Pban-carbon in meteoritic carbon samples would provide a new mechanism to fingerprint the precise history of a meteor. Finally, the identification of Pban-carbon suggests that other allotropes of carbon predicted by the chair interlayer bonding of graphite may exist, motivating further studies on this kinetic pathway for the synthesis of new carbon phases.

5.5 Future directions

While the observation of a new carbon phase is exciting, additional theoretical and experimental investigation is needed to clarify the formation conditions further. Experimental investigation should focus on rationally reproducing the high thermal gradient environment that generated Pban-carbon and, if possible, femtosecond time scale observation of the phase transformation. I suggest NIR pulsed laser heating at high pressures in a diamond anvil cell correlated with high energy, time-dependent in situ X-ray diffraction at, for example the advanced light source beamline 12.2.2. Similarly, varying the pressure media will systematically determine the role of argon in Pban-carbon formation. More advanced theoretical calculations will also elucidate the crystal structure, more accurately correlate Raman scattering to

vibrational modes, and verify the band structure of Pban-carbon.

Chapter 6

OPTICAL TRAPPING, TEMPERATURE MEASUREMENTS, AND ASSEMBLY OF NANOCRYSTAL-NANOWIRE HETEROSTRUCTURES IN ORGANIC SOLVENTS

6.1 Introduction to optical trapping

As we continue to search for more room at the bottom, we have observed that confinement induces unique quantum effects and that material properties are highly-nonlinear as their size, surfaces, and morphology change at the nanoscale[1] [54, 56, 59, 69, 121–127]. Understanding these processes has led to the rational engineering of nanomaterials. However, there are relatively few processes that enable the direct manipulation of nanostructures, which has hindered the production of nano-assemblies and our ability to study single-particle processes. Optical trapping has filled that gap.

An optical trap, or laser tweezer, employs a focused light source to induce a force and to manipulate particles in three dimensions from the nano to micro scale, thereby bridging the chasm from discrete to continuous behavior [151, 152]. This technique has led to a range of unique applications across disciplines. In the biophysics community, optical traps have been used to investigate DNA replication by twisting single strands of DNA [153, 154] and to study protein folding by observing the force required to pull proteins apart [155]. In physics, the optical trap has been used to directly measure long-range hydrodynamic memory in Brownian motion [156], to measure the Casimir force between a silica sphere and a flat surface [157], and to measure the size and charge of nanoparticles in real time [158].

To manipulate particles, single-beam gradient force optical traps require high irradiances

[1]This chapter is in preparation and will be published. It is comprised of work from Matthew J. Crane, Elena P. Pandres, Patrick J. Whitham, Daniel R. Gamelin, Vincent C. Holmberg, and Peter J. Pauzauskie.

on the order of $MWcm^{-2}$, which both allows for the study of and necessitates an understanding of nonlinear effects, such as two photon absorption, to interpret results. In addition, the high irradiances in an optical trap can lead to significant heating. For materials with low absorption, such as silica beads in water, this leads to local temperatures 10-20 K (8 KW^{-1}) above bulk temperatures [159]; for materials with high absorption coefficients, such as gold nanoparticles in water, this leads to temperatures 100-300 K above bulk temperatures and superheating due to the absence of a surface to nucleate a phase transition [160] (Figure 6.1b).

I became interested in leveraging this heating to analyze high temperature, single-particle chemistries and assemble complex heterostructures from nanomaterial building blocks. However, to date, optical traps have almost exclusively employed aqueous liquid media. In fact, to date, there remains only one definitive report of optical trapping in apolar organic solvents [161]. Because most syntheses use organic solvents to produce nanomaterials that are dispersible in organic solvents, the nearly-exclusive use of aqueous trapping media broadly limits the range of particles for trapping, chemistry, and assembly. Similarly, many nanomaterials do not have facile surface bonds to prevent oxidation, which occurs rapidly in oxygen containing environments like water. The O–H stretching also causes quenching of the excited state [14]. Further, organic solvents generally exhibit low thermal conductivities (0.1 $Wm^{-1}K^{-1}$) compared to water (0.6 $Wm^{-1}K^{-1}$) to generate significantly greater temperatures in trapped particles. Optical trapping in oxygen free, organic solvents with low thermal conductivities prevents oxidation, expands the range of particles for trapping, and enables the efficient generation of high temperatures for single-particle chemistry studies.

In this chapter, we discuss the physics of optical trapping in organic media. We show that trapping in organic solvents generates high temperatures, which induces convection. This convection produces a radial confining force on the trapped particle, and prevents temperature measurements through analysis of the Brownian motion. To measure the temperatures, we disperse Mn^{2+} : ZnCdSe quantum dots (QD's), which exhibit strongly temperature-dependent photoluminescence via a Boltzmann distribution of states between the exciton

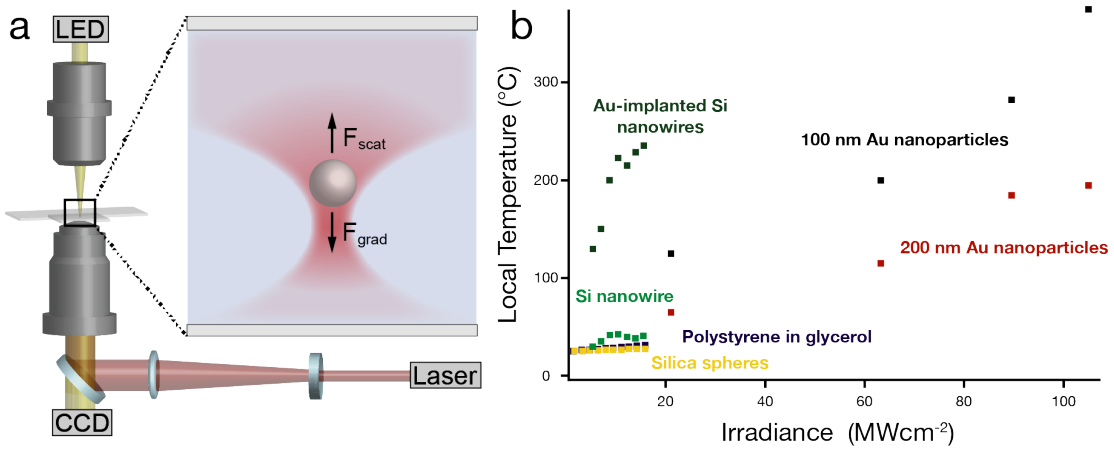

Figure 6.1: Schematic of a simple optical trap, depicting the scattering and gradient forces (a), and measured temperatures of different particles in an optical trap (b)

and Mn^{2+} energy levels. Finally, we leverage these results to align and assemble bismuth nanocrystal-germanium nanowire heterostructures.

6.1.1 Physics of optical trapping

In the most basic optical trap, a laser beam is expanded, collimated, and directed onto a high numerical aperture objective, where it is focused into a chamber containing the particles of interest to a diffraction-limited spot size. The electric field plays a twofold role to induce a force on a particle: the incident beam induces a dipole on a particle, proportional to its polarizability, α, which is attracted to the maximum of the gradient of its electric field, E,

$$F_{grad} = \frac{1}{2}\alpha \nabla E^2. \tag{6.1}$$

Photons scattered by the particle experience a change in momentum, which induces a force on the particle causing it to be displaced from the focal plane in the direction of the laser

propagation at equilibrium. This scattering force is described by,

$$F_{scat} = \frac{k^4 \alpha^4}{6\pi c n_0^3 \epsilon_0^2} I(r) \hat{z} \tag{6.2}$$

where c, k, n_0, ϵ_0, and $I(r)$ are the speed of light, the wavenumber, the refractive index of the medium, the permittivity of free space, and the irradiance. For a stable optical trap, the ratio of the gradient and scattering forces $\frac{F_{grad}}{F_{scat}}$ must be greater than unity at the focal plane. These combined forces generate a potential well to stably trap the particle.

6.1.2 Temperature measurements in an optical trap

To measure the temperature within an optical trap, we typically examine the Brownian motion of the trapped particle by collecting forward scattered light focused onto a QPD [162]. By correlating the particle's location with time, we can solve for the diffusion coefficient. Provided we know the trapped particle's morphology and dimensions, we identify the temperature through the temperature-dependence of the solvent viscosity. More specifically, during a trapping experiment, the trapped particle experiences the F_{grad} and F_{scat} forces as well as the stochastic collisions of the solvent, which produce Brownian motion. We can describe the complex motion of a trapped particle of mass, m, at position, $x(t)$, with the Langevin equation,

$$m(\ddot{x})\,(t) + \gamma_0(\dot{x})\,(t) + \kappa x\,(t) = (2k_B T \gamma_0)^{1/2} \eta(t). \tag{6.3}$$

Here, we model the optical trap as a harmonic oscillator with spring constant, κ, the motion of the particle and the Brownian force as $(2k_B T \gamma_0)^{1/2} \eta(t)$, where γ_0 is the morphology-dependent stokes drag coefficient of the trapped particle and $\eta(t)$ is the noise term. Because the characteristic time for the loss of kinetic energy due to friction is significantly below the

sampling rate, we can simplify the equation as,

$$\ddot{x}(t) + 2\pi f_c x(t) = (2D)^{1/2}\eta(t), \tag{6.4}$$

where we have defined the corner frequency, f_c, as $\kappa/2\pi\gamma_0$ and the Einstein diffusion coefficient, D, as k_BT/γ_0. To analyze the particle's location, we use a piezo stage to oscillate the trapped particle at a known frequency (velocity) and amplitude (distance). After collecting the forward scattered light with a QPD and taking the Fourier transform of the signal, this oscillation produces a spike in the resulting power spectrum, which has a frequency-dependent Lorentzian profile,

$$P_T(f) = \frac{D}{\pi^2\left(f^2 + f_c^2\right)} \tag{6.5}$$

By assuming a linear relation between the distance of the oscillation and the QPD signal, we can identify a calibration constant, $\beta_c al$, to convert volts to meters,

$$P_{response}(f) = \beta_c a l^2 P^{volts}_{response}(f) \tag{6.6}$$

This allows us to measure the diffusion coefficient in pragmatic units of $\mathrm{m^2 s^{-1}}$. Finally, we can identify the temperature by solving the equation,

$$D = k_BT/\gamma_0 \tag{6.7}$$

where γ_0 is,

$$\gamma_0 = 6\pi R\mu(T) \tag{6.8}$$

for a sphere and,

$$\gamma_0 = \frac{4\pi L}{ln\left(\frac{L}{2r}\right) + 0.84}\mu(T) \tag{6.9}$$

for a cylinder, given a temperature-dependent viscosity of the trapping solution, $\mu(T)$[163]. We recently used this technique to observe laser cooling in water by phonon-assisted anti-

stoke luminescence for the first time [6].

6.2 Trapping in organic media

6.2.1 Momentum transport

To the best of our knowledge, there is one conclusive report focused on trapping in organic solvents and three that employ apolar media, such as 2,6-lutidine or acetone [156, 157, 161, 164]. However, there are no reports of trapping in high viscosity organic solvents, of trapping nanowires in organic solvents, or of trapping materials with high absorption cross sections. When selecting new solvents, the generation of a potential well depends solely on the refractive index of the trapping media, as demonstrated by equations 6.2 and 6.1, and, thus, liquid-phase trapping is not limited to water. To date, we have successfully trapped polymer quantum dots [165] in toluene, silicon NWs in toluene, cyclohexane, and squalane, and germanium NWs in toluene and squalane, a range of m=1.021 to m=3.113. We observed two important tricks for success. First, to trap in organic media, the beam should be expanded less than for trapping water to focus the full Gaussian profile into the objective, which was also observed to improve the trapping range of highly absorbing gold nanoparticles in water [166]. Second, the particle needed to sit within a few μm of the focal plane and be initially trapped by a low irradiance beam before increasing the laser power.

In a typical trapping experiment, the laser focuses through a high numerical aperture objective into the center of a chamber containing a solution of particles. Eventually, radiation pressure from the scattering force drives a particle into the focal plane, where the gradient force traps it. During subsequent chamber motions in x, y, or z, the trapped particle remains fixed relative to other particles. The qualitative ease of this trapping process varied significantly depending on the solvent particles were dispersed in: in toluene, particles quickly flew through the trap focus; while, in squalane, they approached more slowly and settled into the potential well. Cyclohexane was intermediate between the two. In comparison, mixtures of squalane and toluene were most similar to water in behavior. These combined observations

demonstrate that, despite the presence of a static trap, the dynamic process of driving a particle into the trap is different for organic solvents. As an estimate of this difference, we consider the difference between the maximum velocity of a particle in a liquid medium,

$$v = \frac{qPR}{6c\pi w_0^2 \mu} \tag{6.10}$$

where q is the fraction of light reflected back by the particle with radius, R, P is the power of the trapping laser, and w_0 is the radius of the beam waist [167]. In order to stop a particle within the potential well of an optical trap, the laser tweezer must do work equal to its kinetic energy,

$$\int_{\infty}^{z_{trap}} F_{grad} - F_{scat} dz = \frac{1}{2} m v^2 = \frac{1}{2} m \left(\frac{qPR}{6c\pi w_0^2 \mu} \right)^2 . \tag{6.11}$$

Because toluene's viscosity is half that of water (Table 6.1), the maximum speed is twice as high and the optical trap must exert 4 times the work on the particle. In addition, the relative viscosities of the toluene (0.55 cP), cyclohexane (1.0 cP), and squalane (28 cP) reflect the observed ease of trapping trend in organic media. Interestingly, the radiation pressure from optical tweezers can print single nanoparticles onto surfaces with high precision [168]. Transitioning from water to low-viscosity organic solvents will likely decrease the powers necessary to print nanoparticles.

Table 6.1: Differences between organic and aqueous media

	Refractive Index	Density (gcm^{-1})	Viscosity (cP)	Thermal Conductivity ($Wm^{-1}K^{-1}$)
Water	$1.33 + i\ 3.48 \cdot 10^{-6}$	0.998	1.002	0.598
Toluene	$1.48 + i\ 6.16 \cdot 10^{-8}$	0.876	0.583	0.141

6.3 Heat transport and convection in an optical trap

6.3.1 Thermal properties of organic solvents

Perhaps the most glaring difference in properties when moving from water to a new solvent remains the change in thermal properties. The extensive hydrogen bonding network and high density of water impart it with a high heat capacity (4.19 $Jg^{-1}K^{-1}$) and thermal conductivity (0.60 $Wm^{-1}K^{-1}$), compared to toluene (1.72 $Jg^{-1}K^{-1}$ and 0.14 $Wm^{-1}K^{-1}$, respectively). While these characteristics of water conveniently enable life as we know it, they also provide an impressive ability to dissipate heat during optical trapping. Thus, extending trapping to organic solvents demands a more rigorous approach to heating than typically applied.

Building on previous results in the lab, we trapped silicon NWs in toluene and investigated their temperatures with the piezo method discussed in Section 6.1.2. Surprisingly, we observed that the temperature of the trapped particle decreased as the laser power increased (Figure 6.2), which is a clearly a non-inuititive and non-physical result. There are multiple possible explanations for the failure of Brownian motion-based measurements.

First, the high temperatures likely generated in the optical trap and the decreased viscosity of toluene may produce convection around the nanowire. Indeed, we observed qualitative evidence for convection based on the motion of nearby nanowires, which slowly approach the trap location throughout an experiment. This convection would induce an additional force on the sides of the NW, which decreases its radial Brownian motion and its observed diffusion coefficient. For one-dimensional structures, the calibration constant is only valid in the radial direction (x- and y-plane). Thus, convection-induced pressure would cause an apparent decrease in temperature through a decrease in Brownian motion, as we observed. Alternatively, radiation-induced pressure on the solvent flowing past an anisotropic nanowire would oppose radial diffusion. We note that further studies are necessary to clarify the magnitude of these hydrodynamic forces.

Second, Smith et al [14] found that optically-trapped silicon nanowires catalyze singlet oxygen formation via triplet-triplet annihilation of excitons generated by the trapping laser.

Singlet oxygen reacts rapidly to oxidize organic molecules. In aqueous media, singlet oxygen reactions are negligible; in organic media, singlet oxygen can react with the solvent. For example, singlet oxygen reacts with toluene to form maleic anhydride and benzoic acid [169]

$$C_6H_5CH_3 + {}^1O_2 \longrightarrow C_6H_5COOH \tag{6.12}$$

$$C_6H_5COOH + 2\,{}^1O_2 \longrightarrow C_4H_2O_3 + 3\,CO_2 + H_2O \tag{6.13}$$

Because maleic anhydride and benzoic acid have viscosities greater than toluene's, the generation of these small molecules would alter the local environment of the trapped particle. We hypothesize that the trapped silicon NW acts as a force probe of the local solution viscosity, which would decrease the measured Brownian motion with increasing irradiance, as we observed. In addition, the solubility of oxygen is approximately ten times greater in toluene than in water, which may magnify the role of singlet oxygen generation [170].

Finally, employing organic media may dissolve adhesive from the trapping chamber. The addition of a high viscosity adhesive to the trapping solution over time would similarly explain the observed decrease in Brownian motion over time. To test this hypothesis, we created an optical trapping chamber out of a rectangular silica capillary tube with a 2 mm by 0.150 mm cross section. We flowed silicon NWs into the tube and measured the diffusion coefficient of a single NW over the course of an hour. The measured nanowire temperature varied both positively and negatively through the experiment, which suggests that the adhesive may play a significant role in this effect.

While all of these explanations warrant further study, it would behoove us to have an alternative temperature sensing method.

6.3.2 Ratiometric quantum dot temperature measurements

To overcome this problem, we dispersed a solution of ZnS coated, Mn^{2+}-doped ZnCdSe quantum ratiometric QD's, a class of material whose temperature-dependent emission provides

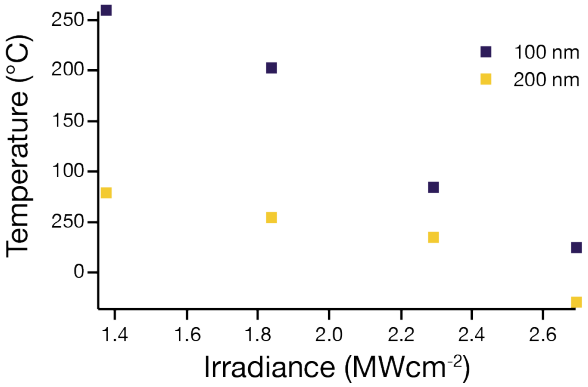

Figure 6.2: Measured temperature of trapped wires at different irradiances

an all-optical temperature measurement. During a typical thermometry event, we pump the quantum confined ZnCdSe to form an exciton, which quickly thermalizes to the Mn^{2+} $^4T_1$ state. The Mn^{2+} $^4T_1$ to $^6A_1$ transition exhibits a long, 400 μs lifetime, allowing a thermal, phonon-assisted excitation of the ZnCdSe exciton from the Mn^{2+} state, which yields up a Boltzmann distribution of states [171]. By measuring the relative population of these states via their PL, we build up an all-optical calibration of the quantum dot temperature, provided that neither state is saturated. Because this process depends on the ratio of the two states, any solvent-mediated recombination pathway applies to both the exciton and Mn^{2+} states and the ratio of the two populations remains an accurate method for thermometry [172]. In addition, by exciting the QD's via the TPA of the NIR trapping beam, the optical trap serves the dual purposes of both manipulating the silicon NW and pumping the QD's for thermometry.

The temperature- and irradiance-dependent PL from the Mn^{2+}:ZnCdSe QD's excited with 488 nm wavelength light (lambda=975/2 nm) is shown in Figure 6.3, illustrating the range of our QD thermometers from 23 °C to 150 °C. Conveniently, Mn^{2+}:ZnSe has been studied as a material for stimulated-emission depletion spectroscopy and exhibits a high TPA cross section [173]. Unfortunately, there also exists a nonradiative recombination process driven by an infrared, metal-to-ligand, ESA from the Mn^{2+} at high irradiances. By modeling

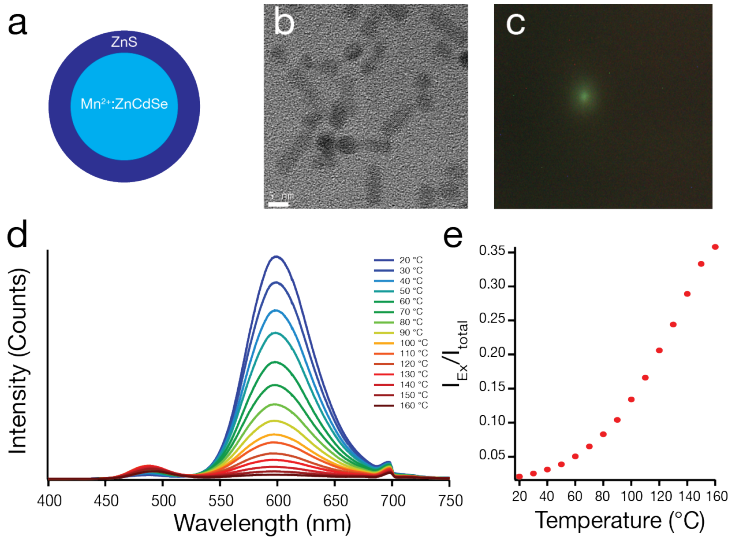

Figure 6.3: Characterization of the Mn^{2+}:ZnCdSe ratiometric QD's, including a schematic of the dots core-shell structure (a), TEM (b), and PL from TPA at 3 $MWcm^{-2}$ (c). In addition, the temperature-dependent PL (d) and ratios of integrated exciton emission (e), centered at 490 nm and total emission at each temperature

this process, we arrive at a new irradiance-dependent calibration, which uses only the ESA absorption cross section, σ_{ESA}, as a fitting parameter,

$$\frac{I_{Ex}}{I_{Mn^{2+}} + I_{Ex}} = \frac{\eta_{Ex} k_{Ex} \left(k_{up} e^{\frac{\Delta E}{kT}} + k_{Mn} + \sigma_{ESA} \Phi \right)}{\eta_{Mn} k_{down} k_{Mn} + \eta_{Ex} k_{Ex} \left(k_{up} e^{\frac{\Delta E}{kT}} + k_{Mn} + \sigma_{ESA} \Phi \right)} \tag{6.14}$$

where I_{Ex} and $I_{Mn^{2+}}$ and η_{Ex} and η_{Mn} are the emission and external quantum efficiency from the exciton and Mn^{2+}, respectively. In addition, k_{down} and k_{up} are the rate constants for energy transfer from exciton to Mn^{2+} and from the Mn^{2+} to the exciton energy levels, respectively; while, k_{Ex} and k_{Mn} are the rate constants for the sum all radiative and nonradiatve recombination processes from the exciton and Mn^{2+} levels. Finally, Φ is the excitation irradiance, which accounts for ESA. Fitting irradiance- and temperature- dependent data of a mixture of QD's and toluene shows that the potential error of this process is greatest at low temperatures and likely influences the result by approximately 10 K. However, because

the rate coefficients are available in literature, we can account for ESA [171].

To monitor temperatures, we dispersed the silicon NWs and QD's together in toluene, traped a wire far from a coverslip, and measured the ratiometric emission at different irradiances. The silicon NWs were 3 μm in length with varying diameters below 500 nm. We observed a maximum temperature greater than the boiling point of toluene (110 °C), confirming that an optically-trapped, low absorption coefficient material can superheat an organic solvent. By comparison, silicon NWs trapped in water at similar irradiances in the identical optical trap reached temperatures of 25 °C, further throwing the observed temperatures into relief. The high temperature of the control sample without a wire is likely due to ESA-induced thermalization, which heats the particles. This will be the subject of future research. In addition, these high temperatures match the qualitative observation of boiling at liquid interfaces, the formation of convection cells, and combustion at junctions with interfaces, none of which have been observed in water trapping. We also observed that the local temperature around the wire depends significantly on the NW size, with a maximum for the 200 nm diameter wire.

6.3.3 Analytical heat transfer of trapped silicon nanowires

To understand this observation, we modeled the heat distribution through the wire at steady state. First, we used a DDA implemented in DDSCAT to vary the wire diameter from 100 nm to 300 nm and solved for the internal electric field distribution. Figure 6.5 illustrates the internal electric field within a 200 nm diameter and 3000 nm length silicon NW. Because this case sits firmly within the Mie regime, internal resonances can build up, as demonstrated by the 6 points of high electric field throughout the NW. These resonances are highly sensitive to both the length and diameter of the NW. We follow the solution of Roder et al. with the addition of a temperature-dependent boundary conditions using,

$$Nu = \frac{hL}{k_m} = \frac{4}{3}\left(\frac{7RaPr}{5(20+21Pr)}\right)^{1/4} + \frac{4}{35}\frac{(272+315Pr)L}{(64+63Pr)2r} \tag{6.15}$$

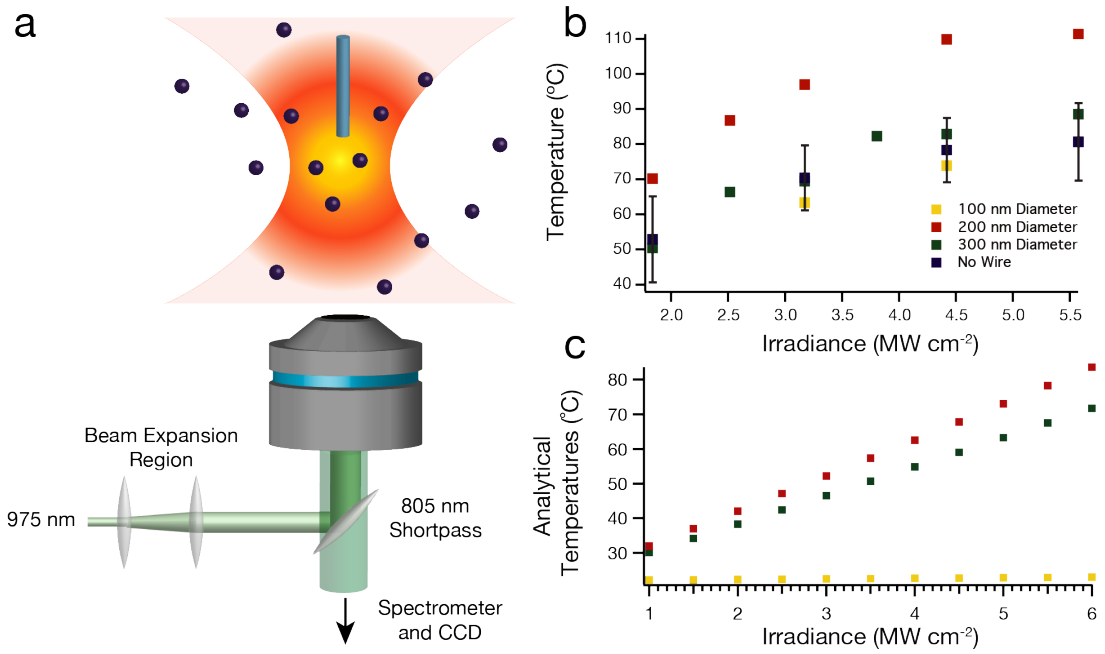

Figure 6.4: A schematic (a) of the experiment using ratiometric quantum dots suspended around an optically-trapped silicon NW, with measured (b) and predicted (c) temperatures.

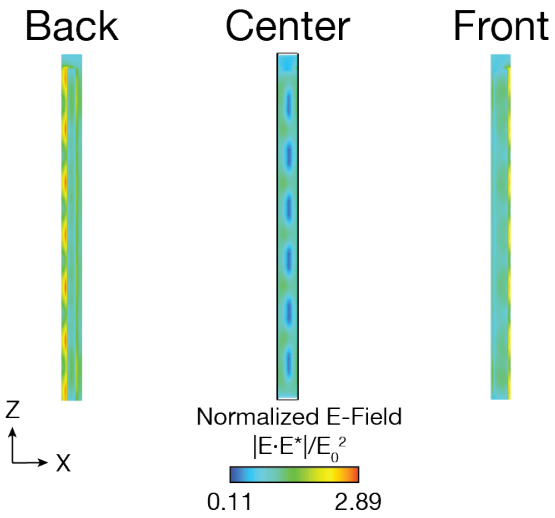

Figure 6.5: A plot of the internal electric fields within the XZ plane upon irradiation of a 200 nm diameter and 3000 nm length silicon NW. The 975 nm incident plane wave is linearly polarized and propagates in the +Z direction. The Y-axis is in the plane of the Figure.

to account for convective heat loss at the surface, which we solve by an iterative process [6, 160, 166, 174–176]. Here, h is the film heat transfer coefficient, k_m is the thermal conductivity of the medium, and the Ra, the Rayleigh number, is the product of the Grashoff, Gr,

$$Gr = \frac{(g\beta\Delta T L^3)}{\mu^2}, \tag{6.16}$$

and Prandtl, Pr, numbers,

$$Pr = \frac{\mu\rho C_p}{k}, \tag{6.17}$$

where g, β, ρ, and C_{pm} are the acceleration due to gravity, the thermal expansion coefficient, density, and heat capacity of the medium evaluated at the film temperature. ΔT is the difference in temperature between the nanowire surface and the bulk solvent temperature. L and r are the nanowire length and radius. The results of this analysis are shown in Figure 6.4c. It should be noted that this correlation for heat transfer from a vertical cylinder was not generated from data that included wires with this curvature [177]. In fact, these NWs are orders of magnitude below any previously-measured case. Regardless, the qualitative results reflect the trends we measured experimentally. For continuous irradiance with a 975 nm wavelength plane wave incident on a bottom of a vertical cylinder, we find a maximum temperature for a 200 nm diameter wire, due to a resonance-enhanced absorption, confirming the validity of the temperature measurements. While the measured temperatures monotonically increase with increasing irradiance, they uniformly plateaued between 4.5 and 5.5 MWcm^{-2}. This is likely due to an increase in the convective heat loss at high temperatures and the increased temperature sampling volume. As we increase the trap irradiance, we simultaneously heat the silicon NW and expand the volume over which we measure temperatures. To a first order approximation, the temperature decreases proportionally to 1/r away from the trapped particle [178]. Measuring the temperature farther from the wire will decrease our observed average temperature. Thus, these temperatures represent a lower bound.

These studies represent the first comprehensive foray into not only optical trapping in organic solvents, but also an understanding of laser-induced heating in organic media. Be-

yond optical trapping, we expect these results to find application in laser-based printing and patterning techniques [168, 179], studies of thermophoretic effects [180], and photochemistry [181]. As an immediate example, one of the few organic trapping studies in literature compared trapped melamine-formaldehyde beads in acetone and water to search for hydrodynamic memory in Brownian motion—that is a "colored" power spectrum. However, despite the similar thermal conductivity to toluene (0.164 for acetone), the report discounted the effects of temperature. If there were some thermophoretic-induced force on the particles, it could have produced a "colored" spectra.

6.4 Assembly of nanocrystal-nanorod heterostructures

6.4.1 Introduction

To demonstrate a potential application employing organic solvents, we the optical trapped, aligned, and assembled semimetal nanocrystal-semiconductor nanorod heterostructures in organic solvents with viscosities up to 28 times greater than water for the first time [161]. We synthesized bismuth-seeded germanium nanorods via a solution-liquid-solid synthesis, which act as nanomaterial building blocks to assemble heterostructures. Discrete dipole approximation simulations and experimental data show that the bismuth seed experiences greater radiation pressure than the germanium wire, which causes it to align away from trapping laser—that is, parallel to the Poynting vector [182, 183]. We leverage this effect to construct arbitrarily long bismuth nanocrystal-germanium nanorod heterostructures freely in solution. Coupled electromagnetic and heat transport simulations demonstrate that trapping and assembling freely in solution produces significantly higher temperatures without bubble nucleation or autoignition compared to trapping and assembling on a surface, due to the Young-Laplace pressure [6, 160]. Interestingly, for non-absorbing particles in the optical trap, heat transport analysis reveals that the lower absorption coefficient of organic media decreases the unintentional heating observed in water. For absorbing particles, heat transport analysis shows significantly increased heating. The ability to trap in oxygen- and water-free

toluene and squalane media significantly increases the library of materials available for use in optical tweezers.

6.4.2 Materials and methods

To trap, manipulate, and assemble particles, we employed a home-built optical trap, as depicted in Figure 6.6a. This consists of a diode-pumped, solid-state Yb^{3+}:YAG thin-disk laser tunable laser set to 1020 nm, a beam expansion region, and a 100x trapping oil-immersion objective (NA = 1.25), and a modified perfusion chamber with a 300 μm spacer [6, 175]. The germanium nanorods were grown via a solution-liquid-solid process from bismuth seeds.

Briefly, bismuth nanocrystals were synthesized by the generation of tris[bis(trimethylsilyl)amido] bismuth and the thermolysis of this precursor in a stabilizing solution of of 25 wt % poly(1-hexadecene-co-1-vinylpyrrolidinone) in 1-octadecene. The nanocrystal dispersion was transferred to a nitrogen atmosphere and washed with a 2:3 ratio of toluene:ethanol at 10,000 RPM three times to remove excess polymer, which is known to facilitate the development of branches during germanium nanorod growth. The cleaned bismuth nanocrystals were redispersed in anhydrous toluene and used for the solution-liquid-solid growth of bismuth-seeded germanium nanorods. Germanium nanorods were synthesized in high boiling point solvents (squalane and trioctylphosphine oxide) via solution-liquid-solid growth, using diphenylgermane (DPG) as the germanium precursor and bismuth nanocrystals to facilitate the anisotropic growth of germanium nanorods [184].

Typical Schlenk line techniques were used for the synthesis of bismuth nanocrystals and germanium nanorods. To synthesize bismuth nanocrystals, a solution of 25 wt % poly(1-hexadecene-co-1-vinylpyrrolidinone) in 1-octadecene was dried over molecular sieves for one week. In a round-bottomed flask, 71 mg of bismuth (III) chloride were combined with 0.46 mL of anhydrous THF and stirred at 950 RPM under nitrogen. After one hour of mixing, 6.1 mL of 25 wt % poly(1-hexadecene-co-1-vinylpyrrolidinone) in 1-octadecene was added and vacuum was quickly pulled on the solution before returning to nitrogen and increasing

the mixing speed to 1150 RPM. 1.2 mL of sodium bis(trimethylsilyl) amide was quickly injected into the flask under nitrogen and the reaction ran for 17 hours. The nanocrystals were immediately transferred to a nitrogen atmosphere for storage and future cleaning.

To clean the bismuth nanocrystals, 2 mL of the nanocrystal dispersion were separated and cleaned under a nitrogen atmosphere by adding 10 mL of toluene and 15 mL of ethanol, vortexing to mix the dispersion, and centrifuging the dispersion at 10000 RPM for ten minutes. The supernatant was carefully removed, and this washing procedure was repeated for a total of three times to remove excess PHD-co-PVP, which is known to facilitate the growth of branched germanium nanorod structures. Bismuth nanocrystals were redispersed in 2 mL of toluene for future use to grow anisotropic germanium nanostructures.

A modified synthesis from Chockla et al. was implemented to synthesize germanium nanowires [184]. Briefly, 2 grams of trioctylphosphine oxide (TOPO) and 4 mL of squalane were combined in a round-bottom flask at 900 RPM and degassed at 150 °C for an hour and a half. 200 μL of cleaned bismuth nanocrystals in 400 μL was added to the flask and low boiling point solvents were removed by quickly pulling vacuum. The solution was heated to 350 °C and a solution of 50 μL diphenylgermane in 500 μL squalane was rapidly injected. The reaction ran for ten minutes, was cooled 100 °C, quenched with 10 mL of anhydrous toluene, and then transferred to a nitrogen atmosphere. A fraction of the nanorod dispersion was removed from the glove box and cleaned with a ratio of 2:3 toluene:ethanol and centrifuged at 8000 RPM for 10 minutes for a total of five washes. The resulting bismuth-seeded germanium nanorods were redispersed in toluene.

To prevent oxide formation, we loaded and sealed the perfusion chamber in a nitrogen atmosphere. TEM and Raman measurements (Figures 6.6b and 6.6c) confirm that the synthesis yielded crystalline germanium nanorods with monodisperse diameters defined by the diameter of the bismuth seed and lengths between 100 and 5000 nm, depending on the synthesis parameters. In addition, TEM images illustrate the presence of the bismuth tips on the germanium nanorods after growth. We will refer to these bismuth-tipped germanium nanorods as "nanorod," hereafter. As recently discussed by Black and coworkers [161], the

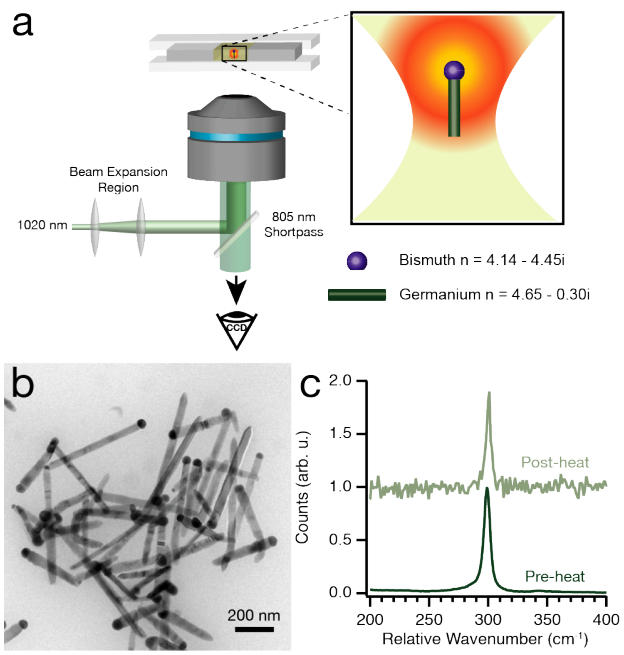

Figure 6.6: A schematic of the optical trapping experiment (a), TEM image of the nanorod, illustrating their average diameter and composition (b), and Raman scattering before and after laser heating the solution (c).

solubility of nanoparticle's in organic solvents enables more facile optical trapping.

6.5 Results and discussion

6.5.1 Optical trapping in high viscosity solvents

To demonstrate the range of solvents available for optical trapping, we varied the ratio of toluene to squalane and observed stable nanorod trapping across the entire range of media composition. This significantly expands the currently reported range of liquid viscosities (Prandlt number) from 1 cP (7.1) up to 28.4 cP (317) [185, 186]. While we were able to trap individual nanorods from 1.0 to 10 W, limited on both sides by the available power of the trapping beam, longer nanorods (1μm) were easier to trap.

The observation that longer nanorods trap more easily is likely due to the different forces on the bismuth and germanium portions particle. Because the nanorods in these experiments

are anisotropic, the optical trapping force and scattering force acted differently on the germanium nanorod and bismuth nanocrystal. To estimate these forces, we modeled a bismuth sphere and a germanium nanorod with the discrete dipole approximation in DDSCAT (Figure 6.7) [183]. For bismuth spheres and germanium cylinders with equivalent diameters, this analysis revealed that the force of radiation pressure on the bismuth nanocrystal is 4-9 time greater than the radiation pressure on the germanium nanorod. These forces represent a lower bound on the radiation pressure as the diameter of the bismuth seed is typically greater than the germanium nanorod. Examining the refractive index of bismuth ($n_{Bi} = 4.14 - 4.45i$) and germanium ($n_{Ge} = 4.65 - 0.30i$) at 1020 nm, it is intuitive that the greater absorption of the bismuth accounts for the increased radiation pressure [187, 188]. Far from the high electric field gradient in the optical trap focal plane, this pressure force dominates, which causes the bismuth particle to align vertically in the trap [167]. Given the density of free carriers in metals employed as seeds the growth of semiconductor nanorods, these simulations suggest that anisotropic radiation pressure is likely a general alignment method of alignment for solution-liquid-solid , supercritical fluid-liquid-solid, and vapor-liquid-solid nanorods [189]. In addition, as was noted during the optical trapping of similarly high-refractive index InP nanorods, the gradient force was independent of the nanorod length because the nanorod length extended far beyond the focal depth of the optical trap [163, 190]. This suggests that, while the bismuth tip experiences significant scattering forces that cause it to align in the direction of the Poynting vector, the germanium nanorod ultimately enables optical trapping force, which is relatively independent of the bismuth. This could explain the ease of trapping longer nanorods.

6.5.2 Alignment and assembly of bismuth nanocrystal-germanium nanorod heterostructures

To demonstrate the application of this alignment force in organic solvents, we used the optical trap to assemble bismuth nanocrystal-germanium nanorod heterostructures freely in a squalane solution [191–194]. We accomplished this by first trapping a nanorod and then positioning the particle above another nanorod in Brownian motion (Figure 6.8) Radiation

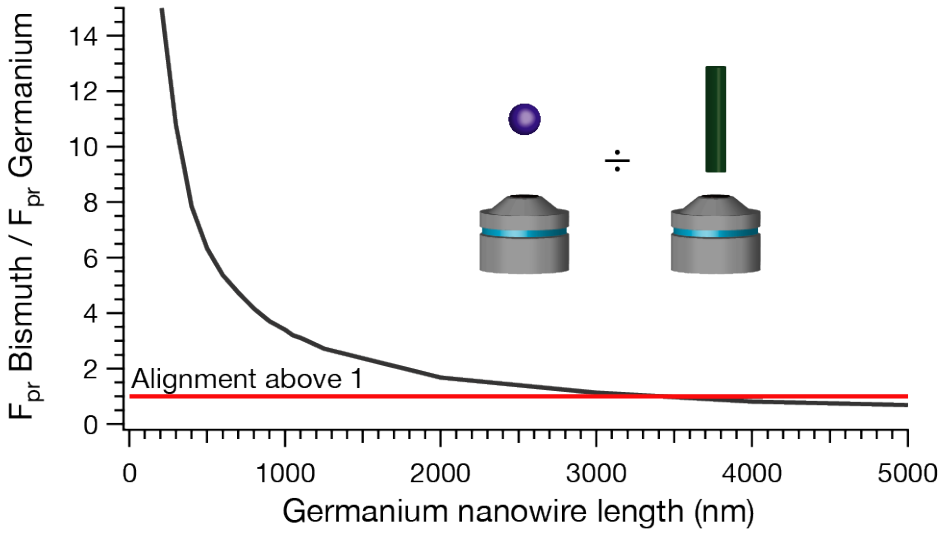

Figure 6.7: The ratio of the radiation pressure force on the bismuth to the radiation pressure force on the germanium nanorod. The calculations were performed for a bismuth nanocrystal with a diameter of 64 nm and a germanium nanorod with a diameter of 32 nm and varying length. nanorods with dimensions above the red line will align with the bismuth vertically in the trap.

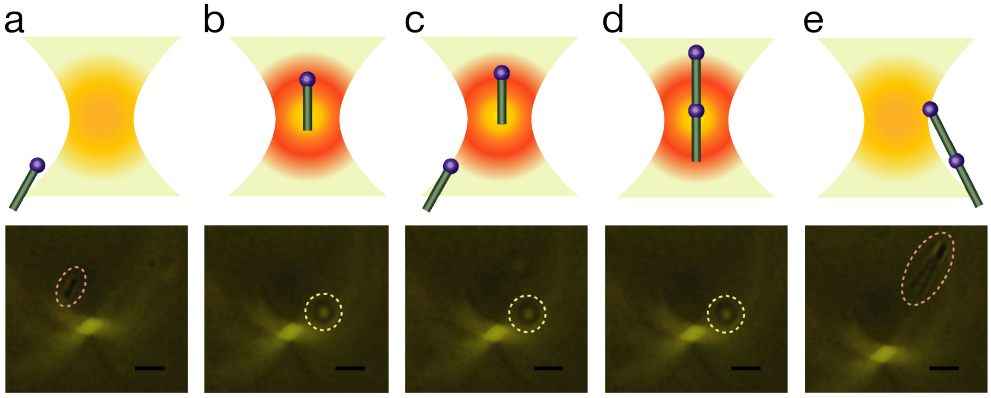

Figure 6.8: Demonstration of nanorod assembly and soldering. First, radiation pressure pushes (a) a single nanorod into the trap (b). We then manipulate the trapped nanorod above a second nanorod diffusing freely in Brownian motion (c). Radiation pressure and laser heating forms a heterostructure (d), and subsequently released back into solution (e)

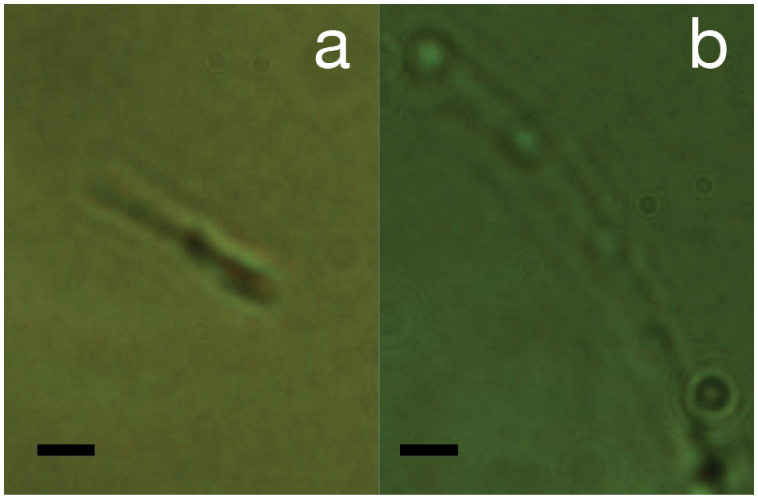

Figure 6.9: Laser-heating of optically trapped nanorods with (b) and without (a) DPG.

pressure accelerated the untrapped nanorod toward the trapped particle. When the accelerated nanorod reached the optical trap, it "soldered" onto the existing nanorod, as shown in Figure 6.8. We could repeat this process to add more nanorod building blocks ad nauseum. Because radiation pressure aligns the bismuth away from the laser, this process creates a repeating bismuth nanocrystal-germanium nanorod heterostructure. We added diphenylgermane to the trapping chamber to illustrate the formation of the heterostructure [184, 189]. As the bismuth heats, the diphenylgermane decomposes and allows for germanium incorporation to form a bismuth-germanium alloy, visible at the interface between germanium nanorods in Figure 6.9. nanorod heterostructure assembly was only possible in squalane at a minimum power of 6 W. In attempts to trap and assemble nanorods dispersed in toluene, radiation pressure drove nanorod into the trap at much higher velocities, which prevented vertical nanorod alignment prior to nanosoldering. The addition of an angled nanorod yielded radially-anisotropic structures that began to spin and ultimately flew out of the trap. While impractical for the continued production of heterostructures, this does illustrate the efficacy of this nanosoldering process to create more complicated structures [195]. Given the low Reynold's number, nanorods enter the trap at terminal velocity, defined by the viscosity of

the solvent and the laser power [167]. The massive disparity between the viscosity of squalane (28.4 cP) and toluene (0.58 cP) illustrates that nanorods approaching the trap will travel at much greater speeds in toluene than squalane. The high power requirement for assembly in squalane could be due to either minimum radiation pressure forces to align the nanorod prior to entering the trap or the increased heating to produce convective forces, which align the nanorod.

6.5.3 Laser heating during trapping in organic media

When trapping in an aqueous chamber with a NIR laser, water's relatively high absorption coefficient can result in appreciable heating of the solvent environment, which has been observed to influence experiments [159, 160]. This has led to trapping in D_2O, due to its low NIR absorption coefficient [6]. A number of independent groups have studied the effect of NIR absorption on the solvent, which suggests heating on the order of 1-10 KW^{-1}. On the other hand, organic solvents often exhibit significantly lower NIR absorption coefficients and thermal conductivities [196]. For an empty trap, the dominant heat loss mechanism is thermal conduction. We estimate that the solvent-induced heating in toluene (α=3.5 m^{-1}, k=0.14 $Wm^{-1}K^{-1}$) is 1.7 $Wm^{-1}K^{-1}$ [159]. A similar analysis for water (α=29 m^{-1}, k=0.60) yields 3.6 $Wm^{-1}K^{-1}$. This suggests that, for an empty trap, the solvent induced heading is similar for water and organic solvents.

However, when the optical trap contains a highly absorbing particle, the lower thermal conductivity of organic solvents (0.1 $Wm^{-1}K^{-1}$) will likely produce significantly greater temperatures in water. As an estimate of the temperatures of the trapped germanium nanorods, we again use the modified theory as discussed in section 6.3.3. To create a lower bound of temperatures, we first a performed heat transport analysis on a germanium nanorod with a diameter of 32 nm and a length of 1 μm without including absorption from the bismuth tip Figure 6.10. The 1 μm nanorods exhibited an average temperatures of 478 °C in an ambient bath of squalane at a power of 6 W, which was used for assembly (Figure 6.10). The temperature profile closely mirrors the source, which is greatest at both ends of the

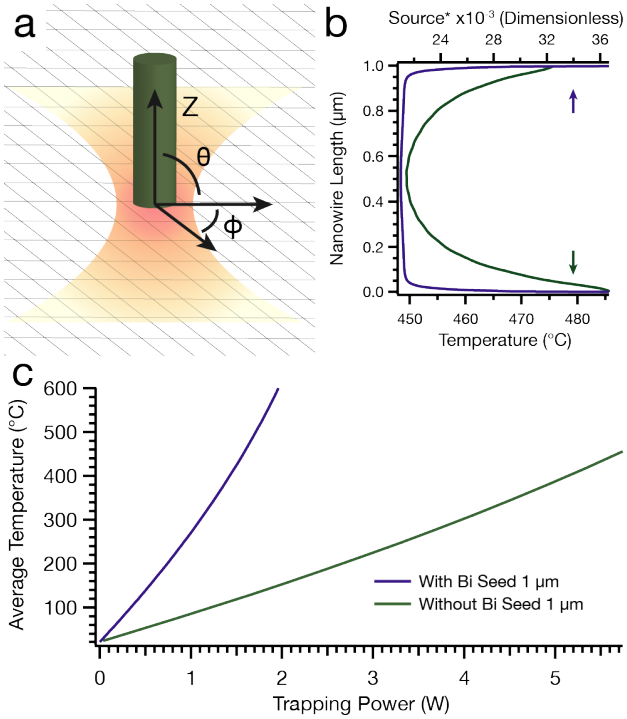

Figure 6.10: Analytical heat transport calculations for the trapped germanium nanorods, using the modified solution of [6]. Panel a illustrates the coordinate system for the calculation. We show the temperature and source profiles of an individual germanium nanorod without a bismuth tip trapped at a power of 6 W (b). The average power-dependent temperature of the germanium nanorod are plotted in panel c. Using the heat balance, we approximate the power-dependent temperature of the combined bismuth and germanium nanorod (c). Panel c shows the average temperature of the germanium nanorod with varying irradiance with and without a bismuth nanocrystal tip.

nanorod and varies only slightly (<10%) along the length of the nanorod, shown in Figure 6.10b. In addition, the temperatures increasing significantly with irradiance Figure 6.6c.

We note that, during the nanosoldering process, the optical trap pushes a single nanorod through the focal plane before the nanorod joined to form a heterostructure. This means that the Rayleigh regime of the Gaussian beam heats the bismuth tip at the maximum irradiance immediately prior to nanosoldering. The time scale to achieve steady state heating is much less than the time for the nanorod to reach the trapped particle, meaning that the particle is constantly at steady state as it approaches the trapped particle.

The Biot number measures the the ratio of heat flux within a structure to the rate of heat flux away from a structure. When the Biot number is much less than 1, the temperature distribution within a material is uniform; when the Biot number is much greater than 1, the temperature distribution within a material is non-uniform. Both the germanium nanorod and the bismuth nanocrystal have Biot numbers far below 1, and the temperature within the nanorod is likely uniform, as suggested by Figure 6.10 b. Further, the uniform temperatures imply that the a heat balance on the nanorod, including the germanium and bismuth, will yield a reasonable approximation of the temperature. We use a heat balance coupled with the iterative convective solution as detailed in the supporting information to obtain an estimate of the bismuth tipped germanium nanorod (Figure 6.10 c). This suggests that the bismuth tip is likely liquid during the nanosoldering process. In addition, the trapped particle will have locally heated the solvent, increasing the ambient medium temperature, which is not considered in this approximation. Temperature measurements of the trapped nanoparticles are under investigation and will be the topic of a future manuscript

6.6 Conclusion

We have expanded the range of optical trapping media from dynamic viscosities and Prandlt numbers from 1 cP and 7, respectively, up to 28.4 cP and 317 for a chamber of pure squalane, and trapped germanium nanorods for the first time. DDA and experimental results show that the bismuth seed particle used to facilitate the growth of germanium nanorods experiences a significantly greater radiation pressure than germanium portion of the nanorod, which causes the bismuth nanocrystal to consistently orient vertically in the trap. In addition operating an optical trap in organic solvents, compared to aqueous solvents, slightly decreases solvent heating effects due to the decreased absorption coefficient, but generates wildly increased temperatures due to the decreased thermal conductivity. We leveraged these effects to produce bismuth nanocrystal-germanium nanorod heterostructures freely in squalane solutions. We anticipate that the bottom-up assembly of well-defined, solution-grown nanostructures will broadly enable technologies that require well-defined heterostructures. Furthermore, we

anticipate that these results will usher in a new realm of optical trapping applications, including nanomanufacturing from nanomaterial building blocks [191], single-particle catalysis [161, 164], and hydrodynamic studies [156, 157].

Chapter 7

RAPID SYNTHESIS OF TRANSITION METAL DICHALCOGENIDE–CARBON AEROGEL COMPOSITES FOR SUPERCAPACITORS

7.1 Introduction to supercapacitors

In response to rapid improvements in renewable energy generation, electrochemical supercapacitors with high power densities and rapid cycling have emerged as a promising technology to bridge the energy density storage and variable energy density demands of grid management and hybrid vehicles[1] [197]. State of the art batteries employ lithium intercalation that enables 3 to 30 times more charge storage than supercapacitors. However, supercapacitors can provide 2 to 3 orders of magnitude greater power [198]. While typical lithium-ion batteries store electrochemical potential via phase transformative redox reactions, supercapacitors do so by means of an electrical double layer in a working electrolyte and/or rapid charge transfer processes with no concomitant phase transition, that occurs in response to an applied voltage [127, 198–200]. Thus, supercapacitors do not face the performance-limiting factors of reaction kinetics, ion transport through bulk electrode material, and accompanying volume changes that are characteristic of batteries. Improvements in efficient, scalable, and economical syntheses are needed to drive supercapacitor applications.

Because double-layer formation dictates power densities, nanostructured materials, such as pyrolyzed carbon aerogels [201–204], with high specific surface areas (SSA) have emerged as the premier supercapacitors [205]. Carbon aerogels are amorphous, sp^2- and sp^3-bonded

[1]This chapter is based on "Rapid synthesis of transition metal dichalcogenide doped carbon aerogels for supercapacitor applications," which is published in *Nature Microsystems and Nanoengineering*, **3**, 17032 (2017) by Matthew J. Crane, Matthew B. Lim, Xuezhe Zhou, and Peter J. Pauzauskie. It was rapidly co-written with Matthew B. Lim.

carbon structures formed from the reaction of resorcinol and formaldehyde with high SSA's (>500 m^2 g^{-1}), narrow pore sizes, and low densities [73, 206–208]. Upon pyrolysis, these aerogels exhibit improved electrical conductivity (up to 50 S cm^{-1}) and SSA with benign chemistry, making them an intriguing material for supercapacitors [207, 209]. To improve their performance, research groups have attempted to load them with high-conductivity or high-capacitance materials [210, 211]. However, their lengthy synthesis time (typically 24 hours or longer) prevents economical scalability, limiting their widespread use [203, 208]. Transition metal dichalcogenides (TMD's) are layered, graphite-like van der Waals structures composed of a transition metal layer sandwiched between two chalcogenide layers that have shown promise as supercapacitor active materials due to the range of oxidation states available to transition metals [127, 212–214]. A recent report demonstrated that Mo_2 capacitance significantly improves after conversion from the semiconducting 2H phase to the 1T, metallic 1T phase, due to enhanced electrical conductivity—the in-plane conductivity of 2H MoS_2 is ~0.2 S cm^{-1} and that of the 1T phase is 10–100 S cm^{-1}—and increased ion intercalation mobility [212, 215, 216]. Similarly, 2H MoS_2 and WS_2-based supercapacitor performance improved after creation of mesoporous structure with enhanced conductivity [217, 218]. However, it is important to note that the most successful 1T devices suffered from a low SSA of 9 m^2 g^{-1}, and required the use of pyrophoric n-butyllithium to induce a phase change, both of which mitigate the scalability of its impressive performance. In addition, freestanding TMD films do not exhibit mechanical stability in electrochemical environments, which sets a limit to the maximum size of unsupported films and inhibits high surface area applications [219]. To address the aforementioned limitations, we present in this work a synthesis that emphasizes scalable processes to encapsulate exfoliated TMD sheets in an aerogel matrix via benign and ultrafast resorcinol–formaldehyde (RF) sol–gel chemistry [73, 203, 206, 211]. This process employs the ultrasonication of TMD precursors—MoS_2 and WS_2—in acetonitrile to produce 2H MoS_2 and WS_2, respectively, followed by the rapid, acid-catalyzed gelation of RF within 30 minutes at mild temperatures. After supercritical drying and high temperature pyrolysis, the resulting carbon aerogel provides a high surface

area, mechanically stable, and electrically conductive support for TMDs that is well suited for electrochemical devices. To demonstrate these applications, we perform supercapacitor tests on our TMD-loaded carbon aerogels that yield favorable specific capacitances around 80 F g^{-1}, volumetric capacitances approaching 60 F cm^{-1}, and low operational electrochemical impedance.

7.2 Materials and Methods

7.2.1 Transition metal dichalcogenide–carbon aerogel composite synthesis

When exfoliated TMD sheets dry, they restack to form low surface area (9 m^2 g^{-1}) films [212, 220]. As such, we designed the rapid synthesis to avoid allowing the TMD solution to dry before the gelation can trap any exfoliated sheets. Additionally, while we employ sonication [221, 222] to disperse the TMD's, there are a range of other potentially scalable exfoliation methods including shear mixing [223], direct synthesis [224], and intercalation [225, 226] to name a few. Figure 7.1 outlines the TMD aerogel synthetic scheme. In the first step, a temperature-controlled bath sonicator (22°C; Branson 1510R-DTH, Danbury CT, USA) exfoliates and disperses TMD sheets in acetonitrile (ACN, EMD Millipore, Billerica MA, USA) at concentrations from 8.6 to 34 mg/mL. However, we were able to synthesize aerogels at TMD loadings of up to 100 mg/mL in acetonitrile. After sonication for 60 minutes, we transferred this solution to a polypropylene tube and added resorcinol (R, Sigma-Aldrich, St. Louis MO, USA), formaldehyde (F, 37 wt-% methanol-stabilized aqueous solution, Sigma-Aldrich), and hydrochloric acid (C, 37 wt-%, Macron, Center Valley PA, USA) to achieve molar ratios of R:F = 1:2, R:C = 8.4:1, and R:ACN = 1:76 [203, 208], which result in a 2:1 ratio by weight of resorcinol to TMD for a 17.1 mg/mL starting dispersion of TMD. This corresponds to molar ratios for resorcinol to MoS_2 (powder, Sigma Aldrich) and WS_2 (powder, Alfa Aesar, Haverhill MA, USA) of 2.9:1 and 4.5:1 respectively. For WS_2-loaded gels, we prepared additional samples by the same technique using initial WS_2 dispersions of 8.6 mg/mL and 34 mg/mL, which corresponds respectively to 4:1 and 1:1 weight ratios, or

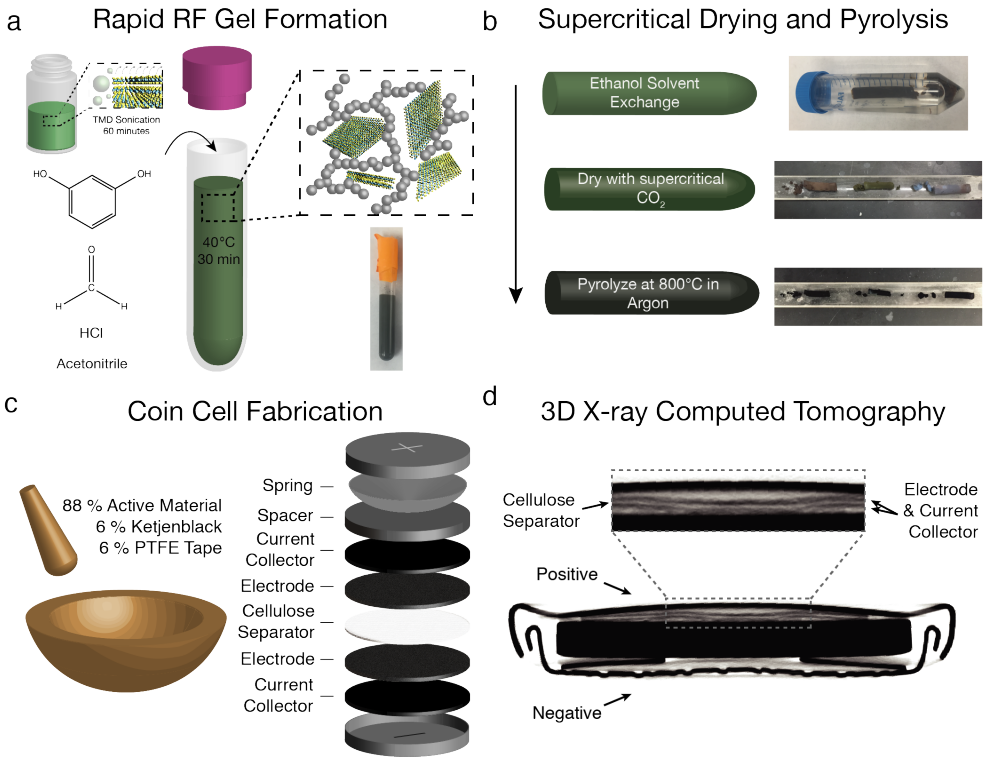

Figure 7.1: Outline of the nanomanufacturing process for composite TMD carbon aerogels. Initially, sonication driven cavitation (a) drives TMD sheets apart and enhances dispersion within acetonitrile. Resorcinol and formaldehyde are added to this solution, which causes rapid sol-gel formation, catalyzed by hydrochloric acid. This gel is washed with ethanol to remove any unreacted species and dried with supercritical CO_2 (b) to displace the solvent without destroying pore structure before being pyrolyzed in argon. Finally, we process this material into a supercapacitor by grinding it with carbon black additive (Ketjenblack) and PTFE tape, rolling and punching it into electrodes that are assembled into a symmetric coin cell, and adding the resulting electrode to a full coin cell, using a cellulose separator, illustrated in (c). A three-dimensional X-ray computed tomography image of a coin cell after 10,000 charge-discharge cycles (d)

9.0:1 and 2.25:1 molar ratios, of resorcinol to WS_2. We also prepared a control sample with no TMD. The mixture of reagents was quickly placed in the bath sonicator set to 40°C for 30 minutes. During this time, the resorcinol undergoes electrophilic aromatic substitution at the 2, 4, and 6 positions with formaldehyde to form methylene and methylene ether bridges [73]. We then washed the aerogel with ethanol three times over 36 hours to remove the acetonitrile and dried it with supercritical CO_2 in an autoclave (E3100, Quorum Technologies, Laughton, East Sussex, UK). Because it has low density and surface tension, supercritical CO2 displaces the ethanol and preserves pore structure to produce a high surface area product. Finally, we pyrolyzed the aerogels in a tube furnace at 800°C in an argon atmosphere for 4 hours, which drives off oxygen moieties, yielding a high conductivity sp^2-and sp^3-bonded support of carbon spheres. We found that annealing at 1000°C destroyed the TMD's. In addition, we note that this pyrolysis step mimics the current industrial synthesis of supercapacitors [227]. Before pyrolysis, the MoS_2 and WS_2 loaded aerogels exhibit a dull, deep blue and green color, respectively, whereas the pure RF aerogel has a brick-red color. Following pyrolysis, the aerogels all exhibit a dark black color, indicative of carbonization (Figure 7.1b) [211]. Henceforth, the pyrolyzed pure RF aerogel will be abbreviated RFA, the pyrolyzed MoS_2-loaded aerogel will be abbreviated MA-17, and the pyrolyzed WS_2-loaded aerogel will be abbreviated WA-8.6, WA-17, or WA-34 according to the concentration of the initial TMD dispersion. Compared with the chemical exfoliation of TMD's via pyrophoric n-butyllithium [212] and the long gelation times in other syntheses [203, 208], our sol-gel synthesis represents a rapid, mild, and benign process.

7.2.2 Transition metal dichalcogenide–carbon aerogel composite characterization

To characterize the aerogels, we employed nitrogen adsorption, XRD, Raman spectroscopy, FTIR , and TEM. We collected nitrogen sorption isotherms using a NOVA 2200e porosimeter (Quantachrome, Boynton Beach FL, USA), heating samples in vacuum at 200°C for at least 12 h prior to analysis to drive off pre-adsorbed species. From the isotherms, we obtained surface area and pore size distributions with Brunauer-Emmett-Teller (BET) theory

and Barrett-Joyner-Halenda (BJH) theory respectively. Specifically, multipoint surface area calculations used data from the relative pressure (P/P_0) range between 0.05 to 0.30, and the pore size distributions used the desorption isotherm. We performed Raman spectra using a home built setup comprised of a 532 nm laser (Coherent Compass, Santa Clara CA, USA) focused with a 50x objective (0.55 NA, Mitutoyo, Kawasaki, Kanagawa, Japan) and collected on a spectrometer fitted with a liquid nitrogen-cooled CCD detector (SpectraPro 500i, Acton Research Corporation, Acton MA, USA). To collect XRD data, we used a Bruker (Billerica MA, USA) D8 Discover X-ray diffractometer equipped with a General Area Detector Diffraction System (GADDS) and a Cu K_α source at 1.54 Å. FTIR measurements were performed by the KBr pellet method with a Bruker VERTEX 70 spectrometer in transmission mode. Finally, bright-field TEM images with accompanying SAED patterns and EDS were obtained on an FEI (Hillsboro OR, USA) Tecnai G2 F20 with 200 kV accelerating voltage. In addition to MoS_2 and WS_2, we attempted to synthesize a selenium-based TMD aerogel composite, by adding $NbSe_2$. However, after pyrolysis, both Raman and XRD demonstrated that the $NbSe_2$ had oxidized into Nb_2O_5 and NbO_2. To fabricate coin cell electrodes, we ground a mixture of pyrolyzed TMD-loaded aerogels in a rotary mill (Fritsch Pulverisette, Idar-Oberstein, Germany) and passed it through a #140 test sieve (opening size ~106 μ m). We ground the milled, sieved product (88 wt%) with PTFE tape (6 wt%) as a binder, and Ketjenblack carbon additive (6 wt%, AkzoNobel, Arnhem, Netherlands) together with a mortar and pestle until the mixture was completely amalgamated. We then flattened the amalgam with a glass rolling pin to ~100 μ m thick sheet, from which we punched 0.5 inch diameter electrodes. We assembled supercapacitor devices in a symmetric two-electrode configuration consisting of a sandwich of SUPER-P carbon black (Timcal, Bironico, Switzerland) aluminum foil current collectors, CR2032 coin cell casings (MTI, Richmond CA, USA) and TMD-loaded aerogel electrodes surrounding a cellulose separator, filled with 1 M Na_2SO_4 aqueous electrolyte (Figure 7.1c). The electrochemical performance of our supercapacitor cells was evaluated using a Bio-Logic (Seyssinet-Pariset, France) VMP3 potentiostat / galvanostat with EC-Lab software. We first conditioned the cells over 5 galvanostatic charge-discharge cycles between 0.1

and 0.9 V, one cycle at 1 mA and four at 10 mA, to ensure complete electrolyte permeation. This was followed by six more galvanostatic cycles between 0.1 and 0.9 V, which were used for capacitance measurements. In these cycles, the cell was charged at 10 mA and discharged at increasing gravimetric current densities of 0.054, 0.28, 0.56, 1.39, 2.78, and 5.53 A g^{-1} for MA-17; and 0.059, 0.30, 0.60, 1.51, 3.02, and 6.03 A g^{-1} for all WS_2 aerogels as well as the RFA (normalized to the mass of active material). For the samples made from 17 mg mL^{-1} TMD dispersions, this corresponds to currents of 1, 5, 10, 25, 50, and 100 mA. Immediately after rate testing, we conducted electrochemical impedance spectroscopy (EIS) at 0.5 V with a 5 mV sinusoidal oscillation between 400 kHz and 10 mHz. Finally, we analyzed the coin cells with cyclic voltammetry (CV), sweeping between 0 and 0.9 V at 20 mV s^{-1}. For WA-17, a galvanostatic cycling test was performed following cyclic voltammetry, whereby the cell underwent continuous charge-discharge cycles between 0.1 and 0.9 V at a fixed current density of 0.25 A g^{-1}.

7.3 Results and Discussion

7.3.1 Results

TEM images of the pyrolyzed aerogels in Figure 7.2 confirmed that the RF matrix, which consisted of nanoscale carbon particles characteristic of a pyrolyzed aerogel, acted as a support for the TMD sheets. Electron diffraction (Figure 7.2a and 7.2b, inset) and energy dispersive X-ray spectroscopy (Figs. S9 and S10) of the doped aerogels demonstrate that the sol-gel process does not chemically modify the TMD's. After incorporation, these TMD crystals range in size from 5–100 nm in the (002) stacking plane and up to micron scale in length. While it does not have a high exfoliation efficiency, acetonitrile is effective at preserving large area sheet sizes by physisorbing to the chalcogenide atoms in TMDs to reduce van der Waals forces before subsequent intercalation [228]. This mild reduction is believed to prevent scissoring of TMDs and lead to large area sheet dispersion (Figure 7.2b and 7.2d) [229]. The WS_2 composite exhibited the highest degree of exfoliation, as evidenced by ad-

ditional TEM images. BET analysis of the aerogels (Figure 7.3 Table 7.1) demonstrated that the neither the addition of TMD sheets in this accelerated synthesis, nor the amount of TMD added significantly impacted the surface area or the morphology of the gel. All the TMD-loaded aerogels maintained high surface areas greater than 400 m2 g^{-1}, with a maximum for WA-17 at 620 m^2 g^{-1}. Furthermore, processing the aerogels for supercapacitor electrodes did not significantly affect their surface area: WA-17 retained 94% of its original surface area after milling and sieving, and electrode sheets made from combining the same milled and sieved sample with PTFE tape and carbon black retained 99% of the original surface area of the aerogel. These results suggest that the aerogel represents a mechanically stable support throughout processing. Comparing the theoretical maximum surface areas for the TMD's (750 and 483 m2 g^{-1}, see SI Section 1) to our control aerogel of pure pyrolyzed RF (776 m^2 g^{-1}), it is clear that the carbon aerogel constituted the majority of the surface area [203]. In addition, the nitrogen sorption isotherms of all the aerogels, including the unloaded control sample, exhibited type H1 hysteresis [230], which is characteristic of largely uniform diameter spherical particles. This further confirms that the carbonaceous matrix constituted the bulk of the surface area in the TMD-loaded samples. Indeed, the TEM images in Figure 7.2 show that the TMD's incorporated as large sheets of material supported by the homogeneous network of carbonized RF polymer. The BJH pore size distributions of the TMD-loaded aerogels were roughly unimodal and peaked below 100 Åpore radius, revealing their mesoporous nature. In contrast, the RFA featured a bimodal pore distribution with larger pores on average than the other samples, as evidenced by the peaks at 90 and 135 Å, and a tail extending past 250 Å.

In FTIR spectra of MA-17 and WA-17 (Figure 7.3c), the absence of epoxy functional groups at 1220 cm^{-1} and alkoxy groups at 1095 cm^{-1}, which form during polycondensation of resorcinol and formaldehyde, shows that pyrolysis successfully removed these oxygen-containing moieties [231]. The broad band centered at 1510 cm^{-1} along with the weaker band at 1630 cm^{-1} correspond to C=C–C stretching in an aromatic ring and is evidence of carbonized sp2-bonded structures in the aerogels. The band at 1340 cm^{-1} represents

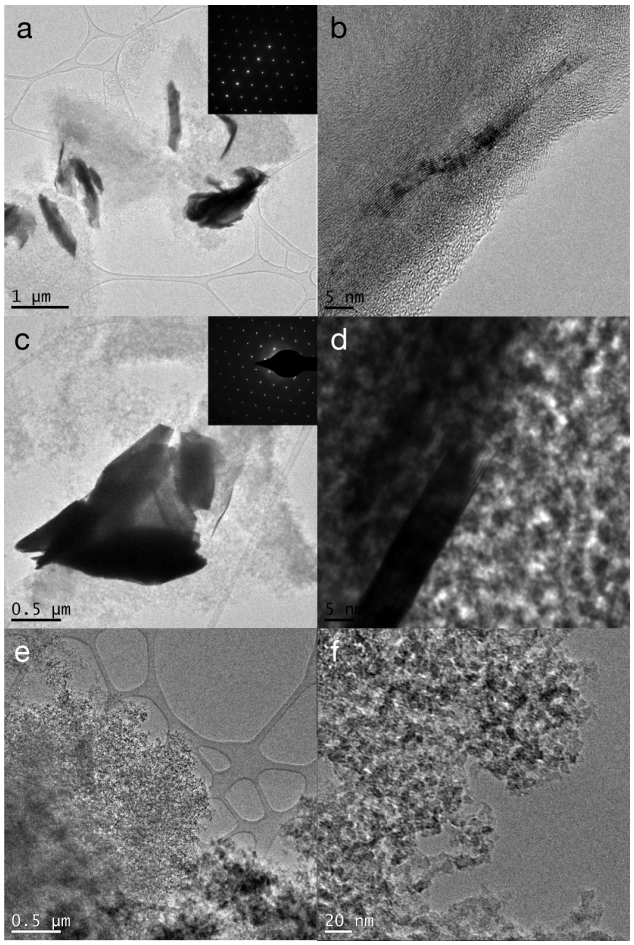

Figure 7.2: TEM images of MA-17 (a, b), WA-17 (c, d), and RFA (e, f). Panels e and f are characteristic of the gels as synthesized, while panels a, b, c, and d demonstrate the presence of exfoliated sheets. Insets in the TEM images (a and c) show electron diffraction of the TMD sheets dispersed in the aerogel.

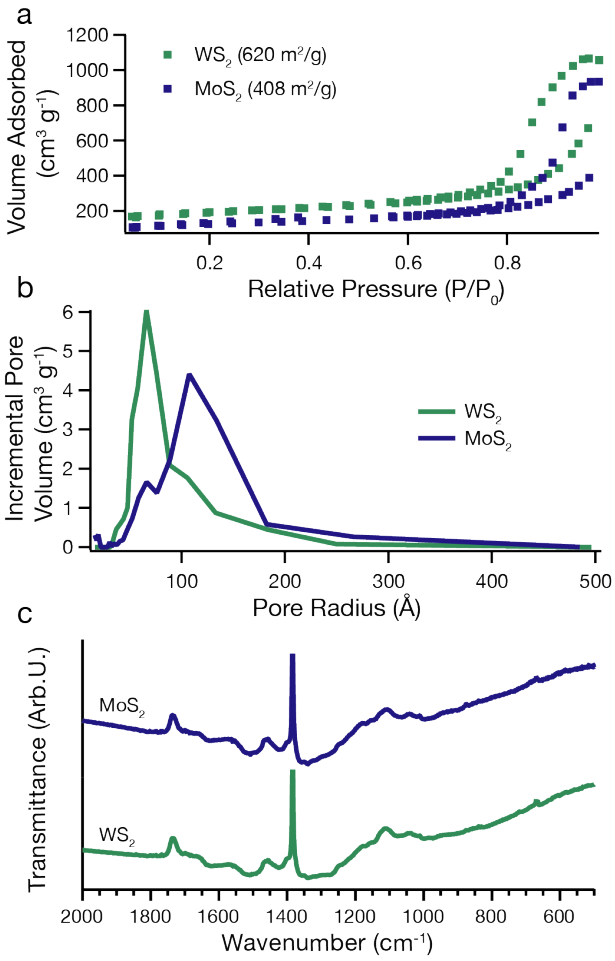

Figure 7.3: Nitrogen sorption isotherms with BET surface area (a) and BJH pore size distribution (b) of MA-17 and WA-17. In addition, FTIR transmittance data (c) demonstrate functional groups within the aerogel composites.

O–H bending in phenol groups, which have been observed to survive heat treatment even at 1000°C, well above the pyrolysis temperature of 800°C for our aerogels [232]. Notably, both aerogels exhibit a small peak at 680 cm^{-1}, corresponding to a C–S mode, which suggests that the rapid synthesis and subsequent pyrolysis produces chemical bonding between the RF matrix and the TMD sheets.

The Raman spectrum of WA-17 shows both the D band at 1345 cm^{-1} and the G band at 1603 cm^{-1} (Figure 7.4c). The D band stems from carbon-carbon sp^3 stretching with A_{1g} symmetry, associated with disordered atoms, while the G band originates from the doubly degenerate (iTO and LO phonon modes) carbon stretching with E_{2g} symmetry. Interestingly, the intensity ratio of these modes and the location of the G band provide information about both the amount of sp^3 bonding and the graphitic grain size domain. As the G band decreases in wavenumber and the intensity ratio of the D band to G band decreases, carbon bonding shifts from graphite to nanocrystalline graphite to amorphous carbon [233]. This analysis suggests that these aerogels contain approximately 5% sp^3 bonding with graphitic grain sizes of 11 nm. Prior reports have shown that the addition of transition metal ions into a carbon aerogel can catalyze graphitization during pyrolysis at temperatures greater than 1000°C [234]. However, we do not observe any catalytic graphitization of the aerogel from Raman spectroscopy. All the TMD's exhibit E^1_{2g} and A_{1g} symmetry Raman active modes, which correspond to in-plane and out-of-plane stretching modes, respectively [235]. Similar to carbon, the distance and intensity ratio between these scattering modes gives information about the degree of electrical coupling between layers. The addition of more monolayers tends to increase the energy of the out-of-plane A_{1g} mode. While the TEM data do not suggest high exfoliation of the TMD's in the gels, the shift between peaks implies that there is a decrease in interlayer coupling, which could lead to increased adsorption or intercalation of ions during supercapacitor operation. For WS_2, the spacing between the E^1_{2g} and A_{1g} peaks decreases from 69 cm^{-1} to 64 cm^{-1} after sonication, which implies that monolayers are electrically coupled to two nearby sheets (Figure 7.4b) [235, 236]. We note that this does not necessarily mean that the sheets were highly exfoliated, only that inter-layer coupling

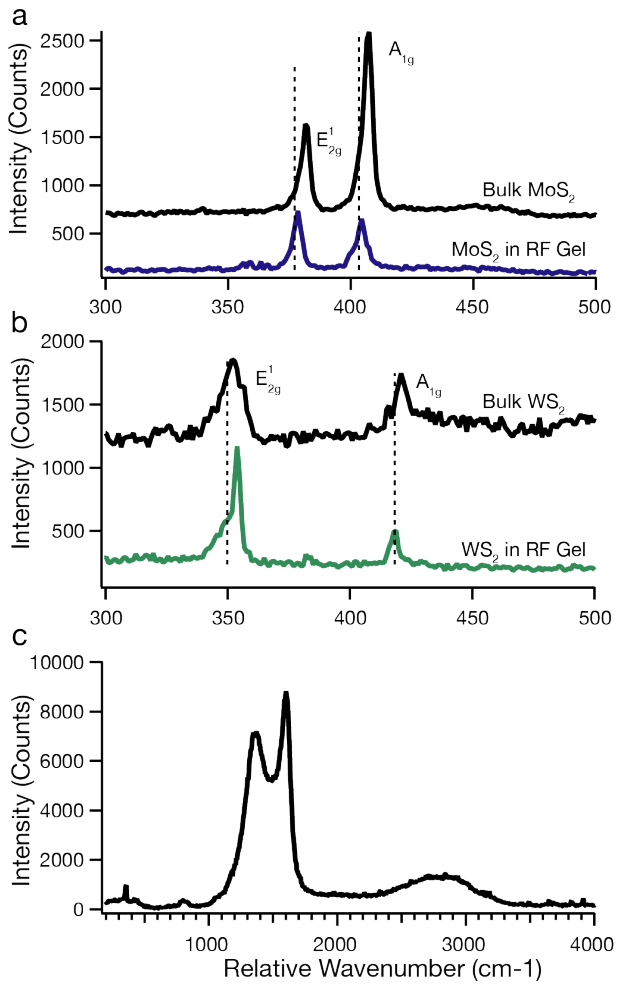

Figure 7.4: Raman characterization of MoS_2 (a) and WS_2 (b) dispersed within the RF matrix of the aerogel (c) for samples synthesized from 17 mg mL^{-1} TMD dispersions. The Raman scattering of the aerogel (c) was collected from the WS_2 composite. For each RF-supported TMD, the bulk Raman spectra is displayed offset for comparison. In addition, the supported TMD and bulk Raman spectra were collected without adjusting the spectrometer grating to prevent alignment-induced shifts in wavenumber. All wavenumbers were further calibrated with a silicon wafer. Vertical dotted lines represent peak centers of the in plane (E^1_{2g}) and out of plane (A_{1g}) modes of the exfoliated TMD's to emphasize the shift from their bulk counterparts due to exfoliation in the case of MoS_2 and WS_2.

in the (001) direction decreased during processing. For MoS_2, there is a less distinct shift, which suggests that the exfoliated material is only slightly shifted from its bulk counterpart (Figure 7.4a). The exfoliated, dispersed (bulk) E^1_{2g} peak sits at 378 cm^{-1} (381 cm^{-1}) and the A_{1g} sits at 404 cm^{-1} (407 cm^{-1}), leading to a difference of 26 cm^{-1} (26 cm^{-1}). A comparison to literature for the out-of-plane A_{1g} shows that each MoS_2 remained coupled to only one other layer. However, the E^1_{2g} and peak spacing suggest the material retained its bulk-like characteristics [235, 237].

The XRD and SAED of both MoS_2 and WS_2-loaded aerogels demonstrated that the TMD's remained crystalline throughout the rapid sol-gel processing and the subsequent high-temperature pyrolysis (Figures 7.2 and 7.5). For these sulfur-based TMD's, we identified the sharp peaks in XRD as highly crystalline 2H phases. The underlying broad peak centered at $2\theta\bar{1}7°$originates from amorphous carbon within the aerogel [203]. By examining the peak broadening, we further quantified the size of the TMD crystals loaded into the aerogels, using the Scherrer equation. This analysis suggested that on average, the thickness of the WS_2 crystallites in the (002) axis is about the same for all the WS_2-loaded aerogels, around 100 nm or 160 layers; whereas the thickness of the MoS_2 crystallites in the MoS_2-loaded aerogel is somewhat lower at 64 nm or 104 layers (Table 7.1). This agrees well with the cross-sectional TEM images of the pyrolyzed aerogels (Figure 7.2).

7.3.2 Electrochemical characterization of composites

From electrochemical tests of our pyrolyzed TMD aerogel supercapacitor electrodes, we evaluated specific volumetric capacitance based on galvanostatic discharge profiles at each applied current, using the full voltage window of 0.9–0.1 V (Figure 7.6d). As we vary the mass loading of TMD's into the aerogel, we observed significant differences in the densities of the aerogels: 0.33, 0.61, and 0.90 g cm^{-3} for RFA, MA-17, and WA-8.6, respectively. The wide range reflects the significant differences in the TMD densities—7.5 g cm^{-3} for WS_2 and 5.06 g cm^{-3} for MoS_2—as well as their molecular weights. For example, while the WS_2 comprises only 3.3 mol-% of WA-17, it represents 41.5 mass-%. Thus, the resulting capacitances repre-

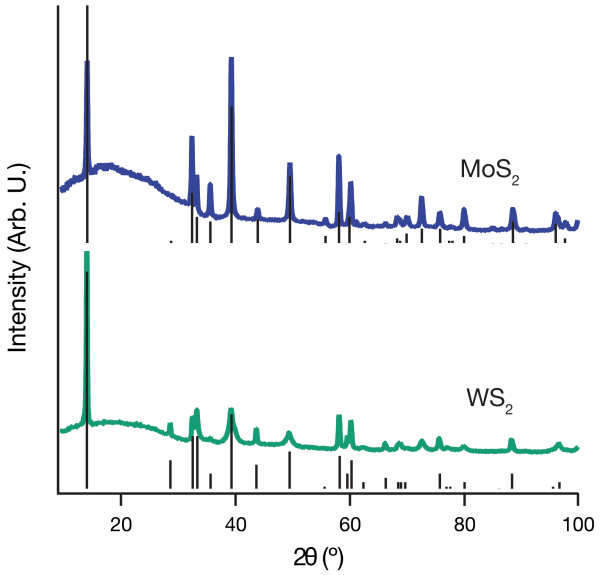

Figure 7.5: XRD patterns of MA-17 and WA-17. Vertical solid lines show the corresponding XRD peaks and relative intensities of 2H-MoS_2 and 2H-WS_2 from the International Centre for Diffraction Data cards.

sent the interplay between the molar percentage of the TMD and the density, capacitance, surface area, and conductivity of the added TMD, as discussed below. While undoped and doped aerogels exhibited similar gravimetric capacitances (87.5 and 84.5 F g^{-1} maxima, respectively), the volumetric capacitance increased significantly upon the addition of TMD's (Table 7.1). The WA-34 exhibited the greatest volumetric capacitance of the samples at 59.8 F cm^{-3} (64.7 F g^{-1}), 127% greater than RFA at 26.3 F cm^{-3} (87.5 F g^{-1}). Similarly, the MA-17 featured a large volumetric capacitance compared to the RFA, at 52.5 F cm^{-3} (84.5 F g^{-1}), as did the other WS_2-loaded aerogels. This marked improvement may be attributed to the reduction of inter-layer coupling in the TMD's accompanying sol-gel processing, as previously shown in Raman analysis. Additionally, the enhanced volumetric capacitance of the TMD-loaded aerogels suggests that they represent promising, scalable materials for high density supercapacitor applications, such as hybrid vehicles or portable electronics where space is constrained [197–199, 238]. It is worth noting that all of our 2H TMD-loaded aero-

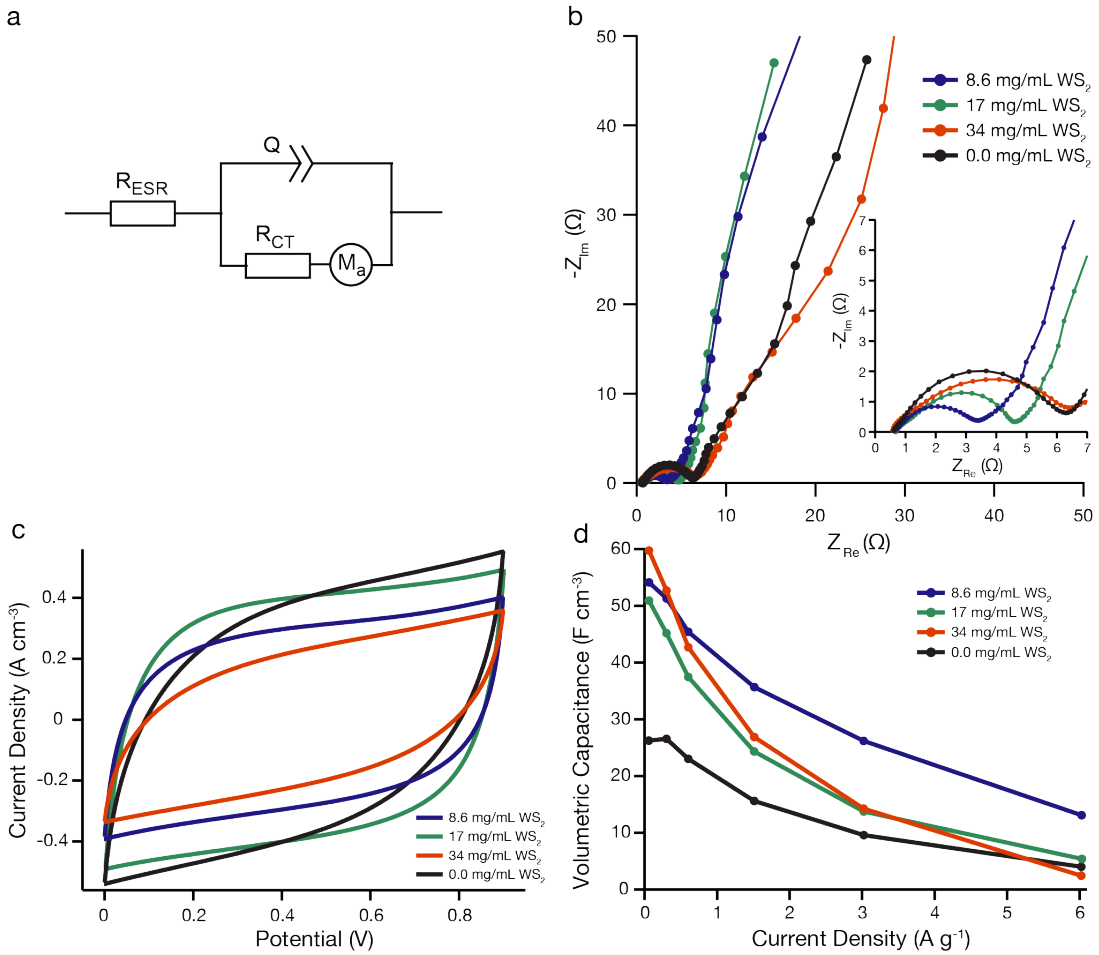

Figure 7.6: Electrochemical characterization of the pyrolyzed aerogels with different WS_2 mass loadings fabricated into coin cell supercapacitors, including equivalent circuit diagram (a), Nyquist plots from EIS (b, inset shows more detail of high–mid frequency range), cyclic voltammogram at sweep rate 20 mV s^{-1} (c), and specific volumetric capacitance (d) as a function of applied current density from galvanostatic tests.

gel devices perform markedly better than devices based on pure, bulk 2H TMD (2–3 F g^{-1} to 40 F g^{-1}) and similarly to devices based on the 1T metallic phase of MoS_2 (~80 F g^{-1}) without pyrophoric materials [212, 239].

The addition of TMD's also improved the rate performance of the aerogels. At the highest tested current, the specific capacitance of WA-8.6 was 24% of its maximum value, compared to 15% for RFA. However, WA-17, WA-34, and MA-17 exhibited more severe drop-offs than RFA. We hypothesize that the poorer capacitance retention of these samples, as well as RFA, is correlated with their higher charge transfer resistance, a value that is measured from impedance spectroscopy, as discussed below. In addition, WA-17 exhibited excellent cycling stability, and increased in performance during repeated charging and discharging. The WA-17 specific capacitance more than doubled between cycles 200 and 400, remaining 33% higher than its initial value at the final tested discharge. This enhanced capacitance during cycling may be due to additional exfoliation of the TMD or increased pseudocapacitance during charging and discharging, as observed by Bissett et al. for MoS_2–graphene composite electrodes [240]. We model the experimental EIS data, shown as Nyquist plots in Figure 7.6b and S4a-b, with the equivalent circuit in Figure 7.6a, which consists of an equivalent series resistance R_{ESR} followed by a constant phase element Q in parallel to a charge transfer resistance R_{CT} and a finite linear diffusion element M_a. R_{ESR} comprises the resistances associated with the bulk electrolyte, bulk electrode, and "external" parts of the system such as the current collector, terminals, and leads. It is represented in the Nyquist plot by the intercept of the curve with the real impedance axis. R_{CT} comprises the resistances due to electron transfer at interfaces in the device and specific adsorption of ions onto the active material, and is measured as the diameter of the best-fit semicircle at mid to high frequencies. Although R_{CT} is typically associated with the kinetics of Faradaic reactions at the electrode–electrolyte interface, the lack of peaks or troughs in the CV sweeps (Figure 7.6c), as well as the lack of voltage plateaus in the galvanostatic discharge profiles, suggest that no such reactions occur under our testing conditions. The constant phase element (CPE) accounts for frequency dispersion of capacitance that arises from the inhomogeneities of porous

and rough electrodes [241]. This causes a slight depression and angling of the semicircular arc that is characteristic of an RC component. Finally, M_a is a particular mass-transport impedance where the diffusion layer has a finite thickness and a reflecting (non-permeable) boundary condition. This accounts for the resistance of electrolyte in pores and interfacial double-layer capacitance along pore walls [242]. In the Nyquist plot, M_a manifests as the kinked line following the semicircle, which deviates from the vertical line of an ideal capacitor.

The Nyquist plots show that R_{CT} increases with WS_2 loading, and that R_{CT} is much greater for MA-17 than WA-17 (~21 Ω vs. 3.9 Ω), despite the former having larger pore sizes, which would reduce ion transport resistance. We hypothesize that these trends in R_{CT} are related to the formation of Schottky barriers between semiconducting TMD's and metals [243]. Zhang et al. have observed the analogous formation of a Schottky junction at the interface of MoS_2 with sp^2 hybridized carbon in graphite, which they attributed to the existence of metallic edge states in MoS_2 nanosheets [244]. Fermi level pinning may be exacerbated in these devices because the aerogels are not composed of pristine graphite, but carbonized RF polymer, whose highly defective structure hosts many charge trapping sites. Additionally, while WS_2 and MoS_2 have similar bulk contact resistances, the incorporation of WS_2 likely does not impact the overall charge transfer resistance of the aerogel as severely as MoS_2 due to differences in molar loading (Table 7.1). Alternatively, R_{CT} is associated with ion adsorption within the pores of the active material [245]. On this subject, an EIS study by Bissett et al. on supercapacitors with exfoliated TMD membrane electrodes in aqueous Na_2SO_4 electrolyte, showed that the ion adsorption in MoS_2 occurs on a much slower timescale compared to WS_2 [239]. It is worth noting that R_{CT} values comparable to ours have been reported previously for coin cells containing bulk (2H phase) MoS_2 as the active material [246].

Interestingly, R_{CT} of the RFA control is similar to WA-34 (5.7 Ω). This observation is consistent with previous studies of TMD-carbon composite supercapacitors where the addition of the TMD lowered R_{CT} from that of the plain carbon as well as the bulk TMD [247, 248]. Like WA-34 and MA-17, the RFA has larger pores which would lower ionic

resistance, but no TMD's to contribute to contact resistance within the electrode. In this case, we hypothesize that the larger RCT is related to the significantly higher specific surface area (776 m^2 g^{-1}) and lower bulk density (0.33 g cm^{-3}) of the RFA due to the absence of TMD's, resulting in a more sparse 3D network of active material with poorer electronic conductivity whose effect is great enough to counteract the easier ion movement. In support of this claim, Yang et al. recently conducted a comprehensive study of pyrolyzed RF aerogel supercapacitors where the pore size was tuned by catalyst concentration [249]. They found that charge transfer resistance tended to increase in tandem with pore size and confirmed the high electronic resistance of samples with large pores by four-point probe measurements.

In contrast to R_{CT}, R_{ESR} is similar for all tested aerogels, ranging from 0.56–0.76 Ω. This is not surprising given the identical composition of the pyrolyzed RF matrix and identical construction of the coin cell devices for all samples. The slight increase in R_{ESR} for MA-17 compared to WA-17 reflects the difference in the electrical conductivity of the constituent bulk TMD's—0.9 S cm^{-1} for WS_2 versus 0.2 S cm^{-1} for MoS_2 at 300 K [216, 250]. Mechanical integrity may also be responsible for the differences in series resistance, as the MA electrode amalgam had a stronger tendency to crack and flake apart during the flattening process, presumably due to the weak interlayer bonding of the TMD and its higher molar loading compared to WA-17.

Another performance metric is the knee frequency f_k, which is the frequency at which the semicircle transitions into the sloped linear region in the Nyquist plot, corresponding to a local minimum of the phase angle. Physically, the knee frequency signifies the point below which ions can penetrate more easily into pores of the active material, covering its entire surface to produce capacitive behavior. Within the WS_2 aerogels, f_k increases with decreasing TMD loading—20, 28, and 54 Hz for WA-34, WA-17, and WA-8.6 respectively—although it drops to 14 Hz for the unloaded RFA. The larger charge transfer resistance of WA-34 and RFA likely accounts for the lower f_k, even though they have larger pores on average compared to the other samples, which would suggest less hindrance to ion diffusion within the electrode [251]. In fact, the very short 45°-sloped Warburg region preceding the

steeper part of the line in these samples also suggests lower resistance to ion diffusion in the pores. The much lower f_k of MA-17 (4 Hz) compared to WA-17 is indicative of the former's much higher charge transfer resistance as well.

The wider pore size distribution of WA-34 and RFA also explains why these samples exhibit smaller slopes—corresponding to a lower phase angle—in the low-frequency region. With variation in pore sizes, the AC signal does not penetrate equally at a given frequency, since it is easier for ions to access larger pores than smaller pores, resulting in a shift from the theoretical vertical line of a capacitor. Song et al. developed a model to describe this particular frequency dispersion using a dimensionless frequency-dependent "penetrability" and a pore size distribution function, showing that the slope of the line in the Nyquist plot decreases for pore distributions with greater standard deviation [252, 253].

The current–voltage plots from the 20 mV s^{-1} CV sweeps are shown in Figure 7.6c. While an ideal capacitor exhibits a rectangular shape, the voltammograms of the aerogel samples exhibit rounded corners, indicating resistance to ion diffusion that slows the response of the current to changes in the direction of the voltage sweep. In agreement with EIS, the MA-17 shows the largest ion diffusion resistance, represented by a lens-shaped voltammogram. Similarly, WA-34 and RFA also have significantly distorted CV curves, while WA-8.6 and WA-17 have the most rectangular curves. The trend in CV shape reflects the superior volumetric capacitances of the WA-8.6 and WA-17 at most of the tested current densities, as well as their higher knee frequencies compared to the other two samples. The lack of peaks and troughs in the voltammograms of the three aerogels indicate that no redox reactions occur over the tested voltage range and that the mechanism of capacitance is purely double-layer. While Na^+ ions are known to intercalate between the layers of TMD particles, they are unlikely to do so except at extremely low scan rates [254, 255].

7.4 Conclusions

In conclusion, we have demonstrated a rapid, scalable nanomanufacturing process for the production of TMD-doped carbon aerogel composites via polycondensation of resorcinol and

Table 7.1: Summary of pyrolyzed TMD aerogel composite properties

	MoS_2 17 mg/mL	WS_2 8.6 mg/mL	WS_2 17 mg/mL	WS_2 34 mg/mL	No loading
TMD Mole %	6.70%	2.30%	4.40%	8.40%	0.00%
XRD Crystallite thickness (nm)	64	99	104	95	-
BET Surface Area (m^2g^{-1})	408	500	620	514	776
Gravimetric Capacitance (F g^{-1})	84.5	60.3	56.2	64.7	87.5
Volumetric Capacitance (F cm^{-3})	52.5	54.2	50.9	59.8	26.3
Molar Capacitance (F mol^{-1})	1650	970	1110	1760	1060
Equivalent Series Resistance $R_{ESR}(\Omega)$	0.76	0.60	0.68	0.56	0.60
Charge Transfer Resistance $R_{CT}(\Omega)$	21	2.6	3.9	5.7	5.7
Knee Frequency f_k(Hz)	4	54	28	20	14

formaldehyde catalyzed with hydrochloric acid in acetonitrile. Compared to typical aerogel processing (24 hours), the reaction presented here occurs in 2% of the time without sacrificing the narrow pore sizes or high surface areas of a standard RF aerogel. This synthesis outlines a general method to support TMD's with high electrical conductivity and porosity which is applicable to other stable TMD's. In addition, any novel advances in TMD synthesis or exfoliation can be directly incorporated via this process. Given the wide potential range of uses of TMD's, including electrochemical, photovoltaic, and catalytic applications, their efficient synthesis will enable rapid, combinatorial optimization of design parameters to engineer new devices. As a proof of concept, we explored the performance of MoS_2 and WS_2-doped carbon aerogels as electrodes for supercapacitors. An initial screening of device performances indicates that the addition of TMD's yields electrodes that are cyclically stable and offer volumetric capacitances up to 127% higher than pyrolyzed RF alone. Further, the

ability to rapidly process new materials into composites is magnified by the range of applications for high-surface-area, conductive supports, and we believe this scalable manufacturing methodology will find widespread use.

Appendix A

PRESSURE-DEPENDENT CARBON VACANCY DIFFUSION COEFFICIENT

A.1 Vacancy diffusion coefficient estimation

To determine vacancy diffusion coefficient in diamond at elevated temperature and pressure, we used a C$\beta\Omega$ model of the form [86, 87],

$$D = fa^2\nu exp\left(\frac{-c^{act}\beta\Omega}{k_BT}\right) \tag{A.1}$$

where D is the diffusion coefficient, a is the lattice parameter, ν is the attempt frequency, B estimated as the Debye frequency, B is the isothermal bulk modulus, Ω is the molar volume, k_B is the Boltzmann constant, T is the temperature. We calculate c^{act} from reported values and literature, using the equation

$$c^{act} = \frac{k_BT}{\beta\Omega}ln\left(\frac{fa\nu}{D}\right) \tag{A.2}$$

While the absolute value of the diffusion coefficient is strongly dependent on c^{act}, we are interested in the diffusion coefficient dependence on temperature and pressure via a, B, and Ω, which we calculate from the diamond equation of state. Notably, c^{act} has no dependence on temperature or pressure in this formalism and, thus, these results are independent of any debate over the value of vacancy diffusion activation, which range from 2.3 to 9.1 eV in literature, Supplementary Table 2.

We use a Mie-Grneisen-Debye model for the diamond equation of state with parameters

defined by Dewaele and coworkers,

$$P\left(V,T\right)=P_{V}\left(V,298K\right)+\left(P_{THDebye}\left(V,T\right)-P_{THDebye}\left(V,T\right)\right) \tag{A.3}$$

where

$$P_{V}=3K_{0}x^{-2}\left(1-x\right)exp\left(\left(1.5K_{0}^{\prime}-1.5\right)\left(1-x\right)\right) \tag{A.4}$$

In these equations, x, the dimensionless volume, is $\left(\frac{V}{V_0}\right)^{(1/3)}$, K_0 and $K_0^{\prime}$ are the bulk modulus and the pressure derivative of the bulk modulus in the reference state (ambient pressure and $T=0K$), and T, V, and P are the temperature, volume, and pressure. θ_{D} is the characteristic Debye temperature. As suggested by Dewaele, we assume the Debye temperature is only a function of volume,

$$\theta_{D}=\theta_{0}x^{-1.5}exp\left(\frac{\gamma_{1}\left(1-x^{3q}\right)}{q}\right) \tag{A.5}$$

Because γ_D is related to θ_D by $dln\theta_D/dlnV$, we define its volume dependence as

$$\gamma_{D}=\gamma_{1}x^{3q}+1/2 \tag{A.6}$$

To fit the values of Dewaele, we simplify this expression to

$$\gamma_{D}=\gamma_{1}x^{3q} \tag{A.7}$$

For the diamond EOS and vacancy diffusion calculations, we use the constants in Supplementary Table 3. The results of this analysis for $c^{act}=0.430$ are shown in Fig. S3.

To account for the time-dependence of vacancy-diffusion, we used a continuum probability distribution function for diffusion,

$$P\left(r,t,D\right)=\frac{4\pi r^{2}}{\left(4\pi Dt\right)^{3/2}}exp\left(\frac{-r^{2}}{4Dt}\right) \tag{A.8}$$

where D is the diffusion coefficient, t the time, and r is the radial distance from the starting

location. To solve for the diffusion coefficient at elevated temperatures and different time scales, we solved for a probability distribution function using experimental values from literature and $t = 3600$ s (Table 3). We then solved for the diffusion coefficient at elevated pressure, $D_{16.3GPa}$, with $t = 30$ s using,

$$P\left(r, 3600s, D_{atm}\right) = P\left(r, 30s, D_{16.3GPa}\right) \tag{A.9}$$

And used this value to calculate the necessary temperature at P=16.3 GPa.

Table A.1: Equivalent temperature diffusion coefficients at elevated pressure

Activation Energy (eV)	873.00 K	1073.00 K	1473.00 K
7.054	972.84	1198.15	1652.56
6.796	972.85	1198.17	1652.59
6.927	972.84	1198.159	1652.57
5.563	972.87	1198.203	1652.66
2.3	973.33	1198.89	1654.99
9.1	972.80	1198.07	1652.40

Here, $k_{solidAr}$ is calculated using the equation

$$log_{10}(k) = -1.5 \times log_{10}(T_{surface}) + 4.671 \tag{A.10}$$

and $k_{liquidAr}$ is calculated using

$$k = 6.38\times10^{-19}T^5 - 6.00\times10^{-15}T^4 + 2.26\times10^{-11}T^3 - 4.43\times10^{-8}T^2 + 7.06\times10^{-5}T - 5.55\times10^{-5} \tag{A.11}$$

The values in Table A.2 are representative of these calculations.

Table A.2: Constants and units used in vacancy diffusion coefficient calculations

Constant Name	Value	Units
V_0	5.6693	Å/ atom
K_0	444.5	GPa
K_0'	4.18	-
θ_0	1860	-
γ_1	0.85	-
q	3.6	-
ν	47.69	THz
f	0.7276	-
R	0.0138	GPaÅK^{-1}atom^{-1}
c^{act}	0.43	-
e	1	-
k	0.05	Wm^{-1}K^{-1}
$k_{solidAr}$	0.88	Wm^{-1}K^{-1}
$k_{liquidAr}$	0.066	Wm^{-1}K^{-1}
n_Carbon	1.5-1i	-
n_Ar	1.6	-

BIBLIOGRAPHY

1. Bell, A. T. The Impact of Nanoscience on Heterogeneous Catalysis. en. *Science* **299,** 1688–1691 (2003).
2. Murray, C. B., Norris, D. J. & Bawendi, M. G. Synthesis and Characterization of Nearly Monodisperse CdE (E = Sulfur, Selenium, Tellurium) Semiconductor Nanocrystallites. *Journal of the American Chemical Society* **115,** 8706–8715 (1993).
3. Michalet, X. *et al.* Quantum Dots for Live Cells, in Vivo Imaging, and Diagnostics. en. *Science* **307,** 538–544 (2005).
4. Weste, N. & Harris, D. *CMOS VLSI Design: A Circuits and Systems Perspective* 4 edition. English (Pearson, Boston, 2010).
5. Resch-Genger, U., Grabolle, M., Cavaliere-Jaricot, S., Nitschke, R. & Nann, T. Quantum Dots versus Organic Dyes as Fluorescent Labels. en. *Nature Methods* **5,** 763–775 (2008).
6. Roder, P. B., Smith, B. E., Zhou, X., Crane, M. J. & Pauzauskie, P. J. Laser Refrigeration of Hydrothermal Nanocrystals in Physiological Media. en. *Proceedings of the National Academy of Sciences* **112,** 15024–15029 (2015).
7. Wuttig, M. & Yamada, N. Phase-Change Materials for Rewriteable Data Storage. en. *Nature Materials* **6,** 824–832 (2007).
8. Pollack, G. L. Kapitza Resistance. *Reviews of Modern Physics* **41,** 48–81 (1969).
9. Voorhees, P. W. The Theory of Ostwald Ripening. en. *Journal of Statistical Physics* **38,** 231–252 (1985).
10. Rousseau, E., Siria, A., Jourdan, G., Volz, S., Comin, F., Chevrier, J. & Greffet, J.-J. Radiative Heat Transfer at the Nanoscale. en. *Nature Photonics* **3,** 514–517 (2009).
11. Carey, V. P., Chen, G., Grigoropoulos, C., Kaviany, M. & Majumdar, A. A Review of Heat Transfer Physics. *Nanoscale and Microscale Thermophysical Engineering* **12,** 1–60 (2008).
12. Voiry, D., Yang, J., Kupferberg, J., Fullon, R., Lee, C., Jeong, H. Y., Shin, H. S. & Chhowalla, M. High-Quality Graphene via Microwave Reduction of Solution-Exfoliated Graphene Oxide. en. *Science* **353,** 1413–1416 (2016).
13. González-Rubio, G. *et al.* Femtosecond Laser Reshaping Yields Gold Nanorods with Ultranarrow Surface Plasmon Resonances. en. *Science* **358,** 640–644 (2017).
14. Smith, B. E., Zhou, X., Roder, P. B., Abramson, E. H. & Pauzauskie, P. J. Recovery of Hexagonal Si-IV Nanowires from Extreme GPa Pressure. *Journal of Applied Physics* **119,** 185902 (2016).
15. Zhu, D., Zhang, L., Ruther, R. E. & Hamers, R. J. Photo-Illuminated Diamond as a Solid-State Source of Solvated Electrons in Water for Nitrogen Reduction. en. *Nature Materials* **12,** 836–841 (2013).

16. Zhou, Y. *et al.* Pressure-Induced Superconductivity in a Three-Dimensional Topological Material ZrTe5. en. *Proceedings of the National Academy of Sciences* **113,** 2904–2909 (2016).

17. Troyan, I., Gavriliuk, A., Rüffer, R., Chumakov, A., Mironovich, A., Lyubutin, I., Perekalin, D., Drozdov, A. P. & Eremets, M. I. Observation of Superconductivity in Hydrogen Sulfide from Nuclear Resonant Scattering. en. *Science* **351,** 1303–1306 (2016).

18. Wigner, E. & Huntington, H. B. On the Possibility of a Metallic Modification of Hydrogen. *The Journal of Chemical Physics* **3,** 764–770 (1935).

19. Weir, S. T., Mitchell, A. C. & Nellis, W. J. Metallization of Fluid Molecular Hydrogen at 140 GPa (1.4 Mbar). *Physical Review Letters* **76,** 1860–1863 (1996).

20. Knudson, M. D., Desjarlais, M. P., Becker, A., Lemke, R. W., Cochrane, K. R., Savage, M. E., Bliss, D. E., Mattsson, T. R. & Redmer, R. Direct Observation of an Abrupt Insulator-to-Metal Transition in Dense Liquid Deuterium. en. *Science* **348,** 1455–1460 (2015).

21. Eremets, M. I. & Troyan, I. A. Conductive Dense Hydrogen. en. *Nature Materials* **10,** 927–931 (2011).

22. May, P. W. Diamond Thin Films: A 21st-Century Material. en. *Philosophical Transactions of the Royal Society of London A: Mathematical, Physical and Engineering Sciences* **358,** 473–495 (2000).

23. Mochalin, V. N., Shenderova, O., Ho, D. & Gogotsi, Y. The Properties and Applications of Nanodiamonds. en. *Nature Nanotechnology* **7,** 11–23 (2012).

24. Weber, J. R., Koehl, W. F., Varley, J. B., Janotti, A., Buckley, B. B., de Walle, C. G. V. & Awschalom, D. D. Quantum Computing with Defects. en. *Proceedings of the National Academy of Sciences* **107,** 8513–8518 (2010).

25. Wort, C. J. H. & Balmer, R. S. Diamond as an Electronic Material. *Materials Today* **11,** 22–28 (2008).

26. Balasubramanian, G. *et al.* Nanoscale Imaging Magnetometry with Diamond Spins under Ambient Conditions. en. *Nature* **455,** 648–651 (2008).

27. Sque, S. J., Jones, R., Goss, J. P. & Briddon, P. R. Shallow Donors in Diamond: Chalcogens, Pnictogens, and Their Hydrogen Complexes. *Physical Review Letters* **92,** 017402 (2004).

28. Chrenko, R. M., Tuft, R. E. & Strong, H. M. Transformation of the State of Nitrogen in Diamond. *Nature* **270,** 141–144 (1977).

29. Moussa, J. E., Marom, N., Sai, N. & Chelikowsky, J. R. Theoretical Design of a Shallow Donor in Diamond by Lithium-Nitrogen Codoping. *Physical Review Letters* **108,** 226404 (2012).

30. Segev, D. & Wei, S.-H. Design of Shallow Donor Levels in Diamond by Isovalent-Donor Coupling. *Physical Review Letters* **91,** 126406 (2003).

31. Davies, G. & service), I. I. *Properties and Growth of Diamond* en. Google-Books-ID: RkFRAAAAMAAJ (INSPEC, the Institution of Electrical Engineers, 1994).

32. Dolde, F. *et al.* Nanoscale Detection of a Single Fundamental Charge in Ambient Conditions Using the $\mathrm{NV}{}{\ensuremath{-}}$ Center in Diamond. *Physical Review Letters* **112,** 097603 (2014).

33. Pezzagna, S., Rogalla, D., Wildanger, D., Meijer, J. & Zaitsev, A. Creation and Nature of Optical Centres in Diamond for Single-Photon Emission—overview and Critical Remarks. en. *New Journal of Physics* **13,** 035024 (2011).

34. Lewis, R. S., Ming, T., Wacker, J. F., Anders, E. & Steel, E. Interstellar Diamonds in Meteorites. *Nature* **326,** 160 (1987).

35. Stroud, R. M., Chisholm, M. F., Heck, P. R., Alexander, C. M. O. & Nittler, L. R. Supernova Shock-Wave-Induced CO-Formation of Glassy Carbon and Nanodiamond. en. *The Astrophysical Journal Letters* **738,** L27 (2011).

36. Verchovsky, A. B., Fisenko, A. V., Semjonova, L. F., Wright, I. P., Lee, M. R. & Pillinger, C. T. C, N, and Noble Gas Isotopes in Grain Size Separates of Presolar Diamonds from Efremovka. en. *Science* **281,** 1165–1168 (1998).

37. Thomson, A. R., Walter, M. J., Kohn, S. C. & Brooker, R. A. Slab Melting as a Barrier to Deep Carbon Subduction. en. *Nature* **529,** 76–79 (2016).

38. Boyd, F. R., Gurney, J. J. & Richardson, S. H. Evidence for a 150–200-Km Thick Archaean Lithosphere from Diamond Inclusion Thermobarometry. en. *Nature* **315,** 387–389 (1985).

39. Huss, G. R. & Lewis, R. S. Presolar Diamond, SiC, and Graphite in Primitive Chondrites: Abundances as a Function of Meteorite Class and Petrologic Type. *Geochimica et Cosmochimica Acta* **59,** 115–160 (1995).

40. Behler, K. D., Stravato, A., Mochalin, V., Korneva, G., Yushin, G. & Gogotsi, Y. Nanodiamond-Polymer Composite Fibers and Coatings. *ACS Nano* **3,** 363–369 (2009).

41. Li, X., Shao, J., Qin, Y., Shao, C., Zheng, T. & Ye, L. TAT-Conjugated Nanodiamond for the Enhanced Delivery of Doxorubicin. en. *Journal of Materials Chemistry* **21,** 7966–7973 (2011).

42. Zhang, Q., Mochalin, V. N., Neitzel, I., Knoke, I. Y., Han, J., Klug, C. A., Zhou, J. G., Lelkes, P. I. & Gogotsi, Y. Fluorescent PLLA-Nanodiamond Composites for Bone Tissue Engineering. *Biomaterials* **32,** 87–94 (2011).

43. Kotov, N. A. Inorganic Nanoparticles as Protein Mimics. en. *Science* **330,** 188–189 (2010).

44. Boudou, J.-P. *et al.* High Yield Fabrication of Fluorescent Nanodiamonds. en. *Nanotechnology* **20,** 235602 (2009).

45. Galimov, É. M. *et al.* Experimental Corroboration of the Synthesis of Diamond in the Cavitation Process. en. *Doklady Physics* **49,** 150–153 (2004).

46. Yang, G.-W., Wang, J.-B. & Liu, Q.-X. Preparation of Nano-Crystalline Diamonds Using Pulsed Laser Induced Reactive Quenching. en. *Journal of Physics: Condensed Matter* **10,** 7923 (1998).

47. Kirmani, A. R., Peng, W., Mahfouz, R., Amassian, A., Losovyj, Y., Idriss, H. & Katsiev, K. On the Relation between Chemical Composition and Optical Properties of Detonation Nanodiamonds. *Carbon* **94,** 79–84 (2015).

48. Pichot, V., Stephan, O., Comet, M., Fousson, E., Mory, J., March, K. & Spitzer, D. High Nitrogen Doping of Detonation Nanodiamonds. *The Journal of Physical Chemistry C* **114,** 10082–10087 (2010).

49. Volkov, D. S., Proskurnin, M. A. & Korobov, M. V. Elemental Analysis of Nanodiamonds by Inductively-Coupled Plasma Atomic Emission Spectroscopy. *Carbon* **74,** 1–13 (2014).

50. Toyli, D. M., Weis, C. D., Fuchs, G. D., Schenkel, T. & Awschalom, D. D. Chip-Scale Nanofabrication of Single Spins and Spin Arrays in Diamond. *Nano Letters* **10,** 3168–3172 (2010).

51. Jelezko, F. & Wrachtrup, J. Single Defect Centres in Diamond: A Review. en. *physica status solidi (a)* **203,** 3207–3225 (2006).

52. Chen, Y.-C. *et al.* Laser Writing of Coherent Colour Centres in Diamond. en. *Nature Photonics* **11,** 77–80 (2017).

53. Trusheim, M. E., Li, L., Laraoui, A., Chen, E. H., Bakhru, H., Schröder, T., Gaathon, O., Meriles, C. A. & Englund, D. Scalable Fabrication of High Purity Diamond Nanocrystals with Long-Spin-Coherence Nitrogen Vacancy Centers. *Nano Letters* **14,** 32–36 (2014).

54. Fitzgibbons, T. C., Guthrie, M., Xu, E.-s., Crespi, V. H., Davidowski, S. K., Cody, G. D., Alem, N. & Badding, J. V. Benzene-Derived Carbon Nanothreads. en. *Nature Materials* **14,** 43–47 (2015).

55. Mandal, M., Haso, F., Liu, T., Fei, Y. & Landskron, K. Size Tunable Synthesis of Solution Processable Diamond Nanocrystals. en. *Chemical Communications* **50,** 11307–11310 (2014).

56. Pauzauskie, P. J. *et al.* Synthesis and Characterization of a Nanocrystalline Diamond Aerogel. en. *Proceedings of the National Academy of Sciences* **108,** 8550–8553 (2011).

57. Wentorf, R. H. The Behavior of Some Carbonaceous Materials at Very High Pressures and High Temperatures. *The Journal of Physical Chemistry* **69,** 3063–3069 (1965).

58. Zhang, L., Mohanty, P., Coombs, N., Fei, Y., Mao, H.-K. & Landskron, K. Catalyst-Free Synthesis of Transparent, Mesoporous Diamond Monoliths from Periodic Mesoporous Carbon CMK-8. en. *Proceedings of the National Academy of Sciences* **107,** 13593–13596 (2010).

59. Guillou, C. L., Brunet, F., Irifune, T., Ohfuji, H. & Rouzaud, J.-N. Nanodiamond Nucleation below 2273 K at 15 GPa from Carbons with Different Structural Organizations. *Carbon* **45,** 636–648 (2007).

60. Liang, Z. Z., Kanda, H., Jia, X., Ma, H. A., Zhu, P. W., Guan, Q.-F. & Zang, C. Y. Synthesis of Diamond with High Nitrogen Concentration from Powder Catalyst-C-Additive NaN3 by HPHT. *Carbon* **44,** 913–917 (2006).

61. Tang, H., Wang, M., He, D., Zou, Q., Ke, Y. & Zhao, Y. Synthesis of Nano-Polycrystalline Diamond in Proximity to Industrial Conditions. *Carbon* **108,** 1–6 (2016).

62. Zapata, T. *et al.* Organic Nanodiamonds. *arXiv:1702.06854 [cond-mat, physics:physics].* arXiv: 1702.06854 [cond-mat, physics:physics] (2017).

63. Bray, K., Sandstrom, R., Elbadawi, C., Fischer, M., Schreck, M., Shimoni, O., Lobo, C., Toth, M. & Aharonovich, I. Localization of Narrowband Single Photon Emitters in Nanodiamonds. *ACS Applied Materials & Interfaces* **8,** 7590–7594 (2016).

64. Butler, J. E., Mankelevich, Y. A., Cheesman, A., Ma, J. & Ashfold, M. N. R. Understanding the Chemical Vapor Deposition of Diamond: Recent Progress. en. *Journal of Physics: Condensed Matter* **21,** 364201 (2009).

65. Tegetmeyer, B., Lewes-Malandrakis, G., Wernet, M., Schreyvogel, C., Lang, N., Yoshikawa, T. & Nebel, C. E. Incorporation of SiV-Centers in Diamond Nanoparticles Using Silicon Background Doping. *Diamond and Related Materials. 26th International Conference on Diamond and Carbon Materials* **65,** 87–90 (2016).

66. Vlasov, I. I., Shenderova, O., Turner, S., Lebedev, O. I., Basov, A. A., Sildos, I., Rähn, M., Shiryaev, A. A. & Van Tendeloo, G. Nitrogen and Luminescent Nitrogen-Vacancy Defects in Detonation Nanodiamond. en. *Small* **6,** 687–694 (2010).

67. Bundy, F. P., Bassett, W. A., Weathers, M. S., Hemley, R. J., Mao, H. U. & Goncharov, A. F. The Pressure-Temperature Phase and Transformation Diagram for Carbon; Updated through 1994. *Carbon* **34,** 141–153 (1996).

68. Bennett, P. C., Melcer, M. E., Siegel, D. I. & Hassett, J. P. The Dissolution of Quartz in Dilute Aqueous Solutions of Organic Acids at 25°C. *Geochimica et Cosmochimica Acta* **52,** 1521–1530 (1988).

69. Crane, M. J., Smith, B. E., Meisenheimer, P. B., Zhou, X., Davis, E. J., Pauzauskie, P. J. & Stroud, R. M. *Laser-Directed Spatial Control of High-Pressure, High-Temperature Nanocrystalline Diamond Formation* 2016.

70. Crane, M. J., Lim, M. B., Xuezhe, Z. & Pauzauskie, P. J. *Rapid Synthesis of Transition Metal Dichalcogenide Doped Carbon Aerogels for Supercapacitor Electrodes* 2017.

71. Dewaele, A., Loubeyre, P. & Mezouar, M. Equations of State of Six Metals above 94 GPa. *Physical Review B* **70,** 094112 (2004).

72. Carpenter, J. H., Root, S., Cochrane, K. R., Flicker, D. G. & Mattsson, T. R. *Equation of State of Argon: Experiments on Z, Density Functional Theory (DFT) Simulations, and Wide-Range Model* English. Unlimited Release SAND2012-7991 (Sandia National Laboratories, Sandia National Laboratories, 2012), 1–56.

73. Pekala, R. W. Organic Aerogels from the Polycondensation of Resorcinol with Formaldehyde. en. *Journal of Materials Science* **24,** 3221–3227 (1989).

74. Merzbacher, C. I., Meier, S. R., Pierce, J. R. & Korwin, M. L. Carbon Aerogels as Broadband Non-Reflective Materials. *Journal of Non-Crystalline Solids* **285,** 210–215 (2001).

75. Lu, X., Arduini-Schuster, M. C., Kuhn, J., Nilsson, O., Fricke, J. & Pekala, R. W. Thermal Conductivity of Monolithic Organic Aerogels. en. *Science* **255,** 971–972 (1992).

76. Klotz, S., Chervin, J.-C., Munsch, P. & Marchand, G. L. Hydrostatic Limits of 11 Pressure Transmitting Media. en. *Journal of Physics D: Applied Physics* **42,** 075413 (2009).

77. Ferrari, A. C. & Robertson, J. Raman Spectroscopy of Amorphous, Nanostructured, Diamond–like Carbon, and Nanodiamond. en. *Philosophical Transactions of the Royal Society of London A: Mathematical, Physical and Engineering Sciences* **362,** 2477–2512 (2004).

78. Korepanov, V. I. *et al.* Carbon Structure in Nanodiamonds Elucidated from Raman Spectroscopy. *Carbon* **121,** 322–329 (2017).

79. Onodera, A., Irie, Y., Higashi, K., Umemura, J. & Takenaka, T. Graphitization of Amorphous Carbon at High Pressures to 15 GPa. *Journal of Applied Physics* **69,** 2611–2617 (1991).

80. Khaliullin, R. Z., Eshet, H., Kühne, T. D., Behler, J. & Parrinello, M. Nucleation Mechanism for the Direct Graphite-to-Diamond Phase Transition. en. *Nature Materials* **10,** 693–697 (2011).

81. Wang, C., Chen, J., Yang, G. & Xu, N. Thermodynamic Stability and Ultrasmall-Size Effect of Nanodiamonds. en. *Angewandte Chemie International Edition* **44,** 7414–7418 (2005).

82. Nian, Q., Wang, Y., Yang, Y., Li, J., Zhang, M. Y., Shao, J., Tang, L. & Cheng, G. J. Direct Laser Writing of Nanodiamond Films from Graphite under Ambient Conditions. *Scientific reports* **4,** 6612 (2014).

83. Doherty, M. W. *et al.* Electronic Properties and Metrology Applications of the Diamond \${\mathrm{NV}}{\hat{-1}}\$ Center under Pressure. *Physical Review Letters* **112,** 047601 (2014).

84. Petrone, A., Goings, J. J. & Li, X. Quantum Confinement Effects on Optical Transitions in Nanodiamonds Containing Nitrogen Vacancies. *Physical Review B* **94,** 165402 (2016).

85. Havlik, J. *et al.* Boosting Nanodiamond Fluorescence: Towards Development of Brighter Probes. en. **5,** 3208–3211 (2013).

86. Dewaele, A., Datchi, F., Loubeyre, P. & Mezouar, M. High Pressure–high Temperature Equations of State of Neon and Diamond. *Physical Review B* **77,** 094106 (2008).

87. Zhang, Y., Zhang, L., Zhao, J., Wang, L., Zhao, G. & Zhang, Y. Doping of Vanadium to Nanocrystalline Diamond Films by Hot Filament Chemical Vapor Deposition. en. *Nanoscale Research Letters* **7,** 1–5 (2012).

88. Chang, S. L. Y., Barnard, A. S., Dwyer, C., Boothroyd, C. B., Hocking, R. K., Ōsawa, E. & Nicholls, R. J. Counting Vacancies and Nitrogen-Vacancy Centers in Detonation Nanodiamond. en. **8,** 10548–10552 (2016).

89. Schwartz, J., Aloni, S., Ogletree, D. F., Tomut, M., Bender, M., Severin, D., Trautmann, C., Rangelow, I. W. & Schenkel, T. Local Formation of Nitrogen-Vacancy Centers in Diamond by Swift Heavy Ions. *Journal of Applied Physics* **116,** 214107 (2014).

90. Karin, T., Dunham, S. & Fu, K.-M. Alignment of the Diamond Nitrogen Vacancy Center by Strain Engineering. *Applied Physics Letters* **105,** 053106 (2014).

91. Yin, C., Rancic, M., de Boo, G. G., Stavrias, N., McCallum, J. C., Sellars, M. J. & Rogge, S. Optical Addressing of an Individual Erbium Ion in Silicon. en. *Nature* **497,** 91–94 (2013).

92. Allen, T. M., Buehler, M. F. & Davis, E. J. Radiometric Effects on Absorbing Microspheres. *Journal of Colloid and Interface Science* **142,** 343–356 (1991).

93. Bastea, S. Transport Properties of Dense Fluid Argon. *Physical Review E* **68** (2003).

94. Simeoni, G. G., Bryk, T., Gorelli, F. A., Krisch, M., Ruocco, G., Santoro, M. & Scopigno, T. The Widom Line as the Crossover between Liquid-like and Gas-like Behaviour in Supercritical Fluids. en. *Nature Physics* **6,** 503–507 (2010).

95. Koscheev, A. P., Gromov, M. D., Mohapatra, R. K. & Ott, U. History of Trace Gases in Presolar Diamonds Inferred from Ion-Implantation Experiments. en. *Nature* **412,** 615–617 (2001).

96. Basu, S., Jones, A. P., Verchovsky, A. B., Kelley, S. P. & Stuart, F. M. An Overview of Noble Gas (He, Ne, Ar, Xe) Contents and Isotope Signals in Terrestrial Diamond. *Earth-Science Reviews* **126,** 235–249 (2013).

97. Ekimov, E. A., Kudryavtsev, O. S., Khomich, A. A., Lebedev, O. I., Dolenko, T. A. & Vlasov, I. I. High-Pressure Synthesis of Boron-Doped Ultrasmall Diamonds from an Organic Compound. en. *Advanced Materials* **27,** 5518–5522 (2015).

98. Frisch, M. J. *et al. Gaussian 16* Wallingford, CT, 2016.

99. Levinshtein, M. *Handbook Series on Semiconductor Parameters* en. Google-Books-ID: MSoNFpljBIEC (World Scientific, 1996).

100. Goss, J. P., Briddon, P. R. & Shaw, M. J. Density Functional Simulations of Silicon-Containing Point Defects in Diamond. *Physical Review B* **76,** 075204 (2007).

101. Moliver, S. S. Electronic Structure of Neutral Silicon-Vacancy Complex in Diamond. en. *Technical Physics* **48,** 1449–1453 (2003).

102. Goss, J. P., Jones, R., Breuer, S. J., Briddon, P. R. & Öberg, S. The Twelve-Line 1.682 eV Luminescence Center in Diamond and the Vacancy-Silicon Complex. *Physical Review Letters* **77,** 3041–3044 (1996).

103. Hepp, C. *et al.* Electronic Structure of the Silicon Vacancy Color Center in Diamond. *Physical Review Letters* **112,** 036405 (2014).

104. Thiering, G. & Gali, A. Complexes of Silicon, Vacancy, and Hydrogen in Diamond: A Density Functional Study. *Physical Review B* **92,** 165203 (2015).

105. Becke, A. D. Density-functional Thermochemistry. III. The Role of Exact Exchange. *The Journal of Chemical Physics* **98,** 5648–5652 (1993).

106. Lee, C., Yang, W. & Parr, R. G. Development of the Colle-Salvetti Correlation-Energy Formula into a Functional of the Electron Density. *Physical Review B* **37,** 785–789 (1988).

107. Miehlich, B., Savin, A., Stoll, H. & Preuss, H. Results Obtained with the Correlation Energy Density Functionals of Becke and Lee, Yang and Parr. *Chemical Physics Letters* **157,** 200–206 (1989).

108. Occelli, F., Loubeyre, P. & LeToullec, R. Properties of Diamond under Hydrostatic Pressures up to 140 GPa. en. *Nature Materials* **2,** 151–154 (2003).

109. Egerton, R. F. *Electron Energy-Loss Spectroscopy in the Electron Microscope* 2nd ed. (Plenum Press, New York, NY, 1996).

110. Shen, G., Mei, Q., Prakapenka, V. B., Lazor, P., Sinogeikin, S., Meng, Y. & Park, C. Effect of Helium on Structure and Compression Behavior of SiO2 Glass. en. *Proceedings of the National Academy of Sciences* **108,** 6004–6007 (2011).

111. Fukunaga, K., Matsuda, J.-i., Nagao, K., Miyamoto, M. & Ito, K. Noble-Gas Enrichment in Vapour-Growth Diamonds and the Origin of Diamonds in Ureilites. en. *Nature* **328,** 141–143 (1987).

112. Martinovich, V. A., Turukhin, A. V., Zaitsev, A. M. & Gorokhovsky, A. A. Photoluminescence Spectra of Xenon Implanted Natural Diamonds. *Journal of Luminescence. Proceedings of the 2002 International Conference on Luminescence and Optical Spectroscopy of Condensed Matter* **102-103,** 785–790 (2003).

113. Caldwell, W. A., Nguyen, J. H., Pfrommer, B. G., Mauri, F., Louie, S. G. & Jeanloz, R. Structure, Bonding, and Geochemistry of Xenon at High Pressures. en. *Science* **277,** 930–933 (1997).

114. Boehler, R., von Bargen, N. & Chopelas, A. Melting, Thermal Expansion, and Phase Transitions of Iron at High Pressures. en. *Journal of Geophysical Research: Solid Earth* **95,** 21731–21736 (1990).

115. Zaitsev, D. S. A. M. en. *Optical Properties of Diamond* 125–376 (Springer Berlin Heidelberg, 2001).

116. Feng, T. & Schwartz, B. D. Characteristics and Origin of the 1.681 eV Luminescence Center in Chemical-vapor-deposited Diamond Films. *Journal of Applied Physics* **73,** 1415–1425 (1993).

117. Lenef, A. & Rand, S. C. Electronic Structure of the N-V Center in Diamond: Theory. *Physical Review B* **53,** 13441–13455 (1996).

118. Mao, H. K., Xu, J. & Bell, P. M. Calibration of the Ruby Pressure Gauge to 800 Kbar under Quasi-Hydrostatic Conditions. en. *Journal of Geophysical Research: Solid Earth* **91,** 4673–4676 (1986).

119. Lin, J.-F., Degtyareva, O., Prewitt, C. T., Dera, P., Sata, N., Gregoryanz, E., Mao, H.-k. & Hemley, R. J. Crystal Structure of a High-Pressure/High-Temperature Phase of Alumina by in Situ X-Ray Diffraction. en. *Nature Materials* **3,** 389–393 (2004).

120. Dubrovinskaia, N. *et al.* Terapascal Static Pressure Generation with Ultrahigh Yield Strength Nanodiamond. en. *Science Advances* **2,** e1600341 (2016).

121. Amsler, M. *et al.* Crystal Structure of Cold Compressed Graphite. *Physical Review Letters* **108,** 065501 (2012).

122. Hu, M. *et al.* Compressed Glassy Carbon: An Ultrastrong and Elastic Interpenetrating Graphene Network. en. *Science Advances* **3,** e1603213 (2017).

123. Huang, Q. *et al.* Nanotwinned Diamond with Unprecedented Hardness and Stability. en. *Nature* **510,** 250–253 (2014).

124. Mao, W. L. *et al.* Bonding Changes in Compressed Superhard Graphite. en. *Science* **302,** 425–427 (2003).

125. Narayan, J. & Bhaumik, A. Novel Phase of Carbon, Ferromagnetism, and Conversion into Diamond. *Journal of Applied Physics* **118,** 215303 (2015).

126. Niu, H., Chen, X.-Q., Wang, S., Li, D., Mao, W. L. & Li, Y. Families of Superhard Crystalline Carbon Allotropes Constructed via Cold Compression of Graphite and Nanotubes. *Physical Review Letters* **108,** 135501 (2012).

127. Wang, Q. H., Kalantar-Zadeh, K., Kis, A., Coleman, J. N. & Strano, M. S. Electronics and Optoelectronics of Two-Dimensional Transition Metal Dichalcogenides. en. *Nature Nanotechnology* **7,** 699–712 (2012).

128. Yusa, H., Takemura, K., Matsui, Y., Morishima, H., Watanabe, K., Yamawaki, H. & Aoki, K. Direct Transformation of Graphite to Cubic Diamond Observed in a Laser-Heated Diamond Anvil Cell. *Applied Physics Letters* **72,** 1843–1845 (1998).

129. Iijima, S. Helical Microtubules of Graphitic Carbon. en. *Nature* **354,** 354056a0 (1991).

130. Kroto, H. W., Heath, J. R., O'Brien, S. C., Curl, R. F. & Smalley, R. E. C60: Buckminsterfullerene. en. *Nature* **318,** 318162a0 (1985).

131. Narayan, J. & Bhaumik, A. Research Update: Direct Conversion of Amorphous Carbon into Diamond at Ambient Pressures and Temperatures in Air. *APL Materials* **3,** 100702 (2015).

132. Koizumi, S., Watanabe, K., Hasegawa, M. & Kanda, H. Ultraviolet Emission from a Diamond Pn Junction. en. *Science* **292,** 1899–1901 (2001).

133. Pinault-Thaury, M. A., Tillocher, T., Habka, N., Kobor, D., Jomard, F., Chevallier, J. & Barjon, J. N-Type CVD Diamond: Epitaxy and Doping. *Materials Science and Engineering: B. Advances in Semiconducting Materials* **176,** 1401–1408 (2011).

134. Teukam, Z. *et al.* Shallow Donors with High N-Type Electrical Conductivity in Homoepitaxial Deuterated Boron-Doped Diamond Layers. en. *Nature Materials* **2,** 482–486 (2003).

135. Lovchinsky, I. *et al.* Nuclear Magnetic Resonance Detection and Spectroscopy of Single Proteins Using Quantum Logic. en. *Science,* aad8022 (2016).

136. Brownlee, D. *et al.* Comet 81P/Wild 2 Under a Microscope. en. *Science* **314,** 1711–1716 (2006).

137. Correa, A. A., Bonev, S. A. & Galli, G. Carbon under Extreme Conditions: Phase Boundaries and Electronic Properties from First-Principles Theory. en. *Proceedings of the National Academy of Sciences* **103,** 1204–1208 (2006).

138. Fayos, J. Possible 3D Carbon Structures as Progressive Intermediates in Graphite to Diamond Phase Transition. *Journal of Solid State Chemistry* **148,** 278–285 (1999).

139. Johnston, R. L. & Hoffmann, R. Superdense Carbon, C8: Supercubane or Analog of .Gamma.-Silicon? *Journal of the American Chemical Society* **111,** 810–819 (1989).

140. Liu, P., Cui, H. & Yang, G. W. Synthesis of Body-Centered Cubic Carbon Nanocrystals. *Crystal Growth & Design* **8,** 581–586 (2008).

141. Liu, P., Cao, Y. L., Wang, C. X., Chen, X. Y. & Yang, G. W. Micro- and Nanocubes of Carbon with C8-like and Blue Luminescence. *Nano Letters* **8,** 2570–2575 (2008).

142. Pokropivny, A. & Volz, S. 'C8 Phase': Supercubane, Tetrahedral, BC-8 or Carbon Sodalite? en. *physica status solidi (b)* **249,** 1704–1708 (2012).

143. Sheng, X.-L., Yan, Q.-B., Ye, F., Zheng, Q.-R. & Su, G. T-Carbon: A Novel Carbon Allotrope. *Physical Review Letters* **106,** 155703 (2011).

144. Takagi, M., Taketsugu, T., Kino, H., Tateyama, Y., Terakura, K. & Maeda, S. Global Search for Low-Lying Crystal Structures Using the Artificial Force Induced Reaction Method: A Case Study on Carbon. *Physical Review B* **95,** 184110 (2017).

145. Ferrari, A. C. & Robertson, J. Origin of the $1150-{\mathrm{cm}}{\hat{}-1}$ Raman Mode in Nanocrystalline Diamond. *Physical Review B* **63,** 121405 (2001).

146. Giannozzi, P. *et al.* QUANTUM ESPRESSO: A Modular and Open-Source Software Project for Quantum Simulations of Materials. en. *Journal of Physics: Condensed Matter* **21,** 395502 (2009).

147. Lewis, R. S., Anders, E. & Draine, B. T. Properties, Detectability and Origin of Interstellar Diamonds in Meteorites. en. *Nature* **339,** 117–121 (1989).

148. Bundy, F. P., Bovenkerk, H. P., Strong, H. M. & Wentorf, R. H. Diamond-Graphite Equilibrium Line from Growth and Graphitization of Diamond. *The Journal of Chemical Physics* **35,** 383–391 (1961).

149. Alivisatos, A. P. Perspectives on the Physical Chemistry of Semiconductor Nanocrystals. *The Journal of Physical Chemistry* **100,** 13226–13239 (1996).

150. Chen, C.-C., Herhold, A. B., Johnson, C. S. & Alivisatos, A. P. Size Dependence of Structural Metastability in Semiconductor Nanocrystals. en. *Science* **276,** 398–401 (1997).

151. Ashkin, A., Dziedzic, J. M., Bjorkholm, J. E. & Chu, S. Observation of a Single-Beam Gradient Force Optical Trap for Dielectric Particles. en. *Optics Letters* **11,** 288 (1986).

152. Ashkin, A., Dziedzic, J. M. & Yamane, T. Optical Trapping and Manipulation of Single Cells Using Infrared Laser Beams. en. *Nature* **330,** 769–771 (1987).

153. Bustamante, C., Bryant, Z. & Smith, S. B. Ten Years of Tension: Single-Molecule DNA Mechanics. en. *Nature* **421,** 423–427 (2003).

154. Gore, J., Bryant, Z., Nöllmann, M., Le, M. U., Cozzarelli, N. R. & Bustamante, C. DNA Overwinds When Stretched. en. *Nature* **442,** 836–839 (2006).

155. Neupane, K., Manuel, A. P. & Woodside, M. T. Protein Folding Trajectories Can Be Described Quantitatively by One-Dimensional Diffusion over Measured Energy Landscapes. en. *Nature Physics* **advance online publication** (2016).

156. Franosch, T., Grimm, M., Belushkin, M., Mor, F. M., Foffi, G., Forró, L. & Jeney, S. Resonances Arising from Hydrodynamic Memory in Brownian Motion. en. *Nature* **478,** 85–88 (2011).

157. Hertlein, C., Helden, L., Gambassi, A., Dietrich, S. & Bechinger, C. Direct Measurement of Critical Casimir Forces. *Nature* **451,** 172–175 (2008).

158. Mojarad, N. & Krishnan, M. Measuring the Size and Charge of Single Nanoscale Objects in Solution Using an Electrostatic Fluidic Trap. en. *Nature Nanotechnology* **7,** 448–452 (2012).

159. Peterman, E. J. G., Gittes, F. & Schmidt, C. F. Laser-Induced Heating in Optical Traps. *Biophysical Journal* **84,** 1308–1316 (2003).

160. Kyrsting, A., Bendix, P. M., Stamou, D. G. & Oddershede, L. B. Heat Profiling of Three-Dimensionally Optically Trapped Gold Nanoparticles Using Vesicle Cargo Release. *Nano Letters* **11,** 888–892 (2011).

161. Black, J. W., Kamenetska, M. & Ganim, Z. An Optical Tweezers Platform for Single Molecule Force Spectroscopy in Organic Solvents. *Nano Letters* **17,** 6598–6605 (2017).

162. Berg-Sørensen, K. & Flyvbjerg, H. Power Spectrum Analysis for Optical Tweezers. *Review of Scientific Instruments* **75,** 594–612 (2004).

163. Reece, P. J., Toe, W. J., Wang, F., Paiman, S., Gao, Q., Tan, H. H. & Jagadish, C. Characterization of Semiconductor Nanowires Using Optical Tweezers. *Nano Letters* **11,** 2375–2381 (2011).

164. Grollman, R. R., Busche, J. & Ostroverkhova, O. *Optical Tweezers-Based Probe of Charge Transfer in Organic Semiconductors at Microscopic Scales* **9360** (2015), 936016–936016–8.

165. Ye, F., Wu, C., Jin, Y., Chan, Y.-H., Zhang, X. & Chiu, D. T. Ratiometric Temperature Sensing with Semiconducting Polymer Dots. *Journal of the American Chemical Society* **133,** 8146–8149 (2011).

166. Hansen, P. M., Bhatia, V. K., Harrit, N. & Oddershede, L. Expanding the Optical Trapping Range of Gold Nanoparticles. *Nano Letters* **5,** 1937–1942 (2005).

167. Ashkin, A. Acceleration and Trapping of Particles by Radiation Pressure. *Physical Review Letters* **24,** 156–159 (1970).

168. Urban, A. S., Lutich, A. A., Stefani, F. D. & Feldmann, J. Laser Printing Single Gold Nanoparticles. *Nano Letters* **10,** 4794–4798 (2010).

169. Boikov, E. V., Vishnetskaya, M. V., Emel'yanov, A. N., Tomskii, I. S. & Shcherbakov, N. V. The Selective Catalytic Oxidation of Toluene. en. *Russian Journal of Physical Chemistry A, Focus on Chemistry* **82,** 2233–2237 (2008).

170. Li, A., Tang, S., Tan, P., Liu, C. & Liang, B. Measurement and Prediction of Oxygen Solubility in Toluene at Temperatures from 298.45 K to 393.15 K and Pressures up to 1.0 MPa. *Journal of Chemical & Engineering Data* **52,** 2339–2344 (2007).

171. Bradshaw, L. R., Hauser, A., McLaurin, E. J. & Gamelin, D. R. Luminescence Saturation via Mn2+–Exciton Cross Relaxation in Colloidal Doped Semiconductor Nanocrystals. *The Journal of Physical Chemistry C* **116,** 9300–9310 (2012).

172. McLaurin, E. J., Bradshaw, L. R. & Gamelin, D. R. Dual-Emitting Nanoscale Temperature Sensors. *Chemistry of Materials* **25,** 1283–1292 (2013).

173. Irvine, S., Staudt, T., Rittweger, E., Engelhardt, J. & Hell, S. Direct Light-Driven Modulation of Luminescence from Mn-Doped ZnSe Quantum Dots. en. *Angewandte Chemie* **120,** 2725–2728 (2008).

174. Roder, P. B., Pauzauskie, P. J. & Davis, E. J. Nanowire Heating by Optical Electromagnetic Irradiation. *Langmuir* **28,** 16177–16185 (2012).

175. Roder, P. B., Smith, B. E., Davis, E. J. & Pauzauskie, P. J. Photothermal Heating of Nanowires. *The Journal of Physical Chemistry C* **118,** 1407–1416 (2014).

176. Bird, R. B., Stewart, W. E., Lightfoot, E. N. & Klingenberg, D. J. *Introductory Transport Phenomena* 1 edition. English (Wiley, Hoboken, NJ, 2014).

177. Churchill, S. W. & Chu, H. H. S. Correlating Equations for Laminar and Turbulent Free Convection from a Vertical Plate. *International Journal of Heat and Mass Transfer* **18,** 1323–1329 (1975).

178. Šiler, M., Ježek, J., Jákl, P., Pilát, Z. & Zemánek, P. Direct Measurement of the Temperature Profile Close to an Optically Trapped Absorbing Particle. en. *Optics Letters* **41,** 870 (2016).

179. Fedoruk, M., Meixner, M., Carretero-Palacios, S., Lohmüller, T. & Feldmann, J. Nanolithography by Plasmonic Heating and Optical Manipulation of Gold Nanoparticles. *ACS Nano* **7,** 7648–7653 (2013).

180. Braun, M. & Cichos, F. Optically Controlled Thermophoretic Trapping of Single Nano-Objects. *ACS Nano* **7,** 11200–11208 (2013).

181. Ni, W., Ba, H., Lutich, A. A., Jäckel, F. & Feldmann, J. Enhancing Single-Nanoparticle Surface-Chemistry by Plasmonic Overheating in an Optical Trap. *Nano Letters* **12,** 4647–4650 (2012).

182. Chockla, A. M., Klavetter, K. C., Mullins, C. B. & Korgel, B. A. Solution-Grown Germanium Nanowire Anodes for Lithium-Ion Batteries. *ACS Applied Materials & Interfaces* **4,** 4658–4664 (2012).

183. Draine, B. T. & Flatau, P. J. Discrete-Dipole Approximation For Scattering Calculations. en. *Journal of the Optical Society of America A* **11,** 1491 (1994).

184. Chockla, A. M., Harris, J. T., Akhavan, V. A., Bogart, T. D., Holmberg, V. C., Steinhagen, C., Mullins, C. B., Stevenson, K. J. & Korgel, B. A. Silicon Nanowire Fabric as a Lithium Ion Battery Electrode Material. *Journal of the American Chemical Society* **133,** 20914–20921 (2011).

185. Comuñas, M. J. P. *et al.* Reference Correlation of the Viscosity of Squalane from 273 to 373 K at 0.1 MPa. *Journal of Physical and Chemical Reference Data* **42,** 033101 (2013).

186. Maragò, O. M., Jones, P. H., Gucciardi, P. G., Volpe, G. & Ferrari, A. C. Optical Trapping and Manipulation of Nanostructures. en. *Nature Nanotechnology* **8,** nnano.2013.208 (2013).

187. Aspnes, D. E. & Studna, A. A. Dielectric Functions and Optical Parameters of Si, Ge, GaP, GaAs, GaSb, InP, InAs, and InSb from 1.5 to 6.0 eV. *Physical Review B* **27,** 985–1009 (1983).

188. Hagemann, H.-J., Gudat, W. & Kunz, C. Optical Constants from the Far Infrared to the X-Ray Region: Mg, Al, Cu, Ag, Au, Bi, C, and Al_2O_3. EN. *JOSA* **65,** 742–744 (1975).

189. Crane, M. J. & Pauzauskie, P. J. Mass Transport in Nanowire Synthesis: An Overview of Scalable Nanomanufacturing. *Journal of Materials Science & Technology. A Special Issue on 1D NanomaterialsSynthesis, Properties, and Applications* **31,** 523–532 (2015).

190. Irrera, A. *et al.* Size-Scaling in Optical Trapping of Silicon Nanowires. *Nano Letters* **11,** 4879–4884 (2011).

191. Agarwal, R., Ladavac, K., Roichman, Y., Yu, G., Lieber, C. M. & Grier, D. G. Manipulation and Assembly of Nanowires with Holographic Optical Traps. EN. *Optics Express* **13,** 8906–8912 (2005).

192. Kudo, T., Wang, S.-F., Yuyama, K.-i. & Masuhara, H. Optical Trapping-Formed Colloidal Assembly with Horns Extended to the Outside of a Focus through Light Propagation. *Nano Letters* **16,** 3058–3062 (2016).

193. Lee, S.-W., Jo, G., Lee, T. & Lee, Y.-G. Controlled Assembly of In_2O_3 Nanowires on Electronic Circuits Using Scanning Optical Tweezers. EN. *Optics Express* **17,** 17491–17501 (2009).

194. Pauzauskie, P. J., Radenovic, A., Trepagnier, E., Shroff, H., Yang, P. & Liphardt, J. Optical Trapping and Integration of Semiconductor Nanowire Assemblies in Water. en. *Nature Materials* **5,** nmat1563 (2006).

195. Galajda, P. & Ormos, P. Rotors Produced and Driven in Laser Tweezers with Reversed Direction of Rotation. *Applied Physics Letters* **80,** 4653–4655 (2002).

196. Kedenburg, S., Vieweg, M., Gissibl, T. & Giessen, H. Linear Refractive Index and Absorption Measurements of Nonlinear Optical Liquids in the Visible and Near-Infrared Spectral Region. EN. *Optical Materials Express* **2,** 1588–1611 (2012).

197. Conway, B. E. *Electrochemical Supercapacitors* en (Springer US, Boston, MA, 1999).

198. Miller, J. R. & Simon, P. Electrochemical Capacitors for Energy Management. en. *Science* **321,** 651–652 (2008).

199. Conway, B. E., Birss, V. & Wojtowicz, J. The Role and Utilization of Pseudocapacitance for Energy Storage by Supercapacitors. *Journal of Power Sources* **66,** 1–14 (1997).

200. Simon, P. & Gogotsi, Y. Materials for Electrochemical Capacitors. en. *Nature Materials* **7,** nmat2297 (2008).

201. Li, J., Wang, X., Huang, Q., Gamboa, S. & Sebastian, P. J. Studies on Preparation and Performances of Carbon Aerogel Electrodes for the Application of Supercapacitor. *Journal of Power Sources* **158,** 784–788 (2006).

202. Li, X. & Wei, B. Supercapacitors Based on Nanostructured Carbon. *Nano Energy* **2,** 159–173 (2013).

203. Lim, M. B., Hu, M., Manandhar, S., Sakshaug, A., Strong, A., Riley, L. & Pauzauskie, P. J. Ultrafast Sol–gel Synthesis of Graphene Aerogel Materials. *Carbon* **95,** 616–624 (2015).

204. Pröbstle, H., Schmitt, C. & Fricke, J. Button Cell Supercapacitors with Monolithic Carbon Aerogels. *Journal of Power Sources. 7th Ulmer Elektrochemische Tage* **105,** 189–194 (2002).

205. Zhu, Y. *et al.* Carbon-Based Supercapacitors Produced by Activation of Graphene. en. *Science* **332,** 1537–1541 (2011).

206. Fricke, J., Pekala, R. W., Alviso, C. T., Kong, F. M. & Hulsey, S. S. Aerogels Derived from Multifunctional Organic Monomers. *Journal of Non-Crystalline Solids* **145,** 90–98 (1992).

207. Kim, S. J., Hwang, S. W. & Hyun, S. H. Preparation of Carbon Aerogel Electrodes for Supercapacitor and Their Electrochemical Characteristics. en. *Journal of Materials Science* **40,** 725–731 (2005).

208. Mulik, S., Sotiriou-Leventis, C. & Leventis, N. Time-Efficient Acid-Catalyzed Synthesis of Resorcinol-Formaldehyde Aerogels. *Chemistry of Materials* **19,** 6138–6144 (2007).

209. Wiener, M., Reichenauer, G., Hemberger, F. & Ebert, H.-P. Thermal Conductivity of Carbon Aerogels as a Function of Pyrolysis Temperature. en. *International Journal of Thermophysics* **27,** 1826–1843 (2006).

210. Lin, Y.-H., Wei, T.-Y., Chien, H.-C. & Lu, S.-Y. Manganese Oxide/Carbon Aerogel Composite: An Outstanding Supercapacitor Electrode Material. en. *Advanced Energy Materials* **1,** 901–907 (2011).

211. Worsley, M. A., Pauzauskie, P. J., Olson, T. Y., Biener, J., Satcher, J. H. & Baumann, T. F. Synthesis of Graphene Aerogel with High Electrical Conductivity. *Journal of the American Chemical Society* **132,** 14067–14069 (2010).

212. Acerce, M., Voiry, D. & Chhowalla, M. Metallic 1T Phase MoS2 Nanosheets as Supercapacitor Electrode Materials. en. *Nature Nanotechnology* **10,** 313–318 (2015).

213. Cao, L. *et al.* Direct Laser-Patterned Micro-Supercapacitors from Paintable MoS2 Films. en. *Small* **9,** 2905–2910 (2013).

214. Ratha, S. & Rout, C. S. Supercapacitor Electrodes Based on Layered Tungsten Disulfide-Reduced Graphene Oxide Hybrids Synthesized by a Facile Hydrothermal Method. *ACS Applied Materials & Interfaces* **5,** 11427–11433 (2013).

215. Ghatak, S., Pal, A. N. & Ghosh, A. Nature of Electronic States in Atomically Thin MoS2 Field-Effect Transistors. *ACS Nano* **5,** 7707–7712 (2011).

216. Kuck, S & Werheit, H. *Non-Tetrahedrally Bonded Binary Compounds II* (2000).

217. Cook, J. B., Kim, H.-S., Yan, Y., Ko, J. S., Robbennolt, S., Dunn, B. & Tolbert, S. H. Mesoporous MoS2 as a Transition Metal Dichalcogenide Exhibiting Pseudocapacitive Li and Na-Ion Charge Storage. en. *Advanced Energy Materials* **6,** n/a–n/a (2016).

218. Li, W., Irle, S. & Witek, H. A. Convergence in the Evolution of Nanodiamond Raman Spectra with Particle Size: A Theoretical Investigation. *ACS Nano* **4,** 4475–4486 (2010).

219. Worsley, M. A., Shin, S. J., Merrill, M. D., Lenhardt, J., Nelson, A. J., Woo, L. Y., Gash, A. E., Baumann, T. F. & Orme, C. A. Ultralow Density, Monolithic WS2, MoS2, and MoS2/Graphene Aerogels. *ACS Nano* **9,** 4698–4705 (2015).

220. Tang, Z., Wei, Q. & Guo, B. A Generic Solvent Exchange Method to Disperse MoS2 in Organic Solvents to Ease the Solution Process. en. *Chemical Communications* **50,** 3934–3937 (2014).

221. Coleman, J. N. *et al.* Two-Dimensional Nanosheets Produced by Liquid Exfoliation of Layered Materials. en. *Science* **331,** 568–571 (2011).

222. Jawaid, A., Nepal, D., Park, K., Jespersen, M., Qualley, A., Mirau, P., Drummy, L. F. & Vaia, R. A. Mechanism for Liquid Phase Exfoliation of MoS2. *Chemistry of Materials* **28,** 337–348 (2016).

223. Varrla, E., Backes, C., Paton, K. R., Harvey, A., Gholamvand, Z., McCauley, J. & Coleman, J. N. Large-Scale Production of Size-Controlled MoS2 Nanosheets by Shear Exfoliation. *Chemistry of Materials* **27,** 1129–1139 (2015).

224. Chhowalla, M., Shin, H. S., Eda, G., Li, L.-J., Loh, K. P. & Zhang, H. The Chemistry of Two-Dimensional Layered Transition Metal Dichalcogenide Nanosheets. en. *Nature Chemistry* **5,** 263–275 (2013).

225. Jeong, S., Yoo, D., Ahn, M., Miró, P., Heine, T. & Cheon, J. Tandem Intercalation Strategy for Single-Layer Nanosheets as an Effective Alternative to Conventional Exfoliation Processes. en. *Nature Communications* **6,** 5763 (2015).

226. Zheng, J., Zhang, H., Dong, S., Liu, Y., Tai Nai, C., Suk Shin, H., Young Jeong, H., Liu, B. & Ping Loh, K. High Yield Exfoliation of Two-Dimensional Chalcogenides Using Sodium Naphthalenide. en. *Nature Communications* **5,** 2995 (2014).

227. Su, W., Zhou, L. & Zhou, Y. Preparation of Microporous Activated Carbon from Coconut Shells without Activating Agents. *Carbon* **41,** 861–863 (2003).

228. Dungey, K. E., Curtis, M. D. & Penner-Hahn, J. E. Structural Characterization and Thermal Stability of MoS2 Intercalation Compounds. *Chemistry of Materials* **10,** 2152–2161 (1998).

229. Pachauri, V., Kern, K. & Balasubramanian, K. Chemically Exfoliated Large-Area Two-Dimensional Flakes of Molybdenum Disulfide for Device Applications. *APL Materials* **1,** 032102 (2013).

230. Sing, K. S. W. Reporting Physisorption Data for Gas/Solid Systems with Special Reference to the Determination of Surface Area and Porosity (Provisional). *Pure and Applied Chemistry* **54,** 2201–2218 (1985).

231. Li, W.-C., Lu, A.-H. & Guo, S.-C. Characterization of the Microstructures of Organic and Carbon Aerogels Based upon Mixed Cresol–formaldehyde. *Carbon* **39,** 1989–1994 (2001).

232. Ganguly, A., Sharma, S., Papakonstantinou, P. & Hamilton, J. Probing the Thermal Deoxygenation of Graphene Oxide Using High-Resolution In Situ X-Ray-Based Spectroscopies. *The Journal of Physical Chemistry C* **115,** 17009–17019 (2011).

233. Ferrari, A. C. & Robertson, J. Interpretation of Raman Spectra of Disordered and Amorphous Carbon. *Physical Review B* **61,** 14095–14107 (2000).

234. Maldonado-Hódar, F. J., Moreno-Castilla, C., Rivera-Utrilla, J., Hanzawa, Y. & Yamada, Y. Catalytic Graphitization of Carbon Aerogels by Transition Metals. *Langmuir* **16,** 4367–4373 (2000).

235. Zhang, X., Tan, Q.-H., Wu, J.-B., Shi, W. & Tan, P.-H. Review on the Raman Spectroscopy of Different Types of Layered Materials. en. *Nanoscale* **8,** 6435–6450 (2016).

236. Zeng, H. *et al.* Optical Signature of Symmetry Variations and Spin-Valley Coupling in Atomically Thin Tungsten Dichalcogenides. *Scientific Reports* **3** (2013).

237. Lee, C., Yan, H., Brus, L. E., Heinz, T. F., Hone, J. & Ryu, S. Anomalous Lattice Vibrations of Single- and Few-Layer MoS2. *ACS Nano* **4,** 2695–2700 (2010).

238. Zhou, J. *et al.* Ultrahigh Volumetric Capacitance and Cyclic Stability of Fluorine and Nitrogen Co-Doped Carbon Microspheres. en. *Nature Communications* **6,** 8503 (2015).

239. Bissett, M. A., Worrall, S. D., Kinloch, I. A. & Dryfe, R. A. W. Comparison of Two-Dimensional Transition Metal Dichalcogenides for Electrochemical Supercapacitors. *Electrochimica Acta* **201,** 30–37 (2016).

240. Bissett, M. A., Kinloch, I. A. & Dryfe, R. A. W. Characterization of MoS2–Graphene Composites for High-Performance Coin Cell Supercapacitors. *ACS Applied Materials & Interfaces* **7,** 17388–17398 (2015).

241. Balakrishnan, A. & Subramanian, K. *Nanostructured Ceramic Oxides for Supercapacitor Applications* (CRC Press, 2014).

242. Bisquert, J. Influence of the Boundaries in the Impedance of Porous Film Electrodes. *Physical Chemistry Chemical Physics* **2,** 4185–4192 (2000).

243. Das, S., Chen, H.-Y., Penumatcha, A. V. & Appenzeller, J. High Performance Multilayer MoS2 Transistors with Scandium Contacts. *Nano Letters* **13,** 100–105 (2013).

244. Zhang, L., Zhu, D., Nathanson, G. M. & Hamers, R. J. Selective Photoelectrochemical Reduction of Aqueous CO2 to CO by Solvated Electrons. en. *Angewandte Chemie International Edition* **53,** 9746–9750 (2014).

245. Hung, K., Masarapu, C., Ko, T. & Wei, B. Wide-Temperature Range Operation Supercapacitors from Nanostructured Activated Carbon Fabric. *Journal of Power Sources* **193,** 944–949 (2009).

246. Jiang, L., Zhang, S., Kulinich, S. A., Song, X., Zhu, J., Wang, X. & Zeng, H. Optimizing Hybridization of 1T and 2H Phases in MoS2 Monolayers to Improve Capacitances of Supercapacitors. *Materials Research Letters* **3,** 177–183 (2015).

247. Huang, K.-J., Wang, L., Zhang, J.-Z. & Xing, K. Synthesis of Molybdenum Disulfide/Carbon Aerogel Composites for Supercapacitors Electrode Material Application. *Journal of Electroanalytical Chemistry* **752,** 33–40 (2015).

248. Liu, Y., Wang, W., Huang, H., Gu, L., Wang, Y. & Peng, X. The Highly Enhanced Performance of Lamellar WS2 Nanosheet Electrodes upon Intercalation of Single-Walled Carbon Nanotubes for Supercapacitors and Lithium Ions Batteries. *Chemical Communications* **50,** 4485–4488 (2014).

249. Yang, I., Kim, S.-G., Kwon, S. H., Kim, M.-S. & Jung, J. C. Relationships between Pore Size and Charge Transfer Resistance of Carbon Aerogels for Organic Electric Double-Layer Capacitor Electrodes. *Electrochimica Acta* **223,** 21–30 (2017).

250. Kam, K.-K. Electrical Properties of WSe2, WS2, MoSe2, MoS2, and Their Use as Photoanodes in a Semiconductor Liquid Junction Solar Cell. *Retrospective Theses and Dissertations* (1982).

251. Farma, R., Deraman, M., Awitdrus, Talib, I. A., Omar, R., Manjunatha, J. G., Ishak, M. M., Basri, N. H. & Dolah, B. N. M. Physical and Electrochemical Properties of Supercapacitor Electrodes Derived from Carbon Nanotube and Biomass Carbon. English. *International Journal of Electrochemical Science* **8,** 257–273 (2013).

252. Song, H.-K., Hwang, H.-Y., Lee, K.-H. & Dao, L. H. The Effect of Pore Size Distribution on the Frequency Dispersion of Porous Electrodes. *Electrochimica Acta* **45,** 2241–2257 (2000).

253. Song, H.-K., Jung, Y.-H., Lee, K.-H. & Dao, L. H. Electrochemical Impedance Spectroscopy of Porous Electrodes: The Effect of Pore Size Distribution. *Electrochimica Acta* **44,** 3513–3519 (1999).

254. Friend, R. & Yoffe, A. Electronic Properties of Intercalation Complexes of the Transition Metal Dichalcogenides. *Advances in Physics* **36,** 1–94 (1987).

255. Gholamvand, Z., McAteer, D., Harvey, A., Backes, C. & Coleman, J. N. Electrochemical Applications of Two-Dimensional Nanosheets: The Effect of Nanosheet Length and Thickness. *Chemistry of Materials* **28,** 2641–2651 (2016).